Title

The dynamics of upstream blocking and hydraulic control in continuously stratified flow past topography

Author

Jagannathan, Arjun

Publication Date

2018

UNIVERSITY OF CALIFORNIA SAN DIEGO

The dynamics of upstream blocking and hydraulic control in continuously stratified flow past topography

A dissertation submitted in partial satisfaction of the
requirements for the degree
Doctor of Philosophy

in

Oceanography

by

Arjun Jagannathan

Committee in charge:

Kraig B. Winters, Chair
Laurence Armi, Co-Chair
Myrl C. Hendershott
Eugene R. Pawlak
Antonio L. Sanchez

2018

The dissertation of Arjun Jagannathan is approved, and it is acceptable in quality and form for publication on microfilm and electronically:

Co-Chair

Chair

University of California San Diego

2018

EPIGRAPH

“How often have I said to you that when you have eliminated the impossible, whatever remains, however improbable, must be the truth”

—Sherlock Holmes, The sign of four

TABLE OF CONTENTS

Signature Page . . . iii

Epigraph . . . iv

Table of Contents . . . v

List of Figures . . . vii

List of Tables . . . xi

Acknowledgements . . . xii

Vita . . . xiv

Abstract of the Dissertation . . . xv

Chapter 1 Introduction . . . 1
- 1.1 Background . . . 1
- 1.2 Outline of the dissertation . . . 7

Chapter 2 Stratified flows over and around long dynamically tall mountain ridges . . . 9
- 2.1 Introduction and background . . . 9
- 2.2 Modelling approach . . . 16
  - 2.2.1 Experimental setup . . . 17
  - 2.2.2 Near-boundary forcing . . . 19
- 2.3 A brief overview of the Winters and Armi (2014) analysis . . . 21
- 2.4 Diagnostics of the overflow . . . 22
- 2.5 Results . . . 23
  - 2.5.1 Infinite ridge ($\beta = \infty$) . . . 24
  - 2.5.2 Finite ridge ($\beta = 30$) . . . 32
- 2.6 Discussion . . . 48
  - 2.6.1 Applicability of the stratified hydraulic framework . . . 48
  - 2.6.2 Downstream conditions and the cold pool . . . 51
  - 2.6.3 The effect of an abrupt change in ridge elevation . . . 52
- 2.7 Limitations and extensions . . . 58
  - 2.7.1 Coriolis effects . . . 58
  - 2.7.2 Simple turbulence model . . . 59
  - 2.7.3 The nature of the flow aloft . . . 59
  - 2.7.4 Extensions to other small Fr and large β flows . . . 60
- 2.8 Concluding remarks . . . 60

Chapter 3 Stability of stratified downslope flows with an overlying stagnant isolating layer . . . 62
3.1 Introduction and background . . . 62
3.2 Ambient profiles characteristic of controlled downslope flows . . . 65
3.3 Mathematical formulation of the streamwise-local stability problems 68
3.4 Numerical implementation . . . 71
3.5 Results for generalized ambient flow profiles characteristic of downslope flow . . . 72
3.6 Discussion . . . 76
3.6.1 Physical interpretation of instability . . . 81
3.6.2 Spatial instability and the Winters and Armi (2014) downslope flow . . . 84
3.6.3 Applicability to other flow regimes . . . 92
3.7 Conclusion . . . 92

Chapter 4 The dynamical link between hydraulic control and wave excitation aloft in blocked stratified flow over topography . . . 94
4.1 Introduction . . . 94
4.2 Theoretical framework for blocked controlled flows in the presence of a sharp density step . . . 97
4.3 Model description . . . 103
4.4 Numerical results . . . 104
4.4.1 Non-plunging interface: weak perturbations aloft . . . 108
4.4.2 Plunging interface: Large amplitude wave aloft . . . 110
4.5 Discussion and conclusions . . . 111

Appendix A Mapping the Winters and Armi (2014) solution to arbitrary terrain shapes 115

Appendix B Sensitivity of the flow structure aloft to domain height and sponge layer thickness . . . 117

Appendix C Description of the linear stability solver . . . 119

Bibliography . . . 121

LIST OF FIGURES

Figure 1.1: Regime diagram for three dimensional, stratified flow past a finite ridge of along-stream half-width σ_y and cross-stream half-length σ_x in the hydrostatic limit $h_m/\sigma_y \ll 1$ (adapted from Smith (1989)). 6

Figure 2.1: Schematic of low Fr controlled asymmetric overflow over an infinite ridge. . 11
Figure 2.2: Flow schematic for low Fr flow past a long but finite ridge of height h_m, along-stream half-width σ_y and cross-stream half-length σ_x with $\beta = \sigma_x/\sigma_y \gg 1$ that falls steeply to ground level at the lateral ends within a length scale $\sigma_x^* \ll \sigma_x$. 12
Figure 2.3: (a) Vertical profiles of the streamwise velocity at the blocking point $y \approx -y_b$ at $t'_\delta = 2.0, 11.7$ and 31.1 along with the analytical prediction of Winters and Armi (2014) for $Fr = 0.16$ flow over an infinite ridge. (b) Normalized upstream volume transport $Q'(t'_\delta)$ (black) in the controlled overflowing layer. 25
Figure 2.4: Time evolution of the flow field for $Fr = 0.16$ flow over an infinite ridge. (Top) Isopycnal lines and contours and (bottom) streamwise velocity contours. 27
Figure 2.4: Time evolution of the flow field for $Fr = 0.16$ flow over an infinite ridge (Continued). 28
Figure 2.4: Time evolution of the flow field for $Fr = 0.16$ flow over an infinite ridge (Continued). 29
Figure 2.5: Vertical profiles of streamwise velocity $v(y,z,t'_\delta)$ at various positions downstream of the upstream blocking location $-y_b$ for the infinite ridge overflow at $Fr = 0.16$. The positions of the downstream locations relative to the ridge center are indicated in the bottom panel of Fig. 2.4a. 31
Figure 2.6: Plunging depth, $p_d(t'_\delta)$ of the lowest streamline that crests the obstacle for $Fr = 0.16$ flow over an infinite ridge. 31
Figure 2.7: Vertical profiles of the streamwise velocity $v(z,t'_\delta)$ in the centerplane $x = 0$ at the blocking point $y = -y_b$ for $Fr = 0.16$ flow over a finite ridge with $\beta = 30$. 32
Figure 2.8: Time evolution of the flow field at the symmetric centerplane, $x = 0$ for $Fr = 0.16$ flow over a finite ridge with $\beta = 30$. (Top) Isopycnal lines and contours and (bottom) streamwise velocity contours. 34
Figure 2.8: Time evolution of the flow field at the symmetric centerplane, $x = 0$ for $Fr = 0.16$ flow over a finite ridge with $\beta = 30$.(Continued) 35
Figure 2.8: Time evolution of the flow field at the symmetric centerplane, $x = 0$ for $Fr = 0.16$ flow over a finite ridge with $\beta = 30$.(Continued) 36
Figure 2.9: Same as Fig. 2.8 but at the cross-stream location $x = 0.93\sigma_x$ at times (a) $t'_\delta = 2.0$; (b) $t'_\delta = 11.7$ and (c) $t'_\delta = 48.9$. 37
Figure 2.9: Same as Fig. 2.8 but at the cross-stream location $x = 0.93\sigma_x$ (Continued) . 38
Figure 2.9: Same as Fig. 2.8 but at the cross-stream location $x = 0.93\sigma_x$ (Continued) . 39

Figure 2.10: Time evolution of streamlines in the horizontal plane at $z = 0.1h_m$, i.e. just above the ground level, for the finite ridge with $\beta = 30$ at $Fr = 0.16$: (a) $t'_\beta = 0.05$; (b) $t'_\beta = 0.31$ and (c) $t'_\beta = 1.3$. Thick red lines indicate fast positive flow and dark blue lines indicate reversed flow. 41

Figure 2.11: Streamwise velocity $v(x)/V_\infty$ at $t'_\beta = 1.3$ at the vertical level $z = 0.1h_m$ and along $y = -1.5\sigma_y$, the half-width of the ridge at $z = 0.1h_m$ (indicated as a dashed line in Fig. 2.10c). Shown in grey is the fit $v/V_\infty = A + B\sigma_x^2/x^2$, with $A = 1.1$ and $B = 1$. 42

Figure 2.12: Upstream volume transport $Q'(x = 0, t'_\delta)$ (black) of the overflow in the centerplane of the finite ridge, normalized by the infinite ridge prediction, Q; and normalized maximum streamwise velocity $v_{max}(x = 0, y_b, z, t'_\delta)/V_\infty$ (red) at the downstream location y_b. 42

Figure 2.13: Vertical profile of the late-time streamwise velocity in the centerplane $x = 0$ of the finite ridge at the blocking point $y = -y_{b_f}$ along with the predicted profile based on H_f. 45

Figure 2.14: (Black) Upstream volume transport $Q'_{H_f}(t'_\delta)$ in a layer of thickness H_f above the blocking level at the centerplane of the finite ridge, normalized by the analytical prediction Q_{H_f} and (red)normalized maximum streamwise velocity, $v_{max}(y_b, z, t'_\delta)/V_\infty$ at the downstream location y_b. 45

Figure 2.15: Vertical profiles of $v(x, y, z, t'_\delta)$ at various positions downstream of the upstream blocking location $-y_b$ for the finite ridge at two different vertical planes: (a) Centerplane $x = 0$, (b) Away from the centerplane, $x = 0.93\sigma_x$. 47

Figure 2.16: Plunging depth, $p_d(x, t'_\delta)$ of the lowest streamline that crests the obstacle for the overflow across a finite ridge with $\beta = 30$ at $Fr = 0.16$. Also shown is $p_d(t'_\delta)$ for the corresponding infinite ridge case. 48

Figure 2.17: (a) Front view and (b) side view of an infinite two level ridge with half-width σ_y, a finite tall central section of height $h_1 + \Delta h$ and half-length σ_x with $\beta = \sigma_x/\sigma_y \gg 1$, straddled on either side by a shorter section of height h_1 and infinite length. 53

Figure 2.18: Computed and predicted vertical profiles of the streamwise velocity at the blocking location $y = -y_b$ of the two-level ridge at (a) the cross-stream location $x = 1.4\sigma_x$ (indicated in Fig. 2.17) and (b) the centerplane $x = 0$ of the taller section. 55

Figure 2.19: Same as Fig. 2.18 but at cross-stream locations$y_1 \leftrightarrow y_1^*$ nearer to the taller section: (a) $x = 1.1\sigma_x$ (indicated in Fig. 2.17a) and (b) $x = 1.03\sigma_x$. 56

Figure 2.20: Schematic depicting the essential features of low Froude number over and around a long mountain ridge of height h_m. 56

Figure 3.1: The downslope jet setting where flow configurations described above occur. The bottom panel displays the typical velocity and stratification profiles at the blocking point and an arbitrary point downstream of the crest, labelled 1 and 2 respectively. 66

Figure 3.2: The background velocity for the illustrative case of $\alpha = 0.5$. As β increases, the flow changes character from a pure parabolic jet towards a linearly sheared profile. 73
Figure 3.3: (a) Vorticity gradient and (b) corresponding inverse Richardon number (Ri^{-1}) profile for the case $\alpha = 0.5$. 74
Figure 3.4: Normalized eigenfunctions (a)$|\hat{u}(z)|$ and (b)$|\hat{w}(z)|$ for $\beta = 0$. This represents the case where the bottom streamline is stationary, ie downslope flow evolves as a pure parabolic jet. 78
Figure 3.5: Normalized eigenfunctions (a),(c) $|\hat{u}(z)|$ and (b),(d) $|\hat{w}(z)|$ for $\beta = 1,2$. When the bottom streamline is not stationary, as for example in the case of a free-slip boundary. 79
Figure 3.6: Normalized eigenfunctions (a),(c) $|\hat{u}(z)|$ and (b),(d) $|\hat{w}(z)|$ for $\beta = 4,6$. This represents the case where the linear component begins to dominate the profile. $\beta = 4$ is the critical value where the velocity maximum coincides with the bottom streamline. 80
Figure 3.7: The Winters and Armi (2014) background velocity profiles at different downstream locations for the optimally controlled stratified downslope flow. . . 85
Figure 3.8: Normalized eigenfunctions (a)$|\hat{u}(z)|$ and (b)$|\hat{w}(z)|$ for the profiles representative of the solutions of Winters and Armi (2014). 85
Figure 3.9: (Adapted from Winters (2016)) Isopycnals and vorticity from a statistically steady non-linear simulation of stratified flow over a smooth topography matching the optimal upstream solution of Winters and Armi (2014) 91

Figure 4.1: (a) Schematic of low Fr controlled asymmetric overflow over an infinite ridge for the case of uniform upstream stratification and flow speed. (b) As in Fig. 4.1a but for the case when a density step is present in an otherwise uniformly stratified fluid with $Fr = V_\infty/N_0 h_m \ll 1$. 98
Figure 4.2: Quasi-steady flow field for 2D $Fr = 0.16$ flow over an infinite ridge with a density step characterized by $N_{\delta_i}/N_0 = 8.6$ located at $z_0 = 2.23h_m$. (Top) Isopycnal lines and contours and (bottom) streamwise velocity contours. Flow is from left to right. 105
Figure 4.3: Vertical profile of the steady streamwise velocity at the blocking point $y = -y_b$ for $Fr = 0.16$ flow over an infinite ridge with a sharp density step located at $z_0 = 2.23h_m$. The Winters and Armi (2014) parabolic overflow prediction is shown in red. 106
Figure 4.4: Prediction of vertical profiles of the velocity and density within the overflowing layer for the case $z_0 = 1.35h_m$, with $N_{\delta_i}/N_0 = 8.6$. (a) Excluding the density interface, (b) Including the density interface. 107
Figure 4.5: Same as Fig. 4.2 but for $z_0 = 1.73h_m$ 109
Figure 4.6: Vertical profile of the steady streamwise velocity at the blocking point $y = -y_b$ for $Fr = 0.16$ flow over an infinite ridge with a sharp density step located at $z_0 = 1.73h_m$. The prediction in red is based on the analytical framework of section 4.2 110

Figure 4.7: Same as Fig. 4.5 but for $z_0 = 1.35h_m$ 112
Figure 4.8: Same as Fig. 4.6 but for $z_0 = 1.35h_m$. 113

Figure A.1: Schematic illustrating how blocked controlled flows over an arbitrary topography are mapped to the Winters and Armi (2014) solution. 116

Figure B.1: Vertical profiles of the streamwise velocity at the blocking point $y \approx -y_b$ along with the analytical prediction of Winters and Armi (2014) for $Fr = 0.16$ flow over an infinite ridge for different configurations of the domain height and sponge layer thickness. 118

LIST OF TABLES

Table 2.1: Summary of important dimensional inner and outer variables and dimensionless flow parameters. 14
Table 2.2: Numerical implementation details for each of the flow experiments. 19

Table 3.1: Characteristics of the unstable mode in the two-parameter space of β and α. The last two columns are the dimensional values of the period (T_p) and wavelength (λ) of the unstable mode for the case $H \approx 1865$ as in the numerical experiments of Smith (1991). 77
Table 3.2: Characteristics of the unstable mode for the flow profiles representative of the exact solutions of Winters and Armi (2014). Refer to table 3.1 for more details on notation. 84

Table 4.1: Speed of fastest upstream propagating internal wave mode within the waveguide formed by the semi-parabolic overflow for different locations of the density step at $Fr = 0.16$ 108

ACKNOWLEDGEMENTS

I would like to start by thanking my parents who always encouraged me to pursue my interests and passions from a young age. This dissertation would not have been possible without their constant support, especially during and after the birth of my daughter. They and my in-laws flew halfway across the globe several times during the past 3 years to babysit and spend time with Shrimayi, so I could focus on research.

Thanks to my wife, Madhumitha who gave up her job in India and joined me in San Diego even while I was still a 2nd year Ph.D. scholar. Madhumitha and Shrimayi have both made this journey so much more enjoyable and memorable.

On the academic side, Kraig has been the ideal mentor that one could ask for. Always available and ever-enthusiastic to talk about science, his approach to research problems, attention to detail and honest critical feedback have played a major role in moulding my scientific personality. From him I learned what I know about stratified flows, computational fluid dynamics and parallel computing, and most of all, how to stay focussed and effectively communicate scientific findings.

My co-advisor Larry taught me the value of obervationally and experimentally grounded intuition, the need for a careful study of the research literature and the importance of making clear, reader-friendly figures. To him, I also owe most of my knowledge of hydraulics and stratified turbulence.

Myrl's unabated enthusiasm for all things science is an inspiration. He served as a sounding board for many ideas and his constant enouragement has been a great source of motivation.

Thank you Antonio Sanchez and Eugene Pawlak for your generous time, comments and questions. The knowledge and insight I gained from Prof. Sanchez's course on hydrodynamic stability greatly enhanced the discussion in chapter 3 of this dissertation. Bill Young's class on asymptotics and perturbation methods was another formative course in SIO.

Thanks and appreciations for the 2013 PO cohort, in particular, Shantong, Cesar and Jannes. Cesar has always amazed me with his encyclopedic knowledge of research frontiers in various sub-fields of oceanography. Talking to Shantong never failed to give me a wider perspective on issues, academic and otherwise. Beach soccer and TG with Jannes and the other wonderful students and staff of SIO made the five years spent here all the more memorable.

I would like to thank NSF for funding my research at SIO and NCAR for providing computational resources through the Yellowstone and Cheynne clusters, which made the research of chapter 2 possible. Special thanks are also due to the graduate student funding coordinator Shelley Weisel for ensuring financial support for me during this last quarter, thereby facilitating the completion of chapter 4 of this dissertation.

Chapter 2 and appendices A and B are a reprint of the revised manuscript, Jagannathan, A., Winters, K.B., Armi, L., “Stratified flows over and around long dynamically tall mountain ridges”, 2018, submitted to the *Journal of the Atmospheric Sciences*. The dissertation author was the primary investigator and author of this paper.

Chapter 3 is a reprint, in full, of the material as it appears in Jagannathan, A., Winters, K.B., Armi, L., “Stability of stratified downslope flows with an overlying stagnant isolating layer”, *Journal of Fluid Mechanics*, 810, 392411, doi:10.1017/jfm.2016.683. The dissertation author was the primary investigator and author of this paper.

Chapter 4 is under preparation for submission to the *Journal of Fluid Mechanics* as Jagannathan, A., Winters, K.B., Armi, L., “The dynamical link between hydraulic control and wave excitation aloft in blocked stratified flow over topography”. The dissertation author was the primary investigator and author of this work.

VITA

2009	B. Tech. in Ocean Engineering , Indian Institute of Technology, Madras
2012	M.S. in Ocean Engineering, Florida Atlantic University
2018	Ph.D. in Oceanography, University of California San Diego

PUBLICATIONS

Jagannathan, A., Winters, K.B., Armi, L, 2018: "The dynamical connection between hydraulic control and wave excitation aloft in blocked stratified flow over topography", *Journal of Fluid Mechanics*, in preparation

Jagannathan, A., Winters, K.B., Armi, L., 2018: "Stratified flow over and around long dynamically tall mountain ridges", *Journal of the Atmospheric Sciences*, Accepted, pending revision.

Jagannathan, A., Winters, K.B., Armi, L, 2017: "Stability of stratified downslope flows with an overlying stagnant isolating layer", *Journal of Fluid Mechanics*, 810, 392-411.

Jagannathan, A., Mohan, R., Dhanak, M, 2014: "A spectral method for the triangular cavity flow", *Computers and Fluids*, 95, 40-48.

ABSTRACT OF THE DISSERTATION

The dynamics of upstream blocking and hydraulic control in continuously stratified flow past topography

by

Arjun Jagannathan

Doctor of Philosophy in Oceanography

University of California San Diego, 2018

Kraig B. Winters, Chair
Laurence Armi, Co-Chair

Upstream flow blocking is a distinguishing feature of stratified flows incident on dynamically tall mountain ridges. Blocking occurs as a consequence of the upstream propagation of long internal wave modes that are excited at the obstacle and which permanently modify the oncoming flow. When the ridge is infinite, the fluid upstream and below a ‘blocking level’ is brought to stagnation. The resulting across-crest asymmetry combined with volume transport constraints causes the overflowing layer to accelerate and develop into a hydraulically controlled flow. The processes leading to the establishment of upstream blocking and hydraulic control occur on a characteristic short time scale. In the interior of a long, but finite ridge, a hydraulically controlled overflow similarly develops on a short time scale, while over a longer time scale, low-level horizontal flow splitting leads to the establishment of an upstream layer-wise potential flow beneath the blocking level. We demonstrate through numerical experiments that for sufficiently long ridges, crest control and streamwise asymmetry are seen on both the short and long time scales. We then proceed to quantify the overflow using the framework of stratified hydraulics.

In a separate study, we investigate the dynamic stability of stratified flow configurations characteristic of blocked, topographically controlled downslope flows. The essential character of the base flow profiles considered is determined by the analytical solutions of Winters and Armi (2014). Their condition of optimal control necessitates a streamline bifurcation above the blocking location, which then naturally produces a stagnant isolating layer overlying an accelerating downslope flow. We show that the inclusion of the isolating layer is an essential component of the stability analysis. The spatial stability problem is also examined in order to estimate the downstream location where finite amplitude features might manifest in streamwise slowly-varying flows over topography.

Finally, to expose the dynamical connection between topographic control and wave excitation aloft, we consider flow over dynamically tall ridges under stratification conditions that feature a strong density jump above crest level. We show that the height of the bifurcating streamline depends sensitively on the location of the step. Further, the question of whether or not the density interface remains flat or plunges across the crest as part of the hydraulically controlled flow is found to be directly related to the requirement of maintaining a subcritical overflow upstream. We also demonstrate that the top of the density interface acts as a ‘virtual topography’ for the flow aloft and fundamentally controls the amplitude of the wave response there.

Chapter 1

Introduction

1.1 Background

Situations where the density of a fluid changes with height are ubiquitous in geophysical and engineering flows. Both the ocean and atmosphere are stably stratified media in which the density slowly increases (decreases) with depth (height). Industrial applications where stratification plays an important dynamical role include natural ventilation (Linden, 1999), atmospheric boundary layer flow through wind turbines (Chamorro and Porté-Agel, 2010; Porté-Agel et al., 2011) and pollutant dispersion in turbulent buoyant plumes (e.g. Kaye, 2008). Flows whose dynamical behavior is fundamentally driven by small density gradients are also known as buoyancy driven flows. In the absence of turbulent mixing and dissipation, the streamlines of buoyancy driven flows overlap with the lines of constant density, called as isopycnals.

As a density stratified flow encounters topographical features, a wide range of dynamical possibilities arises. Internal gravity waves are launched as the flow impinges on the barrier; for a sufficiently tall obstacle, the isopycnals may steepen and overturn leading to irreversible turbulent mixing; the fluid can flow both over the barrier and around it, with the characteristics of each of these flow components depending on the stratification strength, background flow speed and obstacle height. Under certain conditions, the flow of a stratified fluid over an obstacle can also develop into an asymmetric hydraulically controlled flow, analogous to the flow of homogeneous fluid over an obstacle such as water over a dam. The primary focus of this dissertation is on such topographically controlled stratified flows.

Understanding and quantifying the response of stratified flows to topography is an important problem in oceanography and atmospheric science. Some applications are, parametrizing turbulent downstream mixing and surface form drag for global circulation models (Epifanio and Durran, 2001), forecasting downslope windstorm events and orogaphic precipitation (Miglietta and Buzzi, 2001), predicting pollutant dispersal (Hughes et al., 2009), and aviation safety near mountainous terrain. Another issue that has received renewed attention is the role of gusts associated with downslope winds and mountain gap flows in spreading and exacerbating wildfires (e.g. Huang et al., 2009; Cao and Fovell, 2016).

2D Stratified flow over obstacles can be broadly divided into three regimes based on the topographic Froude number $Fr = V_\infty / N h_m$, where V_∞ is the uniform speed far upstream, h_m is the mountain height and N is the stratification, assumed constant and defined as $N = \sqrt{-\frac{g}{\rho_0}\frac{\mathrm{d}\bar{\rho}}{\mathrm{d}z}}$, where g is the acceleration due to gravity, ρ_0 is a constant reference density and $\bar{\rho}(z)$ is the vertical profile of density. When $Fr \ll 1$, the flow is sufficiently energetic for all of the upstream fluid to crest the obstacle. Paradoxically, the flow in this energetic regime is linear and thus amenable to theoretical treatment (e.g. Queney, 1948; Baines, 1998). Depending on the ratio of the obstacle half-width σ_y to the intrinsic length scale V_∞ / N, the response in this case ranges from a potential flow when $\sigma_y \ll V_\infty / N$ to a purely vertically propagating linear mountain wave for a wide obstacle, $\sigma_y \gg V_\infty / N$.

In the opposite limit of dynamically tall ridges, with $h_m \gg V_\infty / N$ or $Fr \ll 1$, the flow is fundamentally non-linear and upstream influence strongly influences its character. Standing long wave modes of vertical scale h_m and group velocity $O(N h_m / \pi)$ are now able to propagate upstream against the oncoming flow. These disturbances are also known as columnar modes and they permanently alter the flow configuration upstream of the ridge. The most important consequence of upstream influence is that the fluid below a height δ from the crest is brought to stagnation. This is known as flow blocking and can also be inferred from energetic considerations as follows. A fluid particle of density ρ_0 will not be able to surmount a barrier of height h_m if

$$\frac{1}{2}\rho V_\infty^2 < g\int_0^{h_m} (h_m - z)\frac{\mathrm{d}\overline{\rho}}{\mathrm{d}z}\mathrm{d}z. \tag{1.1}$$

This suggests that upstream blocking occurs whenever $V_\infty < Nh_m$ ($Fr < 1$), and that the blocking scale $\delta = V_\infty/N$, . However, because of the neglect of the pressure term, this is a heuristic criterion rather than a precise one. The actual blocking characteristics are sensitive to factors like ridge geometry (Baines, 1987) and the dynamics of the overflow (Jagannathan et al., 2018). Hunt et al. (1997) propose that, in general, the blocking scale is $O(V_\infty/N)$ rather than V_∞/N.

The across-crest asymmetry induced by upstream influence promotes the formation of a hydraulically controlled downslope flow above the low-level blocked fluid. Using the framework of stratified hydraulics, Winters and Armi (2014) have recently developed analytical solutions for these controlled downslope flows, which include the effects of upstream blocking. The key features of the solution are a parabolically sheared profile for the upstream overflow above the blocking level $z = h_m - \delta$, and a streamline bifurcation that produces an asymmetric hydraulically controlled downslope flow capped by a 'dead' region of well-mixed, nearly stagnant fluid known as the isolating layer. Crucially, by coupling a condition of optimal crest control with a kinematic constraint for volumetric layer transport, the theory predicts the blocking scale δ and the height of the bifurcating streamline and thus, in effect, completely determines the flow solution within the lowest overlflowing layer.

In the intermediate $Fr = O(1)$ regime, the flow is weakly non-linear and is characterized by progressive steepening of isopycnals above the crest, with decreasing Fr. Overturning eventually occurs at some critical Froude number $Fr_{critical}$ that depends on the obstacle shape;

for e.g., $Fr_{critical} \approx 1.17$ for a hydrostatic ‘Witch of Agnesi’ obstacle (Clark and Peltier, 1984) . The flow solution for these 2D $O(1)$ Fr flows up to the onset of isopycnal overturning can be analytically obtained by solving the linearized version of Long’s equation (Long, 1955). The loss of static stability that occurs as isopycnals overturn above the crest triggers transition to a controlled downslope flow state (Baines, 1998) for which Long’s solution is no longer applicable. Long’s (1955) solution assumes that the incident velocity has a uniform vertical profile which is unaffected by the presence of the ridge. Smith (1985) extended this approach to construct a theory for downslope windstorms by using Long’s equation in conjunction with a streamline bifurcation that is motivated by hydraulic theory. However, this solution also does not factor the upstream influence of the ridge. Upstream blocking effects start to become important at some value of $Fr_{blocking} < 1$, with the fraction of blocked fluid beneath the crest increasing as Fr drops. When $Fr < Fr_{blocking}$ but not asymptotically smaller than 1, the flow exhibits features of both the non-linear $Fr \ll 1$ regime described by Winters and Armi (2014) as well as the linear wave regime $Fr \gg 1$. No analytical solutions exist for this case.

Strongly stratified flow past finite ridges excites upstream propagating columnar modes perpendicular to the ridge as well as oblique modes radiated from the edges. The former are responsible for upstream flow blocking while the latter promote horizontal flow deflection. In the limit $Fr \to 0$, Drazin (1961) showed that, to leading order, the flow beneath the crest of a finite obstacle is a layer-wise horizontal potential flow. However, in the simulations of (Smolarkiewicz and Rotunno, 1989), this solution was realized for $Fr <= 0.055$, which led them to postulate that it is valid only for values of Fr much smaller than 0.1. Typical Fr values for geophysical situations where upstream influence is significant range between 0.1 and 0.5. In this parameter space, Smolarkiewicz and Rotunno (1989) found that the upstream flow remains potential-like, but a pair of low-level vertically oriented lee vortices forms on the downstream side. Two different mechanisms have been proposed to explain the formation of these lee-vortices. While Smolarkiewicz and Rotunno (1989) suggests inviscid baroclinic production as the source of vorticity, (Schar and Durran, 1997) ascribes it to potential vorticity generation at sites of isopycnal overturning and subsequent turbulent internal dissipation.

A longstanding problem in the study of stratified flow past mountains is the effect of low-level lateral flow splitting on the flow component that crests the obstacle. Smith (1989) identified four broad flow regimes based on the Froude number of the flow and ridge aspect-ratio σ_x/σ_y (Fig. 1.1), where σ_x and σ_y are respectively the cross-stream half-length and along-stream half-width of the ridge. In high Fr flows, regardless of the ridge aspect ratio, only linear mountain waves are excited. When Fr is around 1 and the aspect ratio large, splitting effects are negligible; most of the fluid overflows the crest and isopycnals overturn aloft. At moderate values of the aspect ratio and $Fr < 1$, low-level flow splitting occurs and lee vortices form. The parameter regime that is the dynamically richest one is when $0.1 \leq Fr \leq 0.5$ and $\sigma_x/\sigma_y \gg 1$. In this case, the flow exhibits all three classes of phenomena, namely wave overturning, flow splitting and lee vortices. However, the precise regime boundaries demarcating this case from the purely wave-breaking and flow splitting ones are unknown.

As in the 2D case, isopycnal overturning occurs over the crest whenever Fr drops below a critical value, leading to irreversible turbulent mixing and dissipation. In the literature (e.g. Smith, 1989; Epifanio and Durran, 2001; Bauer et al., 2000), this process is often described in terms of a breaking mountain wave. A drawback of this interpretation is that it does not allow for an analytical prediction of the height where overturning first occurs. From numerical simulations (e.g. Clark and Peltier, 1977) and laboratory experiments (e.g. Baines and Hoinka, 1985), it is known that isopycnal overturning signals transition to a non-linear hydraulically controlled state, characterized by a thinning, accelerating downslope flow beneath a wedge of stagnant fluid in the lee. Therefore another interpretation of isopycnal overturning is that it is the mechanism by which an imperfect streamline (isopycnal) bifurcation forms, thereby facilitating the development of an asymmetric controlled flow across the crest. This latter interpretation is the one that we adopt throughout the rest of the dissertation. The advantage of this hydraulic view is that non-linearity

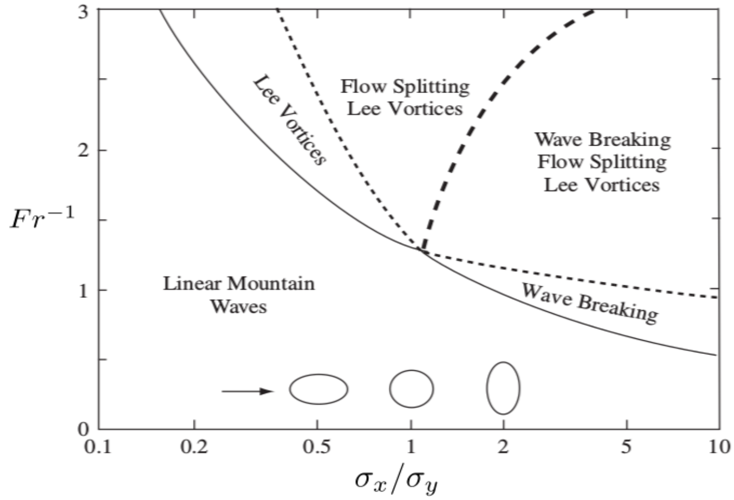

Figure 1.1: Regime diagram for three dimensional, stratified flow past a finite ridge of along-stream half-width σ_y and cross-stream half-length σ_x in the hydrostatic limit $h_m/\sigma_y \ll 1$ (adapted from Smith, 1989). The flow behavior is controlled by two independent dimensionless parameters: the aspect ratio σ_x/σ_y and the topographic Froude number Fr. Four distinct classes of phenomena are identifiable in these flows - a) Linear mountain waves, b) wave-breaking, c) flow-splitting and d) lee vortices.

is included at leading order, which is consistent with the observed highly non-linear character of these flows. Provided one can estimate the volume transport within the overflowing layer, the stratified hydraulic framework then allows for a prediction of the bifurcation height, the peak speed of the overflow, and thus in effect, a complete quantification of its characteristics.

Using numerical simulations, in this dissertation, we explore the applicability of hydraulic theory to the study of low Fr stratified flows over and around long mountain ridges in different idealized settings. The underlying philosophy behind our approach is as follows: The natural across-crest asymmetry in blocked low Fr flows is conducive to the formation of an asymmetric, crest controlled overflow. Consequently, the problem of predicting the overflow characteristics is essentially one of correctly estimating its volume transport. To estimate the transport correctly, upstream effects must be accurately quantified. Accordingly, a primary focus of this study is on understanding the dynamics and quantifying the spatial and temporal scales involved in the establishment of upstream flow blocking, lateral flow splitting and hydraulic control. An offshoot problem pertaining to the dynamic stability of blocked, hydraulically controlled downslope flows is then investigated numerically through a linear stability analysis. Finally, we consider the effect of a strong density jump above crest level on low Fr flow over an infinite ridge, focussing in particular on how this influences the height of the bifurcating streamline and the connection between the hydraulically controlled flow in the lowest overflowing layer and wave excitation further aloft.

1.2 Outline of the dissertation

This dissertation is composed of three research chapters. Chapter 2 investigates the nature of low Fr stratified flow over and around long ridges. The short and long time scales governing the development of the hydraulic overflow and horizontal flow splitting respectively are elucidated in terms of the propagation of upstream influence of the ridge through long columnar modes. We show that in flows where upstream influence is significant and the cross-stream to along-stream aspect ratio of the ridge is large, the blocking depth, overflow thickness and hence the height of the bifurcating streamline can be predicted by coupling a hydraulic control condition with a kinematic constraint for volume transport. Across-crest asymmetry and hydraulic control persist even after the establishment of the low-level splitting flow and the 2D stratified hydraulic framework of Winters and Armi (2014) provides a good quantification of the overflow characteristics. A synthesis of concepts from potential flow theory and stratified hydraulics is also shown to describe low Fr flow over non-uniform ridge shapes well.

Chapter 3 describes a study of the stability properties of blocked, topographically controlled downslope flows. These flows are known to be unstable and gusty in the lee (Lilly, 1978), but previous linear stability analyses (e.g. Smith, 1991) underpredict both the onset and strength of the instability. Taking the analytical flow solutions of Winters and Armi (2014) as the base flow profiles, a streamwise local linear stability analysis is carried out. The upstream flow profile is shown to be stable, having Richardson number $Ri > 1/4$ everywhere. Further downstream, the overflow becomes unstable owing to increasing shear at its upper flank where it meets the isolating layer. The time period and growth characteristics of the unstable mode agree well with the values reported by Lilly (1978) and Scinocca and Peltier (1989) while the spatial growth rates computed near the curve of marginal stability are consistent with the values inferred from the field observations of Farmer and Armi (1999) and numerical simulations of Winters (2016).

Chapter 4 deals with the effect of a strong density step located above crest level on blocked, topographically controlled flows. The height of the bifurcating streamline and the shape of the overflow are shown to depend sensitively on the location of the step relative to the bifurcation level in the uniformly stratified case. Further, the question of whether the density step does or does not plunge across the crest as part of the controlled overflow is fundamentally connected to the requirement of maintaining subcriticality upstream. The top of the density interface acts as as a virtual topography for the flow aloft and determines the amplitude of the vertically propagating wave excited above the overflow.

Chapter 2

Stratified flows over and around long dynamically tall mountain ridges

2.1 Introduction and background

The study of stratified flow past topography is of practical interest in atmospheric science and oceanography. Applications include parameterizing surface drag and turbulence in the lee of ridges, forecasting orographic precipitation and predicting the occurrence of downslope windstorm events. For a recent review of atmospheric applications, see Chow et al. (2012). While flow over dynamically short obstacles is fairly well described in terms of linear theory (e.g. Queney, 1948; Smith, 1980; Durran, 1990), flow over dynamically tall obstacles is fundamentally non-linear in character. Here dynamically tall implies a mountain height larger than the intrinsic height scale obtained from the upstream flow speed and stratification.

Further, when the cross-stream length of the ridge is large compared to its along-stream width, flows 'over' the crest and 'around' the sides develop over disparate time scales. Here, we consider long and dynamically tall mountain ridges and quantify the evolution of the overflow as the low level fluid upstream splits and flows laterally around the sides of the obstacle.

Energetics arguments (Sheppard, 1956) show that, for a sufficiently slow flow or strong stratification, much of the air upstream and below the ridge crest remains blocked. Upstream blocking has been observed both in 2D laboratory towing experiments (Baines, 1977; Baines and Hoinka, 1985) as well as in atmospheric flow over mountains, e.g. in flow over the Alps by Armi and Mayr (2007). The dynamical aspects of these flows are reviewed by Jackson et al. (2013).

When the flow is strictly two dimensional, blocking is accompanied by the formation of an overlying flowing layer that plunges down the obstacle as a non-linear, hydraulically controlled downslope flow. Continuity and mass conservation require that the flow within this layer makes up for the volume transport deficit caused by upstream flow stagnation. Winters and Armi (2014) show using non-linear stratified hydraulic theory that, for an infinite obstacle with upstream blocking, the steady state optimally controlled flow has an upstream velocity profile that is parabolic in shape and this flowing layer thins and accelerates as it plunges down the lee slope. A schematic of this flow is shown in Fig. 2.1.

One might ask whether hydraulic dynamics persist when the cross-stream ridge length is finite but large. In this case, the upstream fluid that is blocked when the ridge is infinite has energetically free horizontal pathways to pass around the obstacle. The validity of a two dimensional treatment of flow past finite obstacles was first raised by Brighton (1978) in the context of laboratory towing experiments. To illustrate the underlying dynamics, we perform numerical experiments in which a uniform upstream flow with speed V_∞ and stability N approaches a mountain ridge of height h_m. We focus on dynamically tall and long ridges, characterized by low topographic Froude number, $Fr = V_\infty/Nh_m \ll 1$ and large cross-stream to along-stream aspect- ratio, $\beta = \sigma_x/\sigma_y \gg 1$. β may also be regarded as a scaled ridge length. Fig. 2.2 shows a schematic of the flow configuration.

Fundamental inner flow scales emerge naturally from this configuration. Energetics considerations (e.g. Sheppard, 1956) suggest that the upstream flow remains blocked below a depth $\delta \approx V_\infty/N$ from the crest. We refer to δ as the blocking scale. When $Fr \ll 1$, $\delta \ll h_m$

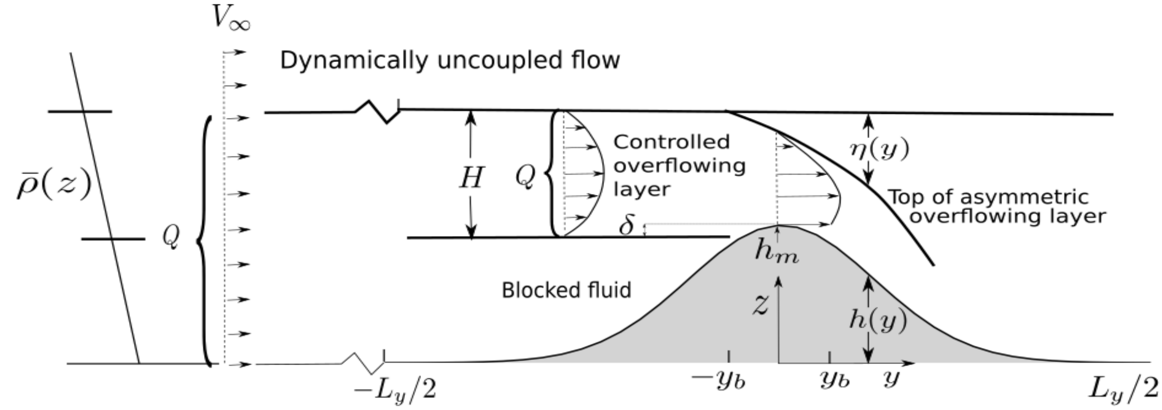

Figure 2.1: Schematic of low Fr controlled asymmetric overflow over an infinite ridge. The far upstream flow configuration is characterized by a linear density profile and uniform flow speed. The fluid upstream and below a depth δ from the crest is blocked. $y = -y_b$ is the streamwise coordinate of the blocking location and $y = y_b$ is the symmetric downstream location. Q denotes the volume transport within the parabolic overflow, which matches the far upstream transport as shown. The thickness H of the overflow is coupled to its transport Q as $Q = NH^2/\pi$ (Winters and Armi, 2014). Additionally, on either side of the crest, the vertical plunge $\eta(y)$ of the top of the overflow is uniquely mapped to $h(y) - h(-y_b)$, the height of the topography relative to the blocking point (see also section 2.3 and Appendix A). The streamwise computational boundaries are $y = -L_y/2$ and $y = L_y/2$. At the upstream boundary a radiation condition is prescribed (see section 2.2.2) which allows upstream propagating waves to escape the domain without reflection.

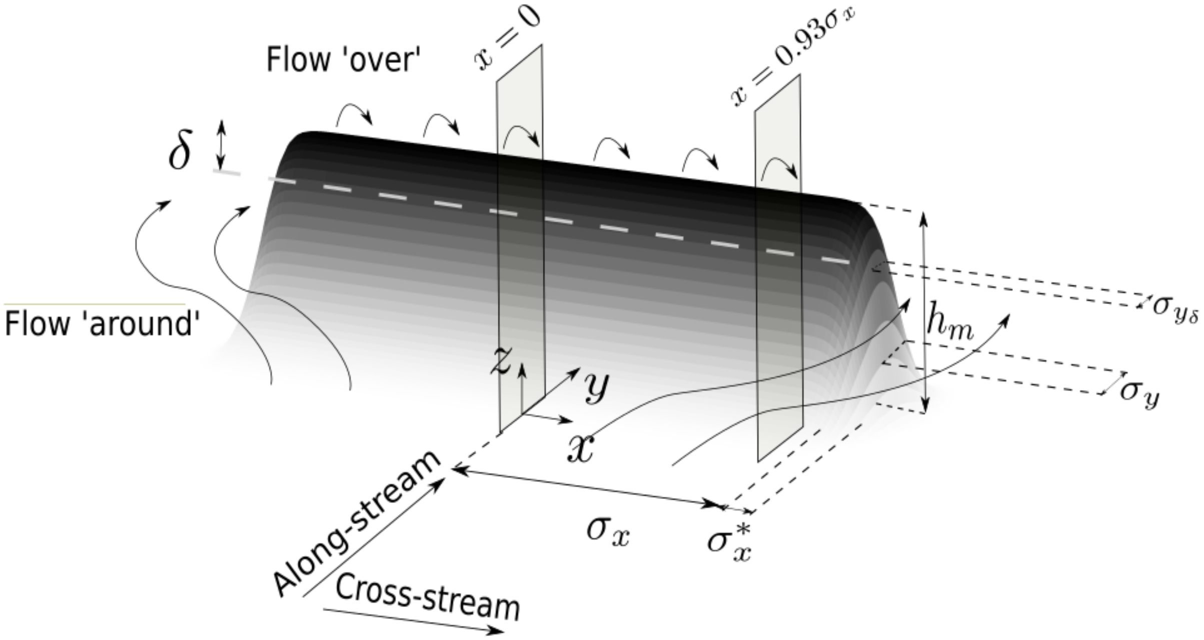

Figure 2.2: Flow schematic for low Fr flow past a long but finite ridge of height h_m, along-stream half-width σ_y and cross-stream half-length σ_x with $\beta = \sigma_x/\sigma_y \gg 1$ that falls steeply to ground level at the lateral ends within a length scale $\sigma_x^* \ll \sigma_x$. The far upstream flow speed and stratification are uniform and equal V_∞ and N respectively with $Fr = V_\infty/Nh_m \ll 1$. Figure not to scale.

constitutes an inner vertical length scale for the overflow. The flow below the blocking level $z = h_m - \delta$ is either blocked or splits around the obstacle laterally, suggesting a second inner length scale $\sigma_{y_\delta} = O(Fr\,\sigma_y)$, the half-width of the obstacle at the blocking level. The fluid above the blocking level has sufficient kinetic energy to flow 'over' the ridge. Thus $\beta_\delta = \sigma_x/\sigma_{y_\delta}$ is an effective scaled ridge length for the flow component that crests the obstacle. The excursion time,

$$t_\delta = \frac{\sigma_{y_\delta}}{V_\infty} \tag{2.1}$$

then follows as a natural inner time scale. Note that the inner time scale can also be rewritten as $t_\delta = O(Fr\,\sigma_y/V_\infty) = O(\frac{\sigma_y}{Nh_m})$. This suggests another interpretation of t_δ as the time taken by columnar internal wave modes (c.f. Baines, 1987) of vertical scale h_m and speed $O(Nh_m/\pi)$ to propagate an upstream distance σ_y. These columnar modes promote flow blocking below $z = h_m - \delta$ and an accelerated overflow across the crest.

Beneath the blocking level, the upstream flow eventually evolves to a layer-wise horizontal potential flow (e.g. Drazin, 1961). Thus the half-length σ_x of the ridge is the appropriate outer length scale. Assuming that flow splitting is also accomplished by columnar internal wave modes of vertical scale h_m that communicate the finite extent of the ridge to a distance of about σ_x upstream,

$$t_\beta = \frac{\sigma_x}{Nh_m/\pi}, \tag{2.2}$$

is an outer time scale for the low-level splitting flow. A summary of these key dimensional scales and non-dimensional parameters is provided in Table 2.1.

A factor that influences the fate of plunging downslope flows is the presence or absence of a dense, cold pool downstream of the crest. In low Fr flow past finite ridges, the low-level dense fluid in the lee is retained and recirculates slowly. This manifests as a pair of vertcically oriented lee vortices that have been observed in numerical simulations (e.g. Smolarkiewicz and Rotunno, 1989) and laboratory experiments (Hunt and Snyder, 1980). As we will see, the retention of a

Table 2.1: Summary of important dimensional inner and outer variables and dimensionless flow parameters.

Dimensional outer parameters		
V_∞	Basic flow speed	[m/s]
N	Background stratification	[1/s]
h_m	Ridge height	[m]
σ_y	Streamwise ridge half-width	[m]
$T = \sigma_y / V_\infty$	Outer excursion time scale	[s]
σ_x	Cross-stream ridge half-length	[m]
σ_x^*	Length of lateral end/connecting sections	[m]
$t_\beta = \sigma_x / (N h_m / \pi)$	Outer flow-splitting time scale	[s]
Dimensional inner parameters based on the ‘Blocking scale’		
$\delta \approx V_\infty / N$	Blocking scale	[m]
$h_m - \delta$	Blocking level	[m]
σ_{y_δ}	Streamwise ridge half-width at blocking level	[m]
$t_\delta = \sigma_{y_\delta} / V_\infty$	Inner excursion time scale	[s]
Dimensionless outer quantities		
$Fr = V_\infty / N h_m \ll 1$	Topographic Froude number	
$\beta = \sigma_x / \sigma_y$	Scaled ridge length	
$t' = t / T$	Scaled outer excursion time	
$t'_\beta = t / t_\beta$	Scaled outer splitting time	
Dimensionless inner quantities		
$Fr_\delta = V_\infty / N\delta \approx 1$	Overflow Froude number	
$\beta_\delta = \sigma_x / \sigma_{y_\delta}$	Scaled dynamic ridge length for the overflow	
$t'_\delta = t / t_\delta$	Scaled inner time	

cold pool inhibits plunging in the lee.

Drazin (1961) developed asymptotic solutions for flows with $Fr \ll 1$ in which, to leading order in small Fr, the steady state is a layer-wise potential flow at all depths below the blocking level. However, this steady asymptotic solution doesn't give insight into the mechanisms or time scales involved in its establishment, nor does it contain a vortical wake structure. Epifanio and Durran (2001) considered long ridges with β up to 12 focussing their attention on the unblocked flow regime, $Fr \geq 1$ for which $\beta_\delta = \beta$. Flows with $Fr < 1$ over obstacles with $O(1)$ horizontal aspect ratios have been studied by a number of authors (e.g. Smolarkiewicz and Rotunno, 1989; Hunt and Snyder, 1980; Hanazaki, 1988). In this regime, splitting flows are established quickly; consequently 2D solutions are not very useful in characterizing them. Previous investigations of low Fr flow past elongated ridges have been confined to moderate values of $\beta \leq 5$ (Bauer et al., 2000; Ólafsson and Bougeault, 1996). The linear regime diagram of Smith (1989) provides some guidance as to the Fr and β ranges over which one might expect 'wave-breaking' and 'flow splitting' but as pointed out by Smith (1989) and others (Bauer et al., 2000; Ólafsson and Bougeault, 1996) there are uncertainties associated with the regime boundaries for low Fr and large β.

To investigate the extent to which flow features characteristic of the infinite ridge solution such as crest control and streamwise asymmetry are seen in low Fr flows past long but finite ridges, we performed a suite of numerical experiments. We first consider a $Fr = 0.16$ flow over an infinite ridge and demonstrate that, by prescribing a uniform outflow with a radiation condition upstream, the flow rapidly evolves towards the optimally controlled downslope flow of Winters and Armi (2014). We then consider the same flow over a finite ridge with steep ends for which $\beta = 30$. We show that the streamwise flow near the ridge center is well described as an infinite ridge overflow for a finite time after which it starts to diverge owing to splitting effects. We quantify the evolution by measuring the volume transport in the overflow as a function of time. Over longer $O(t_\beta)$ time scales, we show that, by reformulating the overflow transport to account for lateral flow splitting, the late-time flow ‘over’ the ridge can still be described by stratified hydraulic theory. Finally, considering an example of a ridge with an abrupt change in height, we demonstrate how these general principles can be extended to predict the overflow across non-uniform ridges.

2.2 Modelling approach

We consider three dimensional, non-rotating, incompressible flow, with free-slip boundary conditions on the ridge surface. The numerical experiments are performed using the spectral large eddy solver described in Winters and de la Fuente (2012), with the bottom topography incorporated as a smooth immersed boundary. The goal is to capture the essentially inviscid dynamics at the large scales of the flow. To this end, we employ a sixth order hyperdiffussion operator to explicitly diffuse only the motions near the smallest grid scale. At rest, the fluid is in hydrostatic balance everywhere, with

$$\frac{\partial \overline{p}_0(z)}{\partial z} = -\overline{\rho}_0(z) g \tag{2.3}$$

where $\overline{p}_0(z)$ is the static pressure, $\overline{\rho}_0(z)$ is the initial density profile and g is the acceleration due to gravity. The fluid is stably stratified with uniform buoyancy frequency N and a density difference $\Delta\rho$ across the total fluid depth. Perturbing about this rest state, for the flow in the domain of interest, the non-linear equations of motion in the Boussinesq limit are

$$\frac{\partial \vec{u}}{\partial t} + \vec{u} \cdot \nabla \vec{u} + g \frac{\rho'}{\rho_0} \hat{\mathbf{k}} = -\frac{1}{\rho_0} \nabla p' + \nu^* \mathcal{D} \vec{u}, \tag{2.4a}$$

$$\frac{\partial \rho}{\partial t} + \vec{u} \cdot \nabla \rho = \kappa^* \mathcal{D} \rho, \tag{2.4b}$$

$$\nabla \cdot \vec{u} = 0. \tag{2.4c}$$

Here, $\vec{u}$ is the three dimensional velocity vector and $\hat{\mathbf{k}}$ is the unit vector in the z direction. ρ_0 is a constant reference density, ρ' and p' are the perturbation density and pressure respectively and ρ is the total density,

$$\rho = \rho' + \overline{\rho}_0(z). \tag{2.5}$$

The topography slopes gently in the streamwise direction with $h_m/\sigma_y = 1/6$, rendering the upstream pressure approximately hydrostatic. Note however that we do not invoke the hydrostatic approximation and are thus able to capture $O(1)$ aspect-ratio shear induced overturning motions downstream.

$\mathcal{D}$ is a sixth order hyperdiffusion operator,

$$\mathcal{D} \equiv \left(\frac{\partial^6}{\partial x^6} + \frac{\partial^6}{\partial y^6} + \frac{\partial^6}{\partial z^6} \right) \tag{2.6}$$

and ν^*, κ^* are hyper- viscosity and diffusivity respectively, which are chosen such that grid scale motions decay to $exp(-1)$ their value within a dissipation time scale $T_{diss} = 5\Delta t$, where Δt is the model time step.

2.2.1 Experimental setup

In all our experiments, the vertical height L_z of the domain is taken to be six times the maximum obstacle height. The flow is rapidly accelerated from rest, with the inflow conditions being ramped up to their desired values over $10\Delta t$.

Infinite ridge experiment

We consider a flow with topographic Froude number $Fr = 0.16$ incident on an infinite Gaussian ridge ($\beta = \infty$) centered at $y = 0$,

$$h = h_m \exp\left(-\frac{y^2}{{\sigma_y}^2}\right). \tag{2.7}$$

Given Fr, the half-width at blocking depth, σ_{y_δ} is found by substituting $h = h_m - \delta \approx h_m - V_\infty/N = h_m(1 - Fr)$ in the LHS of Eq. (2.7), giving for $Fr = 0.16$,

$$\sigma_{y_\delta} \approx \sigma_y/2.5. \tag{2.8}$$

We set $\sigma_y = 6h_m$ and the domain width $L_y = 16.7\sigma_y$, with grid spacing $\Delta y = 0.038\sigma_{y_\delta}$ and $\Delta z = 0.1\delta$. With respect to the inner time scale t_δ, we declare that the flow has reached quasi-steady state when its bulk properties, namely overflow transport, thickness and peak speed at the blocking location deviate by less than 1% over $5t_\delta$. The flow reached quasi-steady state by $t = 31.3t_\delta$, and the run was terminated at $t = 47.6t_\delta$.

Finite ridge experiment

For the finite ridge configuration (see Fig. 2.2), Fr is again set to 0.16 and the ridge height is specified as,

$$h = \left[h_1 + 0.5\Delta h\left(1 + \tanh\frac{(\sigma_x - |x|)}{\sigma_x^*}\right)\right]\exp\left(-\frac{y^2}{\sigma_y^2}\right), \tag{2.9}$$

where $h_1 = 0$, $\Delta h = h_m$ and $\beta = \sigma_x/\sigma_y = 30$. The ends are steep, with $\sigma_x^* = \sigma_x/120$. We exploit the symmetry of the flow configuration to compute the flow on the half domain $x \geq 0$ only, with $x = 0$ treated as a symmetry boundary. To capture lateral flow splitting, we perform the

Table 2.2: Numerical implementation details for each of the flow experiments.

	Infinite ridge ($\beta = \infty$)	*Finite ridge* ($\beta = 30$)	*Two-level ridge*
Ridge configuration			
σ_y	$6h_m$	$6h_m$	$6(h_1 + \Delta h)$
σ_x	-	$30\sigma_y$	$30\sigma_y$
σ_x^*	-	$0.25\sigma_y$	$0.25\sigma_y$
Computational domain			
L_y	$16.7\sigma_y$	$140\sigma_y$	$140\sigma_y$
$L_x/2$	-	$4.7\sigma_x$	$4.7\sigma_x$
L_z	$6h_m$	$6h_m$	$6(h_1 + \Delta h)$
Grid configuration			
Δy	$0.038\sigma_{y_\delta}$	$0.125\sigma_{y_\delta}$	$0.23\sigma_{y_\delta}$
Δx	-	$0.018\sigma_x$	$0.009\sigma_x$
Δz	0.1δ	0.1δ	0.2δ
Inflow/outflow sponge layer thickness	$52\Delta y$	$135\Delta y$	$74\Delta y$
Upper sponge layer thickness	$0.3L_z$	$0.3L_z$	$0.3L_z$
Time step			
Δt	$1.6 \times 10^{-4} t_\delta$	$8.9 \times 10^{-4} t_\delta$	$1.1 \times 10^{-3} t_\delta$

experiment in a large horizontal domain with inflow and outflow channel lengths set to values slightly bigger than $2\sigma_x$ and the lateral half length, $L_x/2$ set to $4.7\sigma_x$. The boundary condition at the lateral boundary $x = 4.7\sigma_x$ is approximated as no-normal-flow, $u = 0$ along with zero normal gradients on streamwise velocity, pressure and density.

The grid resolution is $\Delta y = 0.125\sigma_{y_\delta}, \Delta x = 0.018\sigma_x$ and $\Delta z = 0.1\delta$ and the run was terminated at $t = 48.9t_\delta$. A summary of the computational details for each experiment is given in Table 2.2.

2.2.2 Near-boundary forcing

A sponge layer of thickness $L_z/3$ is imposed at the upper boundary through a Rayleigh damping term that absorbs upward radiating waves. Inflow and outflow boundary conditions are implemented as sponging terms that relax to the specified target values over $O(10 - 100)\Delta y$. The outflow boundary condition is uniform withdrawal at speed V_∞.

Low Fr flows over topography excite internal waves that propagate upstream and alter the oncoming flow. So specifying a uniform inflow condition at the upstream boundary will cause wave reflections that may contaminate the solution in the domain interior, particularly if the inflow channel is not very long. For this reason we apply a radiation condition upstream that maintains the depth integrated transport while allowing the vertical profile of the inflow to evolve in time as upstream propagating waves escape the domain. This is implemented through an iterative scheme that measures the upstream influence at an intermediate location between the ridge center $y = 0$ and inflow boundary $y = -L_y/2$. This information is then utilized in a dynamically evolving boundary condition that is imposed via relaxation,

$$v^{i+1}_{-L_y/2}(x,z) = \alpha v^{i}_{-L_y/2}(x,z) + (1-\alpha)v_{y^*}(x,z), \tag{2.10a}$$

and similarly for u and ρ. Here, i is the time step, y^* is the intermediate position ($-L_y/2 < y^* < 0$) where the flow is measured and α is a weighting parameter. In the finite ridge case, a constraint on the choice of y^* is that it is at least a distance $2\sigma_x$ away from the obstacle. The physical basis for the scheme is that the energy of the upstream propagating signals is primarily contained in columnar internal wave modes (c.f. Baines, 1987), having vertical scale h_m and group velocity $O(Nh_m/\pi)$. The parameter α is therefore chosen as follows. We determine the number of time steps n^* it takes for a columnar mode with group velocity $4Nh_m/\pi$ wave to travel from y^* to the upstream boundary. Then at the time step $i+n^*$, the imposed boundary value $v^{i+n^*}_{-L_y/2}(x,z)$ derives 90% of its information from the measured profile at time step i, $v^{i}_{y^*}(x,z)$. That is,

$$1-\alpha^{n^*} = 0.9 \tag{2.11}$$

We found this scheme to be robust for different choices of α. For example, changing the RHS of Eq. (2.11) from 0.9 to 0.8 produced a negligible change in the bulk properties of the flow. The advantage of this scheme is that it allows for a much shorter inflow channel length than would be possible with a more traditional approach of imposing a uniform inflow condition and a deep sponge layer to radiate upstream disturbances. We have performed a test run for the infinite ridge case using the latter approach and verified that the results match the ones obtained using the iterative scheme above.

2.3 A brief overview of the Winters and Armi (2014) analysis

Winters and Armi (2014) developed semi-analytical solutions for hydraulically controlled flow over an infinite ridge. The solution begins by considering a uniform stratification N and jet-like upstream flow profiles of specified thickness H overlying a stagnant blocked layer, as shown in Fig. 2.1. Note that this approach is different from the hydraulic treatment of Smith (1985) in that it includes the effect of upstream blocking. Asymmetry is triggered by imposing a streamline bifurcation upstream at the top of the jet-like flow. The downslope flow below the lower branch of the bifurcating streamline is then calculated through integrals of Bernoulli's equation. For a chosen upstream wind profile, the bottmmost streamline which represents the terrain surface is thus determined by the dynamics rather then being imposed *a priori*.

Among different jet-like upstream flow configurations considered, it was found that a parabolically sheared velocity profile with a velocity maximum $(3/2)NH/\pi$ and associated volume transport NH^2/π was optimal in the sense that it maximized the blocking scale δ while minimizing the kinetic energy of the flow.

Note that, although the overflow thickness H is assumed *a priori* in constructing the optimal solution, H and the transport Q of the overflow are in fact coupled through the control relationship,

$$Q = NH^2/\pi. \tag{2.12}$$

As we will see below, predicting H from Eq. (2.12) requires an estimation of the overflow transport Q. Winters and Armi (2014) also found that the blocking scale is dynamically related to the overflow thickness as $\delta = H/8$.

An important property of the solution is that, on either side of the crest, it generates a unique one-to-one mapping between the height by which the bifurcating streamline has dropped and the terrain height relative to the blocking level. It is thus a valid solution for arbitrary terrain shapes (Appendix A). As in all hydraulic models, the solution of Bernoulli's equation relies on the hydrostatic approximation and thus the precise shape of the bifurcating streamline is unimportant as long as its slope is small. Upstream of the blocking location, the terrain shape is arbitrary and is not part of the solution.

Finally, internal hydraulic jumps are not included in this model and so the bifurcating streamline is perpetually plunging over an apparently 'bottomless' terrain. However for real ridges, the downslope flow must return to a subcritical state at some location downstream of the crest. The Winters and Armi (2014) solutions are formally valid until this location.

2.4 Diagnostics of the overflow

Volume transport conservation (see also Fig. 2.1) requires that, at the blocking location, the transport within the overflow between $z = h_m - \delta$ and $z = h_m - \delta + H$ match the far upstream transport below the bifurcating streamline. That is,

$$NH^2/\pi = V_\infty \left(h_m - \delta + H\right). \tag{2.13}$$

Substituting $\delta = H/8$ in Eq. (2.13) yields a quadratic for H, with coefficients given in terms of the outer dimensional parameters h_m, N and V_∞,

$$NH^2/\pi = V_\infty \left(h_m + 7H/8\right). \tag{2.14}$$

Note that H obtained by solving the quadratic Eq. (2.14) is the analytical prediction of the overflow thickness in the infinite ridge limit. When the ridge is finite, the fluid below $z = h_m - \delta$ can escape around the sides and the overflow transport and thickness shrink accordingly. To quantitatively compare this overflow with the infinite ridge prediction, we define the volume transport per unit length in a layer of height H starting at the blocking level $z = h_m - \delta$ and measured at the upstream blocking location $y = -y_b$ (indicated in Fig. 2.1),

$$Q'(x,t) = \int_{h_m-\delta}^{h_m-\delta+H} v(x,-y_b,z,t)\,\mathrm{d}z, \tag{2.15}$$

For an infinite ridge, the overflow transport is independent of x and $Q'(x,t)$ reduces to $Q'(t)$. In this case we expect upstream blocking to cause an early surge in the overflow transport, with $Q'(t)$ quickly approaching Q. For a long but finite ridge, we anticipate that $Q'(x,t)$ will approach Q at early times before it starts decreasing as transport is lost to the low-level lateral splitting flow.

As a quantitative measure of asymmetry, we compare the maximum speed at the downstream location $y = y_b$ (indicated in Fig. 2.1) to the reference speed V_∞. An additional measure of asymmetry is the plunging depth $p_d(x,t)$, defined as the depth from the ridge crest to which the streamline originating at the upstream blocking level $z = h_m - \delta$, plunges down the lee slope before it separates.

2.5 Results

We will evaluate the temporal evolution of the diagnostics developed in section 2.4. For a long ridge ($\beta \gg 1$), the inner excursion time scale t_δ is much shorter than the outer flow splitting time scale t_β. Accordingly, we define a scaled inner time

$$t'_\delta = t/t_\delta \tag{2.16}$$

to quantify the near-crest evolution of the overflow and a scaled outer splitting time

$$t'_\beta = t/t_\beta \tag{2.17}$$

to quantify the development of the low-level horizontal splitting flow.

Upstream blocking, streamwise across-crest asymmetry, overturned isopycnals and downslope flow acceleration will be visible in planar vertical sections. We will also show images of horizontal sections which will reveal the establishment of low-level flow-splitting.

2.5.1 Infinite ridge ($\beta = \infty$)

We first present results for flow over an infinite ridge with $\beta_\delta = \beta = \infty$ and $Fr = 0.16$. The blocking scale for this flow is $\delta \approx V_\infty/N = 0.16h_m$. Thus most of the air upstream and below the ridge crest is blocked.

Fig. 2.3a,b show that with respect to the inner time scale, the upstream flow rapidly evolves to that predicted by 2D theory. By $t'_\delta = 2$, the velocity profile at the blocking location already begins to approach the analytically predicted parabolic profile of Winters and Armi (2014). By $t'_\delta = 11.7$, the overflow has evolved further towards a parabolic shape and both its peak speed and volume transport are within 10% of the analytically predicted values. Later, at $t'_\delta = 31.1$, the peak speed matches the prediction exactly. We remark that the dynamical prediction for the blocking scale δ obtained from solving for H in Eq. (2.12) yielded a value that is about 25% smaller than the initial scaling estimate V_∞/N.

The time history of $v_{max}(y_b)/V_\infty$ is also shown in Fig. 2.3b (in red) along with the Winters

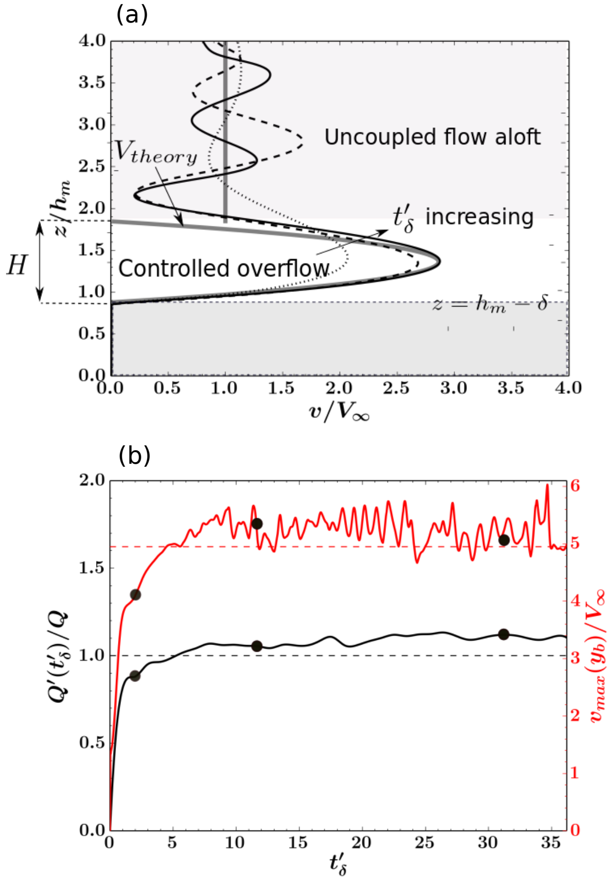

Figure 2.3: (a) Vertical profiles of the streamwise velocity at the blocking point $y \approx -y_b$ at $t'_\delta = 2.0, 11.7$ and 31.1 along with the analytical prediction of Winters and Armi (2014) (plotted in grey) for $Fr = 0.16$ flow over an infinite ridge. H is the Winters and Armi (2014) prediction of the overflow thickness. (b) Upstream volume transport $Q'(t'_\delta)$ (black) in the controlled overflowing layer normalized by the theoretical value Q and normalized maximum streamwise velocity, $v_{max}(y_b, z, t'_\delta)/V_\infty$ (red) at the downstream location y_b, Vs dimensionless time, t'_δ. Dots mark the times at which velocity profiles are shown in Fig. 2.3a and dashed lines are the analytical predictions of Winters and Armi (2014). The location of y_b relative to the ridge crest is indicated in Fig. 2.1.

and Armi (2014) prediction. These infinite-ridge solutions are highly asymmetric as indicated by sustained downslope flow speeds of about $5V_\infty$ with gusts approaching $6V_\infty$. These gusts are quasi-periodic with a period of about t_δ, which for this specific ridge configuration and Fr is roughly two buoyancy periods. They are reminiscent of the quasi-periodic gusts observed in the Bora by Beluši'c et al. (2004) and arise due to Kelvin-Helmholtz (K-H) instability, caused by increasing shear downstream at the top of the overflowing layer (Peltier and Scinocca, 1990; Jagannathan et al., 2017).

Fig. 2.4a-c shows the flow evolution as it approaches a quasi-steady state. Blocking is already visible by $t'_\delta \approx 2$ and the upstream extent of the blocked flow increases with time. By $t'_\delta = 11.7$, upstream influence in the form of long internal gravity waves has permanently modified the incoming flow, shaping the flow above the blocking level into a parabolic jet. Overturning isopycnals are seen above the crest and further downstream, a plunging downslope flow develops. Both the maximum downslope flow speed and its penetration depth increase with time. The instantaneous snapshot in Fig. 2.4b reveals turbulent overturns, both aloft and due to K-H instability at the top of the unstable overflowing layer (Peltier and Scinocca, 1990; Jagannathan et al., 2017). The numerical model, which removes grid-scale variability via the hyperdiffusion operator $\mathcal{D}$ does not completely resolve the details of the turbulent mixing due to these processes. Nevertheless, as shown in Fig. 2.4c, a statistical time-average of the quasi-steady flow reveals the essential downstream flow features, which are an accelerating downslope flow and a nearly stagnant, nearly homogeneous isolating layer that separates the downslope flow from the flow aloft. Comparison with Fig. 2.4b shows that the statistical averaging has no discernible effect on the stable upstream flow.

In their theory, Winters and Armi (2014) do not prescribe a structure for the flow above the overflowing layer, which they assume to be dynamically uncoupled with a mean speed V_∞. We note that the computed solutions in Fig. 2.4 as well as the vertical profiles of $v(-y_b, z, t_\delta)$ in Fig. 2.3a show weak spatial oscillations about this mean which merge smoothly with the jet-like

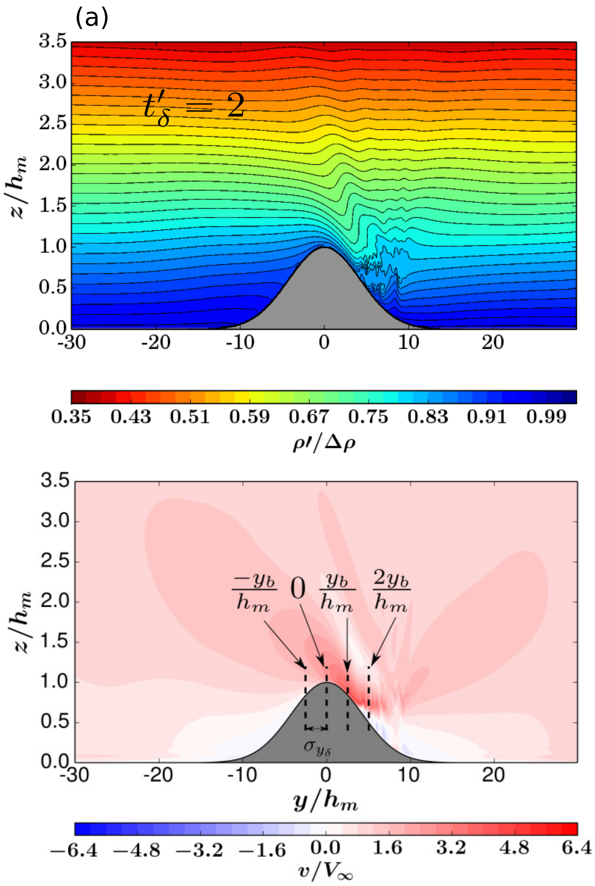

Figure 2.4: Time evolution of the flow field for $Fr = 0.16$ flow over an infinite ridge. (Top) Isopycnal lines and contours and (bottom) streamwise velocity contours. The lower panel indicates the position of the blocking location, ridge center and downstream locations at which we will later (in Fig. 2.5) display the vertical profiles of the streamwise velocity. Flow is from left to right. (a) $t'_\delta = 2$; (b) $t'_\delta = 11.7$ and (c) Averaged over $31.1 \leq t'_\delta \leq 47.2$.

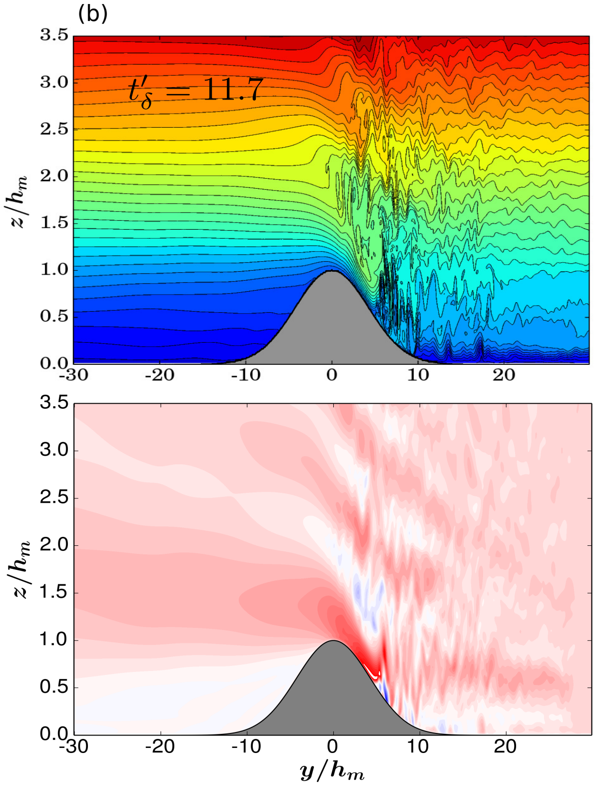

Figure 2.4: Time evolution of the flow field for $Fr = 0.16$ flow over an infinite ridge (Continued).

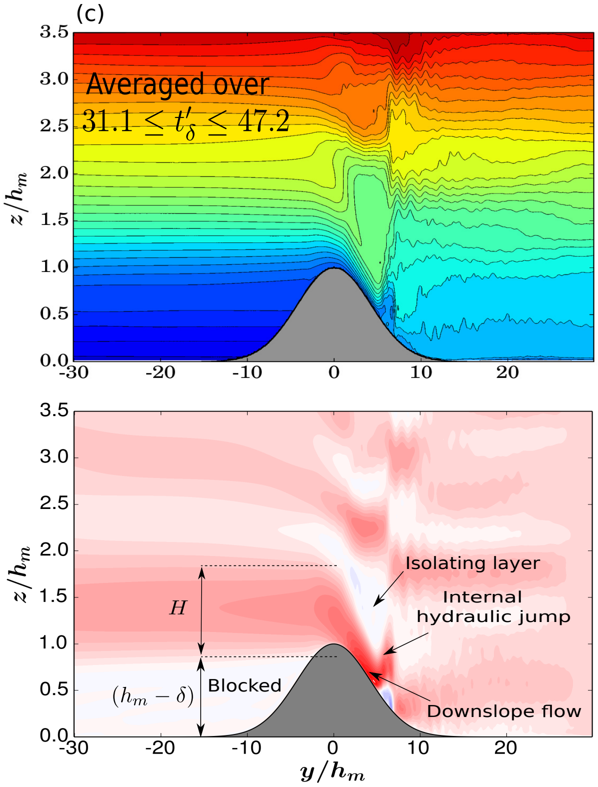

Figure 2.4: Time evolution of the flow field for $Fr = 0.16$ flow over an infinite ridge (Continued).

overflow. We have checked that the quantitative features of the controlled overflowing layer as well as the characteristic wavelength ($\approx 2\pi V_\infty/N$) of the oscillations aloft are insensitive to the height of the model domain and the thickness of the sponge layer (Appendix B).

Across-crest asymmetry sets in early (Fig. 2.4a) and the stratification becomes increasingly asymmetric across the crest as the flow evolves. By $t'_\delta = 11.7$ (Fig. 2.4b), the dense air downstream and below the blocking level $z = (h_m - \delta)$ has been almost completely swept away and is replaced by lighter air that has overflowed the crest. This asymmetry in the density field is a consequence of upstream flow blocking and is directly related to the establishment of hydraulic control at the crest. The supercritical flow downstream manifests as an intensifying downslope windstorm.

Depth profiles of the streamwise velocity at and downstream of the crest elucidate the characteristics of the downslope flow. These are displayed at an early and late inner-time in Fig. 2.5. The maximum speed $v_{max}(y)$ increases downstream and with time at each location as the flow evolves towards a quasi-steady state. At later times, e.g. $t'_\delta \approx 31.9$, the overflow thins and accelerates downstream of the crest. It also progressively plunges deeper in the lee. For example, $v_{max}(2y_b) \approx 6.3V_\infty$ and the vertical location of the maximum is at $z \approx 0.6h_m$ which is a depth of about 2.5δ below crest level. This shows that the flow is highly asymmetric across the crest.

The evolution of the plunging depth $p_d(t'_\delta)$ of the lowest streamline cresting the obstacle is traced in Fig. 2.6. The plunging depth reaches sustained values of about 3δ by $t'_\delta \approx 4$ and subsequently fluctuates between 2.5δ and 3.9δ. The fluctuations are associated with the internal hydraulic jump downstream of the separation location.

In summary, low Fr flow over infinite ridges is highly asymmetric across the crest, with respect to both streamwise velocity and stratification. It is characterized by upstream flow blocking and the development of a thinning accelerating downslope flow that plunges down the lee slope to a significant fraction of the ridge height. Within the overflowing layer, the properties of the quasi-steady flow are well described by the stratified hydraulic theory of Winters and Armi (2014).

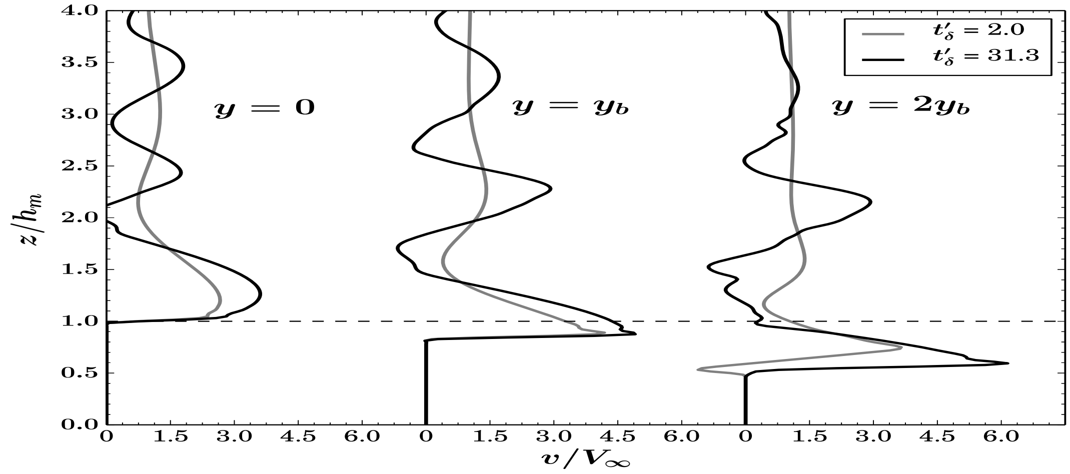

Figure 2.5: Vertical profiles of streamwise velocity $v(y, z, t'_\delta)$ at various positions downstream of the upstream blocking location $-y_b$ for the infinite ridge overflow at $Fr = 0.16$. The positions of the downstream locations relative to the ridge center are indicated in the bottom panel of Fig. 2.4a.

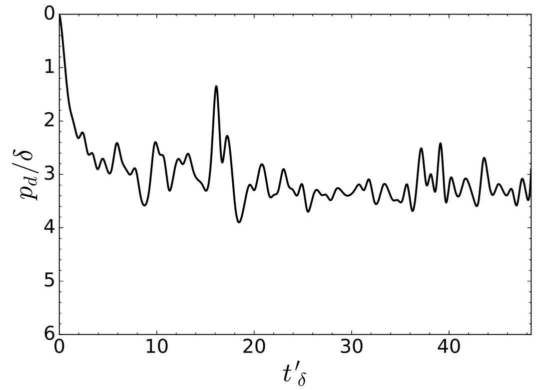

Figure 2.6: Plunging depth, $p_d(t'_\delta)$ of the lowest streamline that crests the obstacle for $Fr = 0.16$ flow over an infinite ridge.

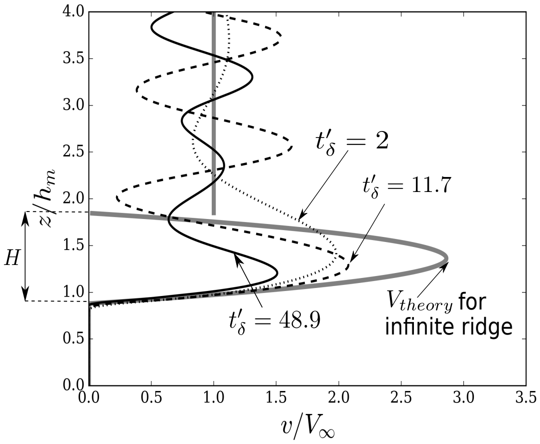

Figure 2.7: Vertical profiles of the streamwise velocity $v(z,t'_\delta)$ in the centerplane $x = 0$ at the blocking point $y = -y_b$ for $Fr = 0.16$ flow over a finite ridge with $\beta = 30$. The corresponding Winters and Armi (2014) prediction for the infinite ridge case at the same Fr is shown in grey, with H being the predicted overflow thickness.

2.5.2 Finite ridge ($\beta = 30$)

We now consider a flow with identical forcing and Froude number incident on a long, but finite ridge with $\beta = 30$. The finite extent allows for both flow ‘over’ and ‘around’ the ridge and we proceed to quantify how the flow characteristics differ from the infinite ridge case for which a purely 2D controlled overflow develops. The shape of the ridge is described by Eq. (2.9) with $h_1 = 0$, $\Delta h = h_m$ and $\sigma_x^* = \sigma_y/4$. (see also Fig. 2.2). We examine the evolution of the overflow in the centerplane and at a plane closer to the lateral ends (shown in Fig. 2.2).

The upstream flow which crests the obstacle originates at or above the blocking level $h_m - \delta$. Hence the appropriate streamwise length scale for flow ‘over’ the crest is σ_{y_δ}, the ridge half-width at blocking level. The scaled dynamic ridge length for the overflow $\beta_\delta = \sigma_x/\sigma_{y_\delta}$ is ≈ 75, which is larger than the geometric scaled length $\beta = 30$ for flow around the sides.

Further, while the topographic Froude number $Fr = 0.16$, the appropriate Froude number for the overflow is $Fr_\delta = V_\infty/N\delta \approx 1$. Our case is dynamically distinct from $Fr \approx 1$ flows for which $\beta_\delta = \beta$ and $Fr_\delta = Fr$ (e.g. Epifanio and Durran, 2001).

Fig. 2.7 traces the evolution of the streamwise velocity at the upstream blocking location, $v(-y_b, z, t'_\delta)$ in the symmetric centerplane $x = 0$. At early times (e.g. $t'_\delta = 2$), the flow profile is nearly identical to that in the infinite ridge case (Fig. 2.3a). By $t'_\delta = 11.7$, the profile is similar in structure to the infinite ridge overflow, but with a lower peak speed. Much later (e.g. $t'_\delta = 48.9$), the overflow is considerably thinner and slower than that in the infinite ridge case. This is because much of the transport associated with the early-time overflow is lost to the low-level horizontal splitting flow. We will show that by a simple reduction of the upstream volume transport in Eq. (2.13), the long-time flow 'over' the ridge can be qualitatively and quantitaively described as an asymmetric crest-controlled overflow.

Figs. 2.8 and 2.9 show the evolution of the flow field at and away from the ridge centerplane respectively. The stratification and streamwise velocity exhibit asymmetry across the crest in the form of an intensifying downslope flow. Isopycnals overturn above the crest and the flow accelerates as it plunges down the lee slope. At early ($t'_\delta = 2$) and intermediate ($t'_\delta = 11.7$) times the flow field in the centerplane is strongly reminiscent of the infinite ridge solution.

At later times, e.g. $t'_\delta = 48.9$ ($t'_\beta = 1.3$), the fluid in the lee beneath the blocking level is nearly motionless, both at and away from the centerplane (Figs. 2.8c and 2.9c). Downslope plunging is strongly inhibited and the stratification below the overflow is nearly symmetric across the crest. The initial dense 'cold pool' in the lee is retained on the long flow splitting time scale. This contrasts strikingly with the infinite ridge solution (Fig. 2.4) where the density field becomes highly asymmetric across the crest as the downslope flow evolves. Above the blocking level, the flow is streamwise asymmetric, both at and away from the centerplane. This is a clear signature of hydraulic control at the crest. Recall, in addition, that the overflow Froude number $Fr_\delta \approx 1$.

The evolution of horizontal streamlines at $z = 0.1h_m$ (i.e. well below the blocking level) is depicted in Fig. 2.10a-c. At early outer times (e.g. $t'_\beta = 0.05$), the low-level flow is blocked immediately upstream of the ridge. Subsequently, the upstream flow splits laterally around the sides, with speeds of about $2V_\infty$ at the obstacle ends and approaching $3V_\infty$ further downstream.

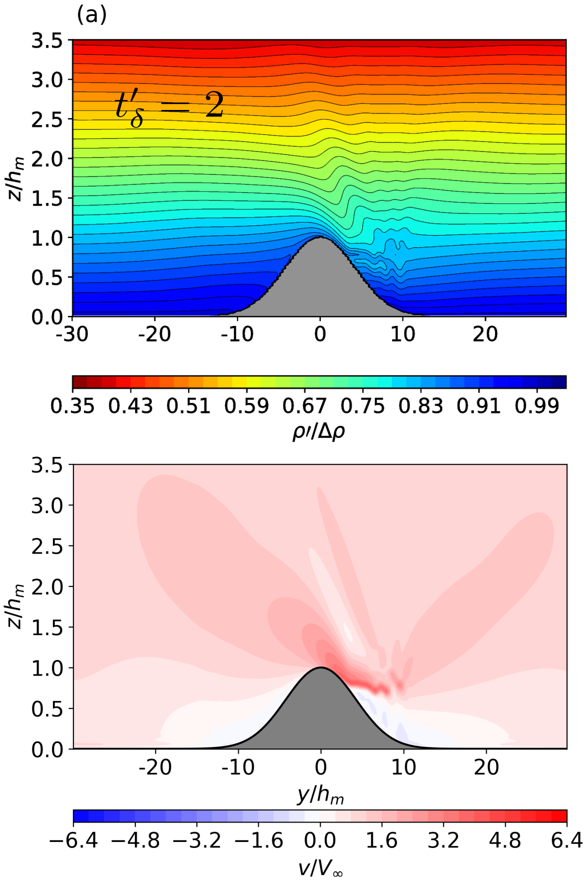

Figure 2.8: Time evolution of the flow field at the symmetric centerplane, $x = 0$ for $Fr = 0.16$ flow over a finite ridge with $\beta = 30$. (Top) Isopycnal lines and contours and (bottom) streamwise velocity contours. Flow is from left to right. (a) $t'_\delta = 2.0$; (b)$t'_\delta = 11.7$ and (c) $t'_\delta = 48.9$. H_f and δ_f in (c) are the predicted late-time overflow thickness and blocking scale respectively predicted from Eq. (2.22) and Eq. (2.23).

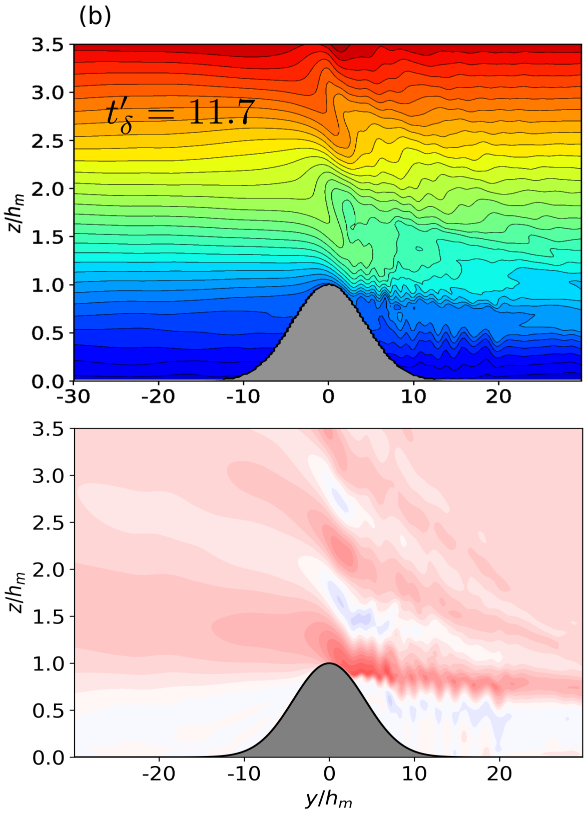

Figure 2.8: Time evolution of the flow field at the symmetric centerplane, $x = 0$ for $Fr = 0.16$ flow over a finite ridge with $\beta = 30$.(Continued)

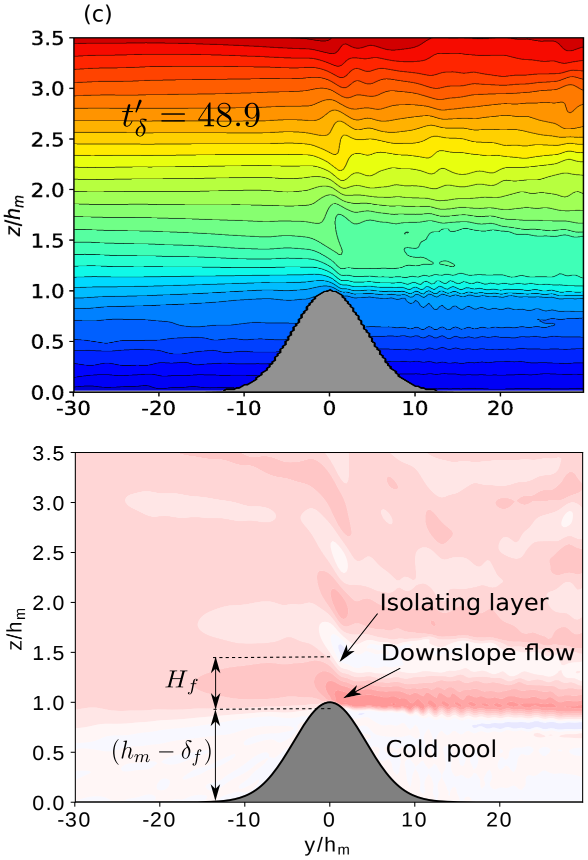

Figure 2.8: Time evolution of the flow field at the symmetric centerplane, $x = 0$ for $Fr = 0.16$ flow over a finite ridge with $\beta = 30$.(Continued)

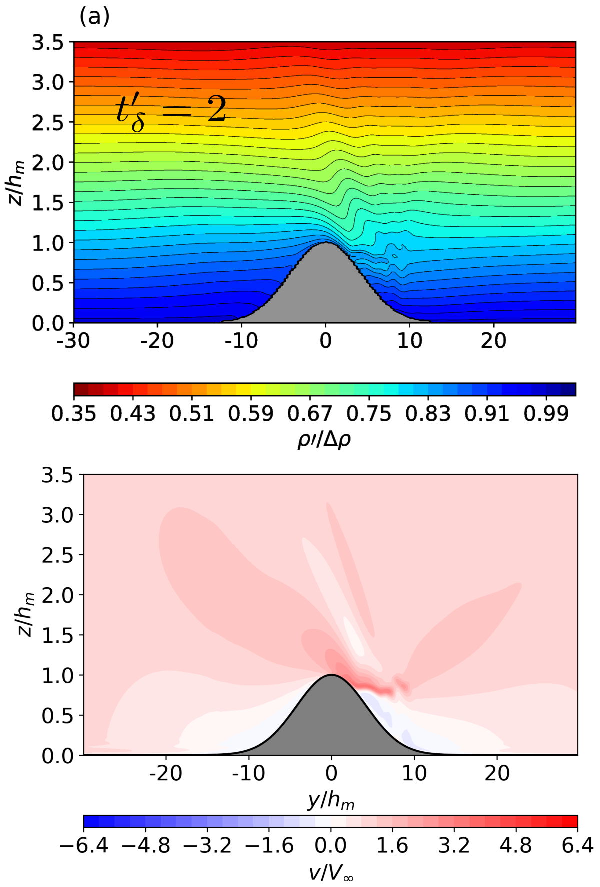

Figure 2.9: Same as Fig. 2.8 but at the cross-stream location $x = 0.93\sigma_x$ at times (a) $t'_\delta = 2.0$; (b) $t'_\delta = 11.7$ and (c) $t'_\delta = 48.9$.

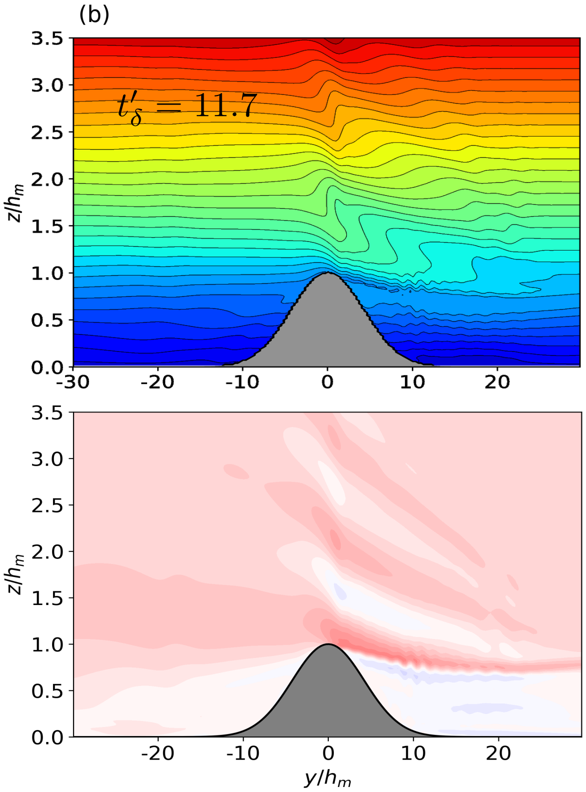

Figure 2.9: Same as Fig. 2.8 but at the cross-stream location $x = 0.93\sigma_x$ (Continued)

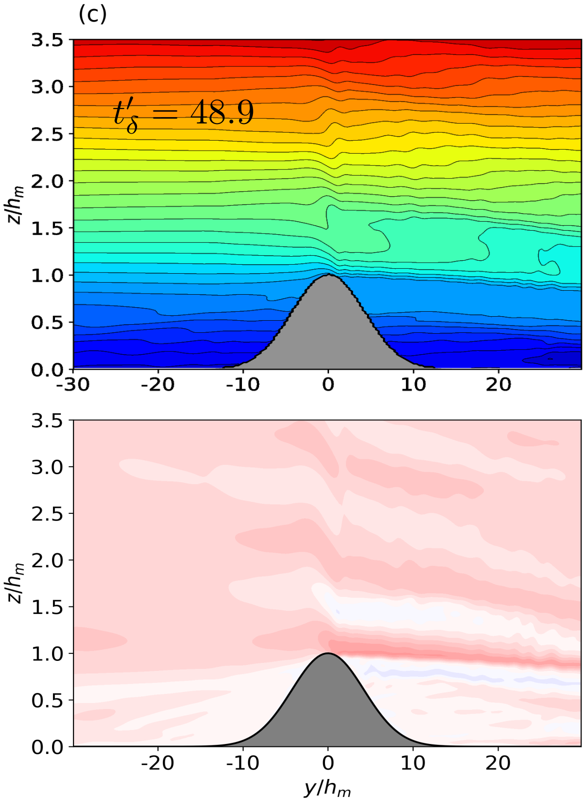

Figure 2.9: Same as Fig. 2.8 but at the cross-stream location $x = 0.93\sigma_x$ (Continued)

In the lee, a vortex pair develops and the vortex centers move downstream with time, forming a slowly recirculating flow within the cold pool.

At low levels upstream, the late-time horizontal splitting flow is a layer-wise potential flow, as proposed by Drazin (1961). For example, at $z = 0.1h_m$, where the ridge half width is $1.5\sigma_y$, Fig. 2.11 shows that $v(x)$ at $y = -1.5\sigma_y$ is well approximated by the expression

$$v(x, y = -1.5\sigma_y) = V_\infty \left(A + B\frac{\sigma_x^2}{x^2} \right), \qquad |x| \geq \sigma_x. \tag{2.18}$$

This is simply the scaling law for potential flow around convex, symmetric 2D obstacles. The constant A is unity for an infinite domain but is slightly larger here due to the presence of side walls. B is a factor that depends on the details of the obstacle shape. For this case, the best fit was obtained with $A = 1.1$ and $B = 1$.

As a consequence of low-level flow splitting, the transport in the overflow is less than the infinite ridge prediction. In Fig. 2.12, we track the upstream transport, $Q'(x = 0, t'_\delta)$ in a layer of thickness H above the blocking level $h_m - \delta$ and compare peak flow speeds at y_b with those for the 2D infinite ridge case. Q' deviates from the infinite ridge curve at $t'_\delta \approx 1$ by which time it is 85% of Q. From around $t'_\delta = 5$, Q' starts decreasing steadily as more and more transport is lost to the low-level splitting flow. Significantly, at $t'_\delta = 12$, Q' and $v_{max}(y_b)$ are close to 75% and 80% of the predicted infinite ridge values. Therefore for $0 < t'_\delta \leq O(10)$, the flow in the centerplane is well described as a controlled infinite ridge overflow.

One distinctive feature of low Fr flows in a purely 2D setting is gustiness of the downslope flow, associated with loss of stability downstream (Jagannathan et al., 2017). This manifests itself as high frequency oscillations in the measured peak downstream speed $v_{max}(y_b)$ (Fig. 2.3b). By contrast, such gustiness is absent in the finite ridge case. Thus the combination of diminished downslope plunging (Fig. 2.8) and loss of overflow transport weakens the downstream shear, thereby stabilizing the flow.

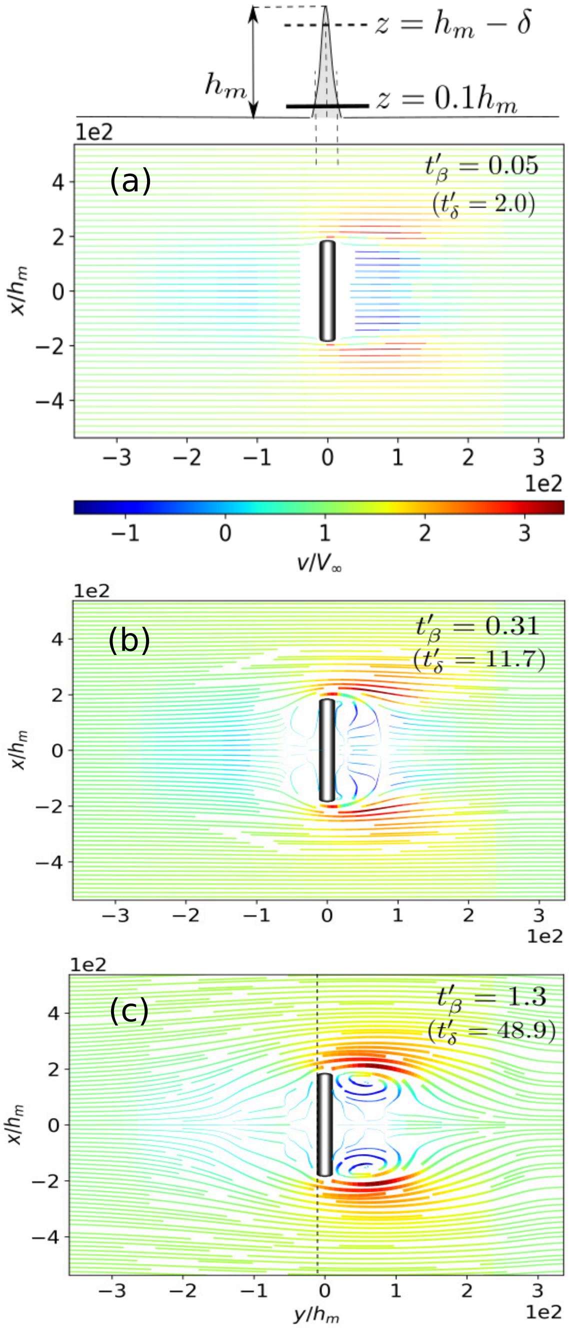

Figure 2.10: Time evolution of streamlines in the horizontal plane at $z = 0.1h_m$, i.e. just above the ground level, for the finite ridge with $\beta = 30$ at $Fr = 0.16$: (a) $t'_\beta = 0.05$; (b) $t'_\beta = 0.31$ and (c) $t'_\beta = 1.3$. Thick red lines indicate fast positive flow and dark blue lines indicate reversed flow.

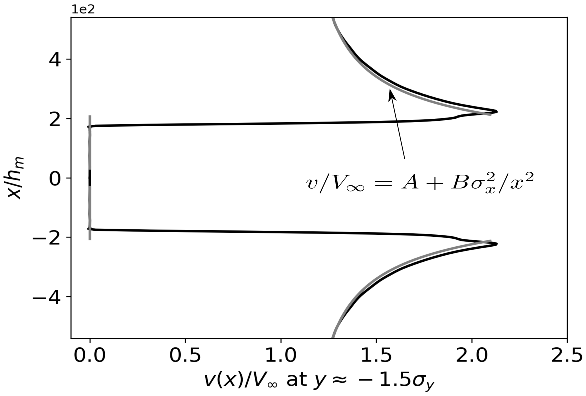

Figure 2.11: Streamwise velocity $v(x)/V_\infty$ at $t'_\beta = 1.3$ at the vertical level $z = 0.1h_m$ and along $y = -1.5\sigma_y$, the half-width of the ridge at $z = 0.1h_m$ (indicated as a dashed line in Fig. 2.10c). Shown in grey is the fit $v/V_\infty = A + B\sigma_x^2/x^2$, with $A = 1.1$ and $B = 1$.

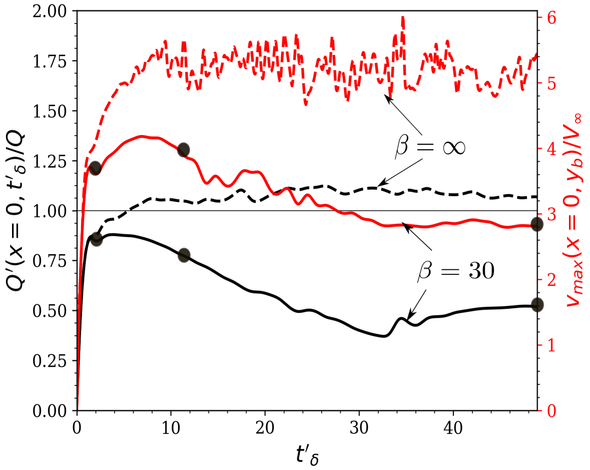

Figure 2.12: Upstream volume transport $Q'(x = 0, t'_\delta)$ (black) of the overflow in the centerplane of the finite ridge, normalized by the infinite ridge prediction, Q; and normalized maximum streamwise velocity $v_{max}(x = 0, y_b, z, t'_\delta)/V_\infty$ (red) at the downstream location y_b. Dots mark the times $t'_\delta = 2.0, 11.7$ and 48.9 for which vertical velocity profiles are shown in Fig. 2.7.

At $t'_\beta = 1.3$ ($t'_\delta = 48.9$), the flow over the crest is still asymmetric both at and away from the centerplane (Fig. 2.8c and 2.9c). By this time, the low-level flow upstream of the ridge has almost entirely split horizontally around the sides of the obstacle (Fig. 2.10c). Thus at each cross-stream section along the ridge, a portion $V_\infty(h_m - \delta)$ of the upstream transport which was absorbed into the overflow at early times is lost to the lateral splitting-flow. This motivates the reformulation of the late-time overflow (Fig. 2.7) with a reduced transport. From its observed across-crest asymmetry, we infer hydraulic control at the crest. Assuming a modified and as yet unknown thickness H_f for this overflow, for optimal control (Winters and Armi, 2014), it must be parabolic in shape, with average speed NH_f/π and transport

$$Q_{H_f} = NH_f^2/\pi. \tag{2.19}$$

This yields a new blocking scale, $\delta_f = H_f/8$. Below $z = h_m - \delta_f$, the upstream flow is predominantly 'around' the ridge. Recall that the length of the end sections $\sigma_x^* \ll \sigma_x$. Therefore from Eq. (2.18), on either side of the centerplane, the excess transport per unit length of the obstacle that escapes around the sides can be written as

$$Q^* \approx \frac{1}{\sigma_x} \int_{\sigma_x}^{\infty} BV_\infty \frac{\sigma_x^2}{x^2} (h_m - \delta_f) \, \mathrm{d}x = V_\infty (h_m - \delta_f), \tag{2.20}$$

for the best-fit value $B = 1$. This is exactly the amount of transport that is blocked ahead of the ridge at early times. For $\beta_\delta \gg 1$, this allows us to estimate the transport lost along each streamwise plane in the ridge interior as $V_\infty(h_m - \delta_f)$. Therefore the late-time transport for the overflow in the ridge interior is simply $V_\infty H_f$. The volume conservation equation Eq. (2.13) then reduces to

$$NH_f^2/\pi = V_\infty H_f, \tag{2.21}$$

giving

$$H_f = \pi V_\infty / N \tag{2.22}$$

and

$$\delta_f = H_f/8 = \frac{\pi V_\infty}{8N}, \tag{2.23}$$

which is more than 2.5 times smaller than the scaling estimate V_∞/N, suggesting that the blocking location moves closer to the crest. These predictions for the quantities H_f and δ_f match the observed late-time overflow reasonably well, as indicated in Fig. 2.8c. We denote the new upstream blocking location as $y = -y_{b_f}$.

When Fr is small as is the case here, most of the upstream fluid below crest level eventually splits around the ridge. This occurs on the slow time scale t_β (Fig. 2.10). Thus H_f is considerably smaller than H, which in turn implies that the late-time overflow has a reduced peak speed and correspondingly reduced kinetic energy relative to that at early-times. The predicted velocity profile at the new upstream blocking location $y = -y_{b_f}$ is shown in Fig. 2.13 along with the computed profile in the centerplane $x = 0$ at $t'_\delta = 48.9 (t'_\beta = 1.3)$. The agreement in the peak speed is within 10% of the newly predicted value. Fig. 2.14 shows the evolution of the transport

$$Q'_{H_f}(t'_\delta) = \int_{h_m-\delta_f}^{h_m-\delta_f+H_f} v(-y_b, z, t'_\delta)\,\mathrm{d}z, \tag{2.24}$$

in a layer of thickness H_f above the blocking level $h_m - \delta_f$ on the centerplane, along with the maximum downslope flow speed $v_{max}(y_b)$. At later times Q'_{H_f} is within 20% of Q_{H_f} while $v_{max}(y_b)$ is within 8% of the Winters and Armi (2014) prediction for H_f. Thus even at later times, the stratified hydraulic framework describes the properties of the overflow well. We note that the integral in Eq. (2.24) slightly overestimates Q'_{H_f}. This is due to the fact that in the computed solution (Fig. 2.13), the overflow merges smoothly with the flow aloft whereas in the theory, there is a discontinuity between these flow components (shown in grey). The essential features of the

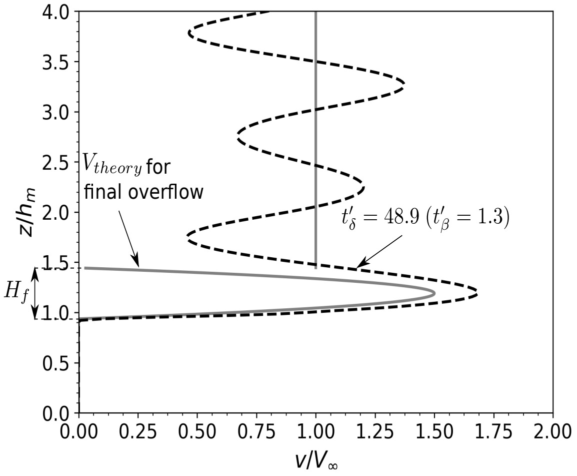

Figure 2.13: Vertical profile of the late-time streamwise velocity in the centerplane $x = 0$ of the finite ridge at the blocking point $y = -y_{b_f}$ along with the predicted profile based on H_f.

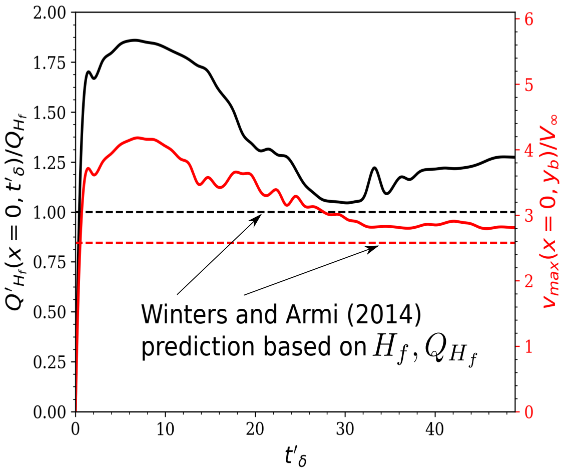

Figure 2.14: (Black) Upstream volume transport $Q'_{H_f}(t'_\delta)$ in a layer of thickness H_f above the blocking level at the centerplane of the finite ridge, normalized by the analytical prediction Q_{H_f} and (red)normalized maximum streamwise velocity, $v_{max}(y_b, z, t'_\delta)/V_\infty$ at the downstream location y_b.

late-time overflow along the centerplane are labelled in Fig. 2.8c.

Vertical downstream profiles of the streamwise velocity (Fig. 2.15) offer another view of the evolving downstream flow in the centerplane $x = 0$ and at $x = 0.93\sigma_x$. The flow characteristics are remarkably similar both at and away from the centerplane. While the early-time downslope flow closely resembles that observed in the infinite ridge case (Fig. 2.5), at later times, the overflow is qualitatively similar, but has reduced transport and kinetic energy. Peak downstream speeds are lower and the locations of the maxima have moved upward to near the crest level $z = h_m$.

The combination of a slower overflow and the retention of a cold pool downstream lead to diminished plunging in the lee at $t'_\beta = O(1)$ (or equivalently, late-inner-times $t'_\delta \gg 1$). This is seen in Fig. 2.16, which shows the time history of the plunging depth, $p_d(x, t'_\delta)$ in each plane, alongside $p_d(t'_\delta)$ for the infinite ridge case. With respect to the inner time scale, the plunging depth overshoots quickly, for example reaching 2.2δ in the centerplane at $t'_\delta \approx 2$. However, on the slower splitting time scale t_β, as the kinetic energy of the overflow decreases (Fig. 2.15), p_d correspondingly levels off to values smaller than δ, both at and away from the centerplane.

We now summarize the results of this section as follows: For $0 < t'_\delta < O(1)$, the development of the flow near the ridge center mimics the 2D infinite ridge overflow, both qualitatively and in terms of the quantitative measures of asymmetry $v_{max}(y_b)$ and p_d. At intermediate times $O(1) < t'_\delta < O(10)$, the qualitative features of the infinite ridge solution persist both at and away from the ridge centerplane, but the quantitative measures begin to deviate from the infinite ridge values. In the centerplane, Q' and $v_{max}(y_b)$ are still 75% of the infinite ridge values for t'_δ as high as 12. On the longer flow-splitting time scale, the energetically weaker overflow is unable to penetrate the cold pool downstream, leading to substantially reduced plunging depths. Nevertheless, across-crest asymmetry and downslope flow acceleration persist above the blocking level. The late-time flow is well-described as an asymmetric crest-controlled overflow lying above a horizontal splitting flow whose upstream properties follow from potential flow theory.

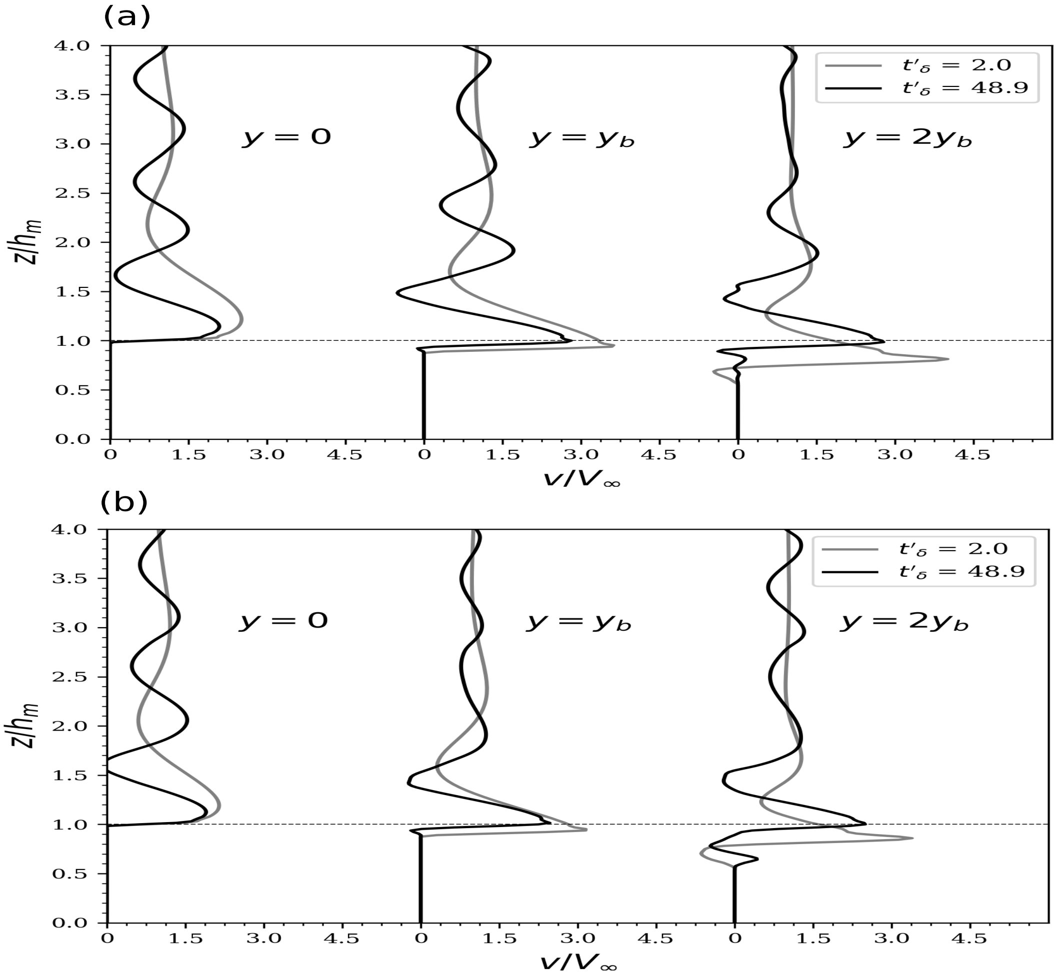

Figure 2.15: Vertical profiles of $v(x,y,z,t'_\delta)$ at various positions downstream of the upstream blocking location $-y_b$ for the finite ridge at two different vertical planes: (a) Centerplane $x = 0$, (b) Away from the centerplane, $x = 0.93\sigma_x$. The cross-stream and streamwise positions of the measurement locations are indicated in Fig. 2.2 and Fig. 2.4a respectively.

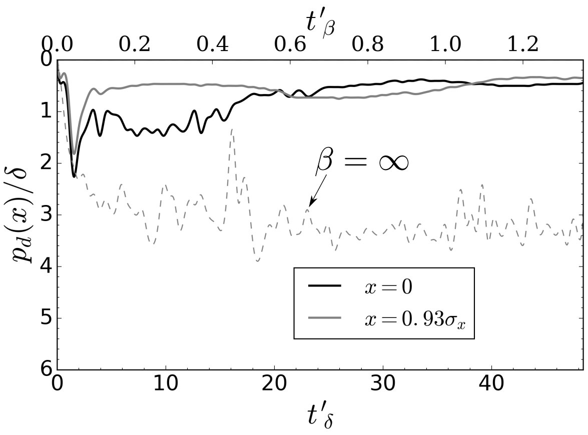

Figure 2.16: Plunging depth, $p_d(x, t'_\delta)$ of the lowest streamline that crests the obstacle for the overflow across a finite ridge with $\beta = 30$ at $Fr = 0.16$. Also shown is $p_d(t'_\delta)$ for the corresponding infinite ridge case.

2.6 Discussion

2.6.1 Applicability of the stratified hydraulic framework

Asymmetry and hydraulic control form the dynamical basis of the infinite ridge theory of Winters and Armi (2014). In particular, it is a hydrostatic approach that is valid up to arbitrary stretching in the horizontal direction and is applicable for any terrain shape provided the ratio h_m/σ_y is small, as is the case here. A practical question is, how useful is this hydraulic framework in understanding low Fr flows over long but finite ridges? In this setting, flow 'over' the crest establishes itself on a fast, inner time scale t_δ while flow 'around' the sides develops over a relatively longer time scale t_β.

When the ridge is infinite ($\beta = \infty$), an asymmetric crest-controlled flow state is attained quickly, by $t'_\delta = O(1)$ (Fig. 2.3). For a long but finite ridge ($\beta \gg 1$), the splitting time scale $t_\beta \gg t_\delta$ and so the development of flow over and around the ridge occur on disparate time scales. As a result, until intermediate times $O(1) < t'_\delta < O(10)$, the flow away from the edges is well approximated as a purely 2D infinite ridge overflow (Figs. 2.7 and 2.12).

By the time ($t'_\beta = O(1)$) horizontal splitting effects become significant, the overflow in the ridge interior is already asymmetric and has a parabolic velocity profile upstream of the crest. While its peak speed and thickness begin to decrease with the onset of flow splitting, across-crest asymmetry persists. On the slow splitting time scale $t_\beta \gg t_\delta$, the overflow retains the essential dynamical features of the infinite ridge overflow. This flow continues to be optimally controlled and the hydraulic view of the problem remains valid in the neighborhood of the crest. Our findings therefore demonstrate that across-crest asymmetry and hydraulic control, once established, persist even after the low-level flow has split around the sides of the ridge.

The isolating layers in Figs. 2.4 and 2.8 form as a result of mixing due to isopycnal overturning aloft, and in the infinite ridge case, also partly from repeated Kelvin-Helmholtz overturns at the top of the unstable downslope flow (Jagannathan et al., 2017). However, the hydraulic theory of Winters and Armi (2014) does not provide any insight about the formation of this homogenized isolating layer. Hydraulics also does not explicitly rely on internal mountain wave scales. Rather, the vertical scales of importance, h_m and δ, appear only indirectly through the transport equations (e.g. Eq. (2.13)). While limiting in some ways, the power of this approach is that it fully accounts for non-linearity, which is not possible in a wave treatment. Further, it produces quantitative predictions for the thickness and peak speed of the overflow which can be checked against the numerical solutions.

In our experiments, the far upstream flow speed V_∞ and stratification N are constant, i.e. these are like impulsively started laboratory towing experiments. This allows for a ready estimate of the modified late-time transport $V_\infty H_f$ within the overflow of thickness H_f. However in a geophysical context, these quantities are not usually known *a priori* and the exact, time varying upstream flow conditions must be determined using atmospheric soundings. As a more realistic example, one might consider flows with a spin-up time $T_{sp} \gg t_\delta$. The Froude number Fr and the inner length scales δ and $\sigma_{y_\delta} = O(Fr\,\sigma_y)$ will then be slowly evolving functions of time. However note that the inner time scale t_δ built from the instantaneous values of V_∞ and σ_{y_δ} will remain constant over the spin-up period as it is $O(\frac{\sigma_y}{Nh_m})$ and thus independent of V_∞ provided $Fr \ll 1$.

This suggests that when $T_{sp} \gg t_\delta$, the streamwise flow at any time $t < T_{sp}$ will be hydraulically controlled at the instantaneous Fr, which implies an overflowing layer of slowly expanding thickness and increasing peak speed. Thus while the quantitative details will differ, the essential dynamical character of the flow in the neighborhood of the crest will not change even when the background flow is slowly evolving.

A natural question then, is whether realistic low Fr flows across mountain ridges are characterized by the optimally controlled, parabolically sheared flow profiles predicted by Winters and Armi (2014) and seen in idealized towing experiments. Indeed, such flow features were noted by Armi and Mayr (2007) in their study of continuiously stratified flow over the alps. For example, the sounding at Sterzing (Fig. 16 of Armi and Mayr (2007)), taken well after the establishment of deep foehn conditions, reveals a parabolic velocity profile with peak speed of 20 ms^{-1} and thickness of about 3800 m. From the same figure, the blocking depth is seen to be about 500 m and the mean stratification $N \approx 10^{-2}\ \mathrm{s}^{-1}$. Based on the infinite ridge theory of Winters and Armi (2014), the prediction for the upstream overflow is $H = 8\delta \approx 4000$ m and $v_{max} = (3/2)NH/\pi \approx 19\ \mathrm{ms}^{-1}$, which agree well with the observed values.

The stratified hydraulic theory of Winters and Armi (2014), assuming optimal hydraulic control and across-crest asymmetry, predicts that the overflow at the blocking location is parabolic in shape. It further relates the thickness of the overflow to the blocking scale, $H = 8\delta$ and predicts its peak speed $v_{max} = (3/2)NH/\pi$ and transport $Q = NH^2/\pi$. In simple towing experiments, H is obtained by estimating the overflow transport and equating it to the optimal value NH^2/π. This is trivial for an infinite ridge (see Fig. 2.1). For long but finite ridges, a straighforward kinematic adjustment to the overflow transport after accounting for flow splitting, yields quantitative predictions for H and v_{max}. We will show in section 2.6.3 that by a similar, but algebraically more involved kinematic accounting for the overflow transport, the flow characteristics can be accurately predicted for low Fr flows across composite ridge configurations.

2.6.2 Downstream conditions and the cold pool

A significant point of difference between the finite and infinite ridge flow solutions is that, in the latter, the flow plunges much deeper into the lee before rebounding back to subcriticality via an internal hydraulic jump (Fig. 2.4c). Consequently the downslope flow is able to accelerate to peak speeds that are more than five times the far upstream flow speed (Fig. 2.5).

Comparing the isopycnals in Fig. 2.4 and Fig. 2.8, it is clear that the reason for this difference is the retention, in the case of the finite ridge, of the dense cold pool downstream. This acts as a strong stratification barrier to the plunging overflow, limiting both its speed and penetration depth. By contrast, in the infinite ridge case, the dense stratified fluid in the lee is swept away after a finite time, and replaced by lighter fluid that overflows the crest. Consequently, the descent of the downslope flow is unimpeded, and it is able to plunge deep in the lee.

This phenomenon is qualitatively similar to the observations of Mayr and Armi (2010) of a Foehn event in Owens valley located east of the Sierra Nevada. There they found that diurnal heating which has the effect of raising the potential temperature of the valley atmosphere leads to progressively deeper descent of the flow over the course of the day.

In our experiments, the properties of the cold pool are set by the prescribed downstream condition of uniform flow and stratification, and include low-level lee vortices (Fig. 2.10). While Drazin's (1961) solution fails to predict these lee vortices, Fig. 2.11 shows that his prediction of layer-wise potential flow is nonetheless valid upstream. As in the studies of Smolarkiewicz and Rotunno (1989), Schar and Durran (1997) and Ólafsson and Bougeault (1996), the present simulations were also carried out by imposing free slip boundary conditions. This suggests that vertical vorticity is produced by a purely inviscid baroclinic mechanism (Smolarkiewicz and Rotunno, 1989) at early times. The lee vortices intensify at later times perhaps because of potential vorticity anomalies that develop due to internal dissipation caused by upstream stagnation and flow splitting (Schar and Durran, 1997). The role of upstream blocking and flow splitting on orographic wake formation is further discussed by Epifanio and Rotunno (2005). In realistic atmospheric flows, the lee conditions may be affected by other factors such as surface heating or cooling and the presence or absence of secondary topographical features downstream (e.g. Winters, 2016).

2.6.3 The effect of an abrupt change in ridge elevation

We now seek to test the applicability of the stratified hydraulic approach in describing the overflow across a composite two-level ridge configuration shown in Fig. 2.17. This is an infinite ridge with a taller central section for which $\beta = 30$ and relative height difference, $\Delta h/h_1 = 1$. Mathematically, the ridge surface is given by Eq. (2.9), where σ_x^* is now the length of the narrow sloping section connecting the two ridge levels and is set to $\sigma_x/120 \ll \sigma_x$. The center of the taller section is treated as a symmetry boundary and the numerical model configuration and boundary conditions are identical to those in the finite ridge experiment. $Fr = V_\infty/Nh_1$ is set to 0.16, which implies $Fr = 0.08$ for flow approaching the taller section. The details of the numerical experiment are given in Table 2.2.

Far away from the taller section

The flow well away from the taller section is unaffected by its presence and must hence be identical to that in the infinite ridge case of section 2.5.1. The fluid beneath the blocking level cannot escape laterally and the low-level transport $V_\infty(h_1 - \delta)$ augments the overflow transport to match that of a parabolic, optimally controlled flow, as shown in the schematic Fig. 2.1.

Adjacent to the taller section

At cross-stream distances comparable to σ_x from the edge of the taller section, the overflow across the shorter section is additionally augmented by the splitting flow around the taller central section. Based on potential flow scaling Eq. (2.18) for flow around the finite ridge, we hypothesize

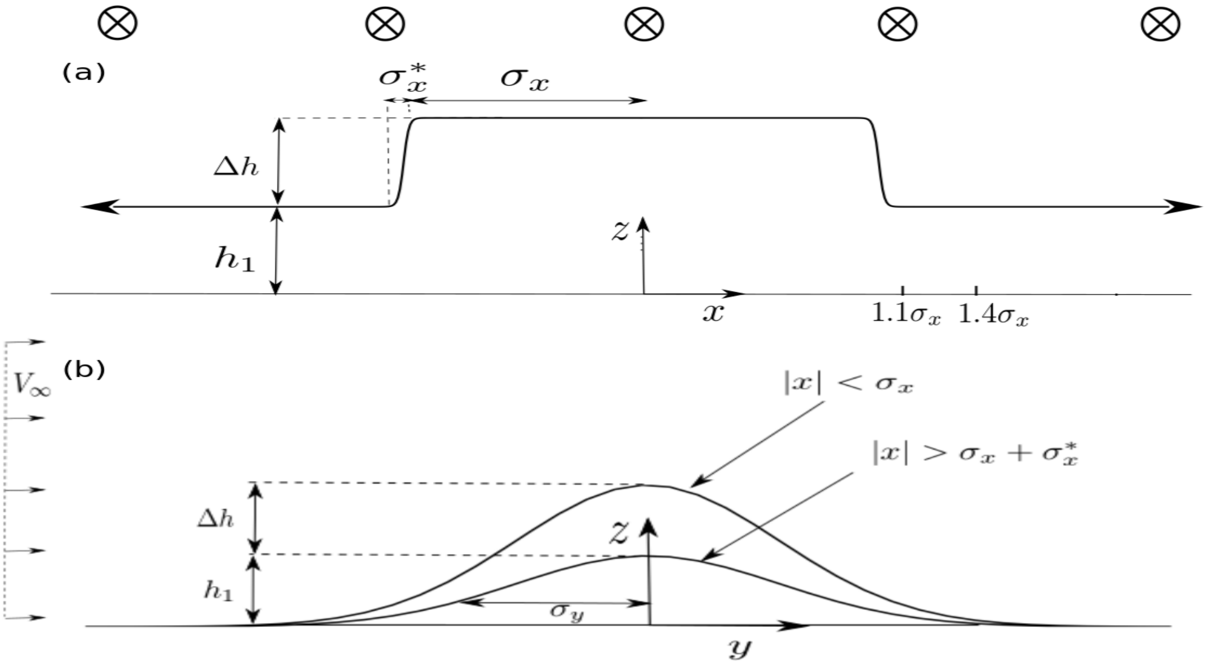

Figure 2.17: (a) Front view and (b) side view of an infinite two level ridge with half-width σ_y, a finite tall central section of height $h_1 + \Delta h$ and half-length σ_x with $\beta = \sigma_x/\sigma_y \gg 1$, straddled on either side by a shorter section of height h_1 and infinite length. This reduces to the single level ridge in Fig. 2.2 when $h_1 = 0$ and $\Delta h = h_m$. Figure not to scale.

that, at a vertical level $h_1 < z^* < h_1 + \Delta h - \delta$, where the ridge half-width is $\sigma_{y_{z^*}}$ this splitting flow scales with cross-stream distance as

$$v(x, y = -\sigma_{y_{z^*}}, z^*) \approx V_\infty \left(A + B\frac{\sigma_x^2}{x^2} \right), \qquad |x| > \sigma_x \tag{2.25}$$

The experimental domain is the same as in the finite ridge case of section 2.5.2; therefore $A = 1.1$ remains unchanged. However, due to the composite shape of the ridge, we anticipate that the shape factor B will, in general, be different from unity. The splitting flow speed and correspondingly, the overflow transport, decay with increasing cross-stream distance from the edge of the taller section. Assuming optimal crest control and an upstream overflow thickness $H(x) > h_1$, the volume conservation equation Eq. (2.13) for the infinite ridge is modified to

$$NH^2(x)/\pi = V_\infty(h_1 - \delta) + V_\infty \left(A + B\frac{\sigma_x^2}{x^2} \right)(\Delta h - \delta) + V_\infty(H + \delta - \Delta h), \tag{2.26}$$

with $\delta = H(x)/8$. The transport in the overflow is thus enhanced due to flow splitting. Note that as $x \to \infty$ and correspondingly, $A = 1$, Eq. (2.26) reduces to Eq. (2.13) for the infinite ridge case. We found that, for the case $\Delta h/h_1 = 1$ considered here, the value $B = 1.7$ for the shape coefficient produces the most accurate predictions, capturing both the quantitative properties of the overflow and its cross-stream decay away from the taller section.

Fig. 2.18a shows a late-time vertical profile of the upstream streamwise velocity at the cross-stream location $x = 1.4\sigma_x$ (indicated in Fig. 2.17a). The grey curve is the naive infinite ridge prediction based on Eq. (2.13), ignoring ridge geometry and lateral flow splitting, while the red curve is the corrected prediction obtained after modifying the transport calculation according to Eq. (2.26). While the naive prediction underestimates the peak speed and thickness of the overflow by close to 30%, these quantities are predicted almost exactly when flow splitting is

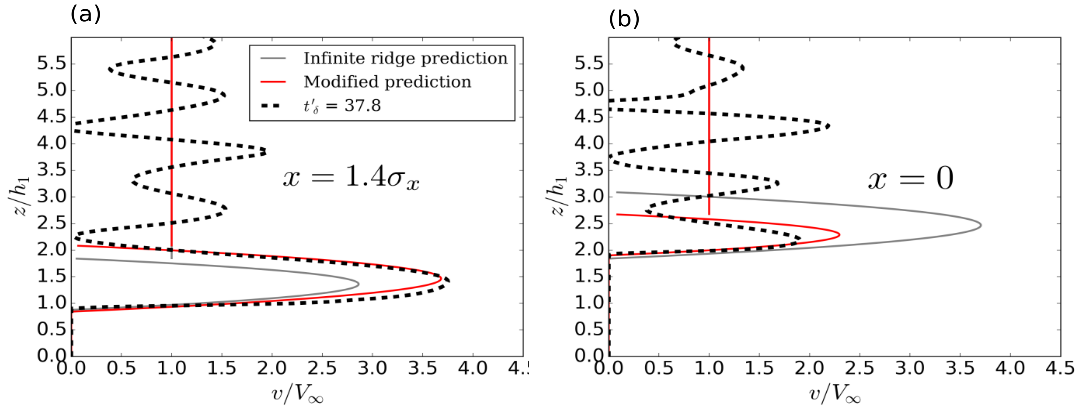

Figure 2.18: Computed and predicted vertical profiles of the streamwise velocity at the blocking location $y = -y_b$ of the two-level ridge at (a) the cross-stream location $x = 1.4\sigma_x$ (indicated in Fig. 2.17) and (b) the centerplane $x = 0$ of the taller section. Shown are the naive predictions (grey) obtained by ignoring flow splitting and solving Eq. (2.13) for an infinite ridge; and the modified predictions (red) obtained from solving Eq. (2.26) and Eq. (2.28) that correctly account for flow splitting.

accounted for correctly.

Over the taller section

Since the length of the connecting section is much shorter than the ridge length ($\sigma_x^* \ll \sigma_x$), we can, as in section 2.5.1, estimate the excess transport per unit length which is eventually absorbed into the splitting flow. This precisely equals the transport that is lost ahead of the taller section at late-times. From Eq. (2.25), on either side of the centerplane, this is given by

$$Q^* \approx \frac{1}{\sigma_x} \int_{\sigma_x}^{\infty} BV_\infty \frac{\sigma_x^2}{x^2} (\Delta h - \delta)\, \mathrm{d}x = BV_\infty (\Delta h - \delta). \tag{2.27}$$

At early times, the blocked transport ahead of the taller section, is $V_\infty(h_1 + \Delta h - \delta)$. Therefore, at later times, the portion of the blocked transport that is accounted for in the overflow aloft is given by $V_\infty(h_1 + \Delta h - \delta) - BV_\infty(\Delta h - \delta) = V_\infty[h_1 + \Delta h(1 - B) + \delta(B - 1)]$.

Assuming that this late-time overflow is optimally controlled with upstream thickness H, the volume conservation equation for flow over the taller central portion of the ridge is therefore

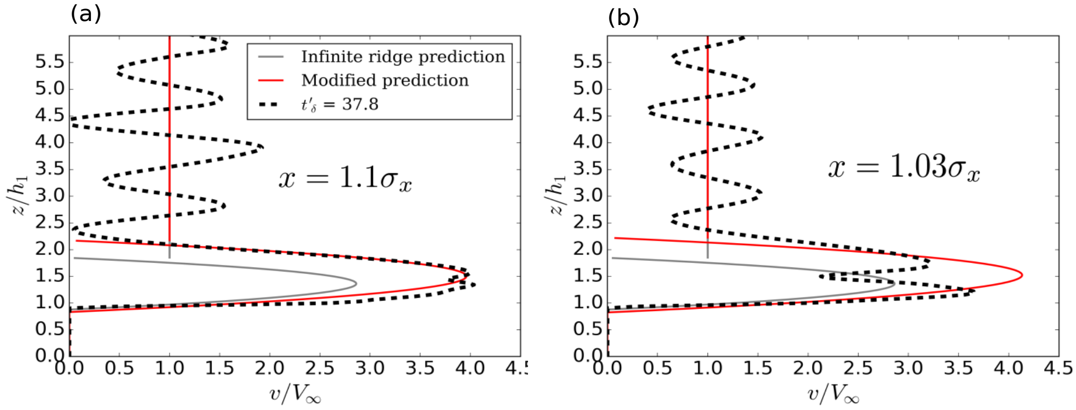

Figure 2.19: Same as Fig. 2.18 but at cross-stream locations$y_1 \leftrightarrow y_1^*$ nearer to the taller section: (a) $x = 1.1\sigma_x$ (indicated in Fig. 2.17a) and (b) $x = 1.03\sigma_x$.

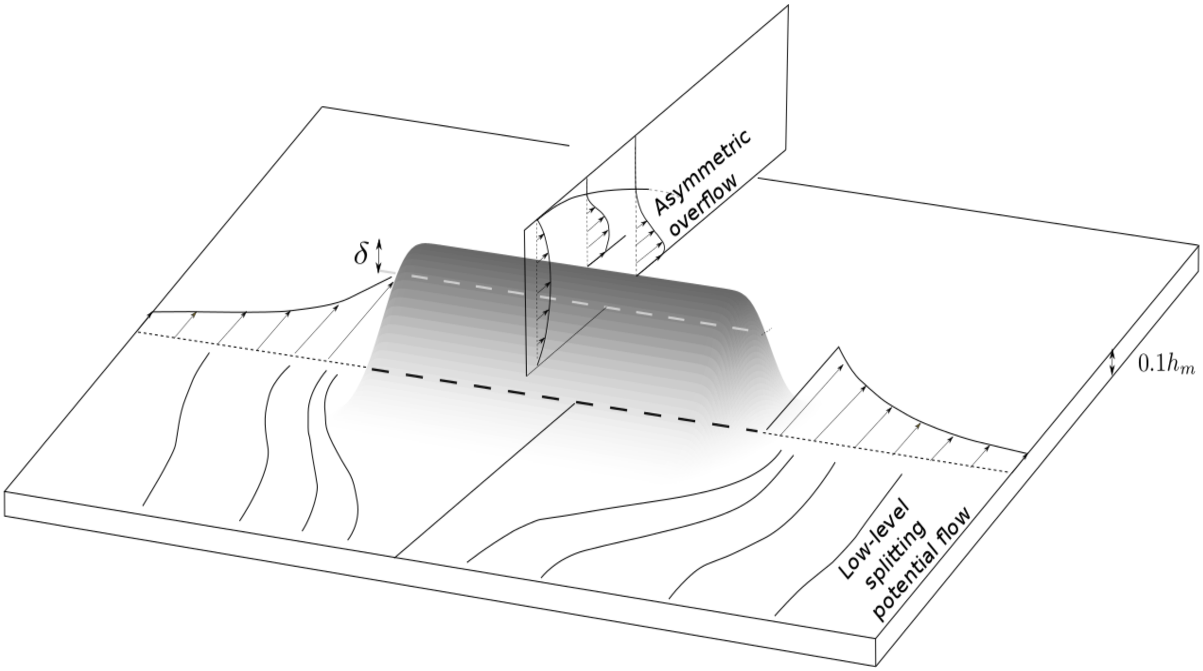

Figure 2.20: Schematic depicting the essential features of low Froude number over and around a long mountain ridge of height h_m. The flow has two distinct components: Above the blocking level is an overflow that is asymmetric and hydraulically controlled at the crest. Below the blocking scale δ from the crest is a layer-wise horizontal splitting flow that is potential-like upstream. The downstream penetration of the overflow is dependent on lee conditions and in our simple towing experiments, is limited due to the retention of a dense, cold pool.

$$NH^2/\pi = V_\infty H + V_\infty[h_1 + \Delta h(1-B) + \delta(B-1)], \tag{2.28}$$

with $\delta = H/8$ as before. Note that in the limit $\Delta h \to 0$, there is no splitting flow; the shape factor $B = 0$ and we recover the transport equation Eq. (2.13) for the infinite ridge.

In solving Eq. (2.28), we again use $B = 1.7$, the shape factor that produced the best fit for the overflow across the shorter section. Fig. 2.18b shows that, consistent with the Winters and Armi (2014) prediction, the computed upstream overflow in the centerplane $x = 0$ of the taller section has a parabolic profile starting at its blocking level. But whereas the naive prediction substantially overestimates its peak speed and thickness, the modified prediction that accounts for transport lost to the enhanced splitting flow, agrees well with the computed flow profile.

The transition region $\sigma_x < x \leq 1.1\sigma_x$

Across the lower portion of the ridge (Fig. 2.18a), the bottom of the overflow is located at an elevation $z \approx h_1 - \delta$ while over the taller section $|x| < \sigma_x$ it is at $z \approx h_1 + \Delta h - \delta$ (Fig. 2.18b). The flow near the abrupt change in ridge height must therefore bridge these two distinct overflows. The upstream velocity profile at the cross-stream location $x = 1.1\sigma_x$ is shown in Fig. 2.19a. The overflow exhibits two velocity peaks but these are only sightly separated and Eq. (2.26) predicts the bulk properties of the overflow well. Moving closer to the the taller section $x = 1.03\sigma_x$, Fig. 2.19b shows that although the total thickness of the overflow is predicted reasonably, its vertical structure is that of two jets with distinct peaks. Thus near the abrupt change in ridge elevation, the overflow is a composite of the short and tall section overflows. As a result, even after a kinematic adjustment to the overflow transport, the near-crest profile cannot be described in terms of a single parabolic overflow as in the infinite ridge theory of Winters and Armi (2014).

In summary, this two-level ridge example demonstrates that, in the flow regime where upstream influence and blocking are important, the steady overflow upstream of a dynamically tall, long ridge can be obtained by assuming optimal hydraulic control at the crest and coupling it to appropriate kinematic equations for the overflow transport. The details of the ridge geometry matter only to the extent that they modify the transport calculations. While the plunging depth of the overflow and its eventual separation in the lee are influenced by downstream conditions, a layer-wise solution of Bernoulli's equation, as in Winters and Armi (2014) furnishes a complete desciption of the asymmetric overflow in the neighborhood of the crest.

2.7 Limitations and extensions

2.7.1 Coriolis effects

As shown in the simulations, the hydraulic flow component develops on the short time scale t_δ while the low level splitting dynamics is established over a longer time scale $t_\beta \gg t_\delta$. Thus rotational effects play no role provided that $t_\beta \ll O(1/f)$, where f is the Coriolis frequency. In many mid-latitude atmospheric flows characterized by low Fr and large β, for example, with $N = 10^{-2}\ \mathrm{s}^{-1}$ and $V_\infty = 10\ \mathrm{ms}^{-1}$ and mountain dimensions $h_m = 4$ km, $\sigma_y = 20$ km and $\sigma_x = 200$ km (yielding $Fr = 0.25$ and $\beta = 10$), the corresponding t_δ can be shown to be well under an hour while t_β is about a quarter of an inertial period. Thus both the crest-controlled overflow and lateral splitting flow are established before Coriolis effects become significant.

The layer-wise upstream potential flow solution has also been realized in laboratory towing experiments (e.g. Brighton, 1978; Hunt and Snyder, 1980). Yet there are other geophysical applications where the flow splitting time scale may be comparable to or larger than an inertial period. In such situations, the evolution of the low-level splitting flow will be constrained by rotation and its horizontal scale is no longer set by the mountain half-length σ_x. Rather, as hypothesized by Pierrehumbert and Wyman (1985) and confirmed by Wells et al. (2005), geostrophic imbalance leads to the development of a mountain-parallel barrier jet trapped within a deformation radius Nh_m/f of the mountain. This disrupts the symmetry of the upstream splitting flow as well as the lee vortices, as can also be seen in the simulations of Wells et al. (2005).

However, as long as t_δ is small compared to an inertial period, asymmetry and crest control are likely to persist even after low-level flow splitting is established, regardless of whether the time scale controlling its evolution is t_β or $2\pi/f$.

2.7.2 Simple turbulence model

The focus of this study is on the dynamics of upstream blocking, hydraulic crest control and low-level flow splitting. These processes are laminar and therefore insensitive to the presence or absence of any turbulence closure model. Downstream of the crest, the supercritical flow is unstable to overturning shear instabilities. We resolve the formation of these instabilities but model the subsequent turbulence using a simple closure scheme that removes grid-scale variability. A higher resolution LES treatment of these processes in topographically controlled flows over an infinite ridge can be found in Winters (2016). A comparable treatment for the finite ridge case in which a hydraulically controlled overflow occurs in conjunction with lateral flow splitting is beyond our current computing capability.

2.7.3 The nature of the flow aloft

In both the infinite and finite ridge cases, we noted that the flow above the controlled overflowing layer is characterized by spatial oscillations with vertical wavelength approximately $2\pi V_\infty/N$ (Appendix B). While the hydraulic theory of Winters and Armi (2014) assumes that the controlled overflowing layer is decoupled from the overlying flow, it does not say anything about the possibility of wave excitation aloft as a response to the plunging overflow. Therefore the present analysis does not yield any insight about the ampitude of this wave-like flow nor its dynamical connection to the controlled overflow beneath.

One intrepretation of the layered structure aloft (e.g. Fig. 2.4c) is as follows. The flow in the layer immediately above the controlled overflow responds to the 'virtual topography' formed by the plunging overflow and is also asymmetric across the crest. The layers further aloft respond in a similar fashion. A similar response to virtual topography was noted by Armi and Mayr (2015) in their observations in the Sierras of hydraulically controlled flows with a descending temperature inversion at the top of the overflowing layer.

2.7.4 Extensions to other small Fr and large β flows

In the infinite ridge case, lowering Fr further while keeping h_m fixed shrinks the blocking scale δ and hence, also σ_{y_δ} and t_δ. This leads to quicker establishment of hydraulic control with a correspondingly thinner overflow. Increasing Fr has the exact opposite effect.

For a finite ridge, the (Fr, β) regime diagram (e.g. Smith, 1989; Lin, 2007) indicates that the flow behavior at low Fr and large β is uncertain. That is, the precise parameter space over which both flow-splitting and 'wave breaking' occur is unknown. The present study suggests another interpretation of this regime diagram. For a finite ridge, changing Fr and β essentially has the effect of making t_δ and t_β more or less disparate relative to one another. We have seen that blocking and hydraulic control are established on the short time scale t_δ. Assuming that 'wave breaking' triggers a transition to the controlled state (e.g. Baines, 1998), we may conjecture that flow-splitting and lee vortices are accompanied by a crest-controlled overflow when t_β is about an order of magnitude larger than t_δ. When these two time scales become comparable, the overflow will be subcritical and the flow then falls in the flow-splitting-only regime.

2.8 Concluding remarks

Across-crest asymmetry and hydraulic control are persistent features of low Fr flows past long ridges. On a short time scale, upstream blocking imparts a fundamentally non-linear and asymmetric character to the flow over the crest. This asymmetry persists even on the longer time scale over which the low-level splitting flow is established. The flow is therefore comprised of two distinct dynamical components as depicted in Fig. 2.20. The assumption of optimal crest control along with the recognition that the upstream splitting flow is potential-like, further allows for an accurate reformulation of the near-crest overflow.

This chapter has been submitted to the *Journal of the Atmospheric Sciences* as Jagannathan, A., Winters, K.B., Armi, L., “Stratified flows over and around long dynamically tall mountain ridges”. The dissertation author was the primary investigator and author of this paper.

Chapter 3

Stability of stratified downslope flows with an overlying stagnant isolating layer

3.1 Introduction and background

Features reminiscent of shear induced instability are often seen in the lee of topographically controlled stratified flows in the atmosphere and ocean. Despite a wealth of literature on the subject (e.g. Smith (1991), Scinocca and Peltier (1989), Farmer and Armi (1999), Armi and Mayr (2007) and references contained therein), the origin of these instabilities and their growth rate remain uncertain. Our aim here is to better reconcile field observations with results from numerical simulations exhibiting these features and linear stability theory. Figure 3.1 shows the idealized spatial structure of the flows under consideration. See also Winters and Armi (2014). A jet-like upstream profile with constant stratification, N_0 develops into a strong, thinning downslope flow beneath a layer of nearly stagnant, mixed fluid above. This downstream evolution is associated with intensifying shear at the interface between the flowing and stagnant layers. A feature to note is upstream influence characterized, in part, by stagnant "blocked" fluid below $z_d = z_b$. For a topography with crest height h_0, blocking is achieved by the upstream propagation of internal waves with vertical scale of about h_0. Given a far upstream velocity U_∞, mountain height h_0 and uniform upstream stratification N_0, our primary focus is in the flow regime

$$U_\infty/N_0h_0 \ll 1 \tag{3.1}$$

where upstream influence and blocking are important.

Observations of the 1972 Boulder storm by Lilly (1978) revealed quasi-periodic oscillations in the lee of the topography that were conjectured to be signatures of unstable Kelvin Helmholtz (K-H) waves. While Clark and Farley (1984) held these to be the result of a 3D shear-aligned convective instability, Scinocca and Peltier (1989) contested this view and instead advanced the idea that the dynamic instability of downslope windstorms was an intrinsically 2D phenomenon. In support of this assertion, they were able to replicate the quasi-periodic, 5-15 minute pulses revealed in the data using a 2D non-linear, non-hydrostatic anelastic numerical model. To investigate the effect of the upstream conditions on this phenomenon, they also simulated a downslope windstorm with an initially uniform upstream profile and found that the time evolution of the solution clearly exhibited upstream influence, characterized principally by blocking, as well as the pulsating features alluded to above. This led them to conclude that the occurrence of the pulsations does not depend sensitively on 3D effects nor on upstream conditions that precipitate the downslope windstorm. More recently, detailed measurements by Beluši'c et al. (2004) confirm the presence of 3-13 minute pulsations in the dynamically similar downslope Bora flow as well.

To test the hypothesis that these pulsations are the result of a dynamic instability of the mean flow, Peltier and Scinocca (1990) performed a spatial and temporal stability analysis of the downstream flow solutions of Scinocca and Peltier (1989) but found that the growth rates obtained were almost two orders of magnitude smaller than expected. They conjectured that the mean state extracted from the numerical simulation had already been modified by non-linear interactions with the instability modes. This motivated them to redo the stability analysis after introducing plausible but rather ad-hoc changes to the base state. Only then were they able to obtain growth rates that matched their 2D simulations. Here, we will examine the stability of profiles whose essential character is similar to the modified profiles of Peltier and Scinocca (1990), but determined by recently obtained solutions for steady, density-stratified topographically controlled flows by Winters and Armi (2014).

A similar (to our) approach was adopted by Smith (1985). However, he assumed a uniform upstream profile and invoked Long's (1955) equation, streamline bifurcation and local hydraulic theory to produce a downslope flow underlying a stagnant, uniform density layer aloft. Focusing only on the flowing layer, he notes that if the Miles-Howard condition (Miles (1961), Howard (1961)) of $Ri < 1/4$ is considered a sufficient criterion for onset of instabiity, then the local hydraulic theory prediction is validated by the Scinocca and Peltier (1989) numerical simulation of idealized severe downslope windstorms. To test if this agrees with results from linear stability theory, Smith (1991) solved the Taylor-Goldstein equation at a number of downstream locations for the base flow configurations of Smith (1985). We note however, that in his analysis, the background states were truncated at the upper edge of the flowing layer so as to exclude the stagnant uniform density isolating layer aloft. The stability analysis for these profiles, while yielding values for the wavelength that were consistent with Scinocca and Peltier (1989), severely underpredicted the onset and growth rate of the unstable K-H mode. Further, his choice of a uniform upstream profile excludes blocking and is not applicable in flow regimes where blocking and upstream influence are dynamically important. Thus linear stability analysis for flow profiles produced by both local hydraulic theory and extracted from numerical simulations yielded very small growth rates that were insensitive to upstream influence.

Recently, Winters and Armi (2014) accounted for the upstream influence of the topography in constructing optimally-controlled, jet-like solutions that thin and accelerate over the crest. These solutions are valid in the asymptotic limit of Eq. (3.1) and are characterized by a blocked region underlying the jet, a stagnant isolating layer of uniform density and a bifurcating streamline that separates the accelerating flow below from the dynamically uncoupled flow aloft (refer figure 3.1). They then show that, downstream of the blocking location, there emerges a region of sub-quarter Richardson number along the upper edge of the active layer, increasing in thickness downstream, and surmise that this suggests an environment conducive to the generation of shear instability.

One of our objectives here is to investigate the stability of the profiles produced in the optimally controlled flow of Winters and Armi (2014) at different downstream locations. These profiles have the character that the fluid velocity is zero in the overlying isolating layer, the thickness of which increases downstream of the crest. Formally, we will examine flow profiles characteristic of low Froude number settings.

3.2 Ambient profiles characteristic of controlled downslope flows

The family of profiles we study are those that arise naturally in the lee of the topography when the problem is formulated within a hydraulic framework as in Winters and Armi (2014). Figure 3.1 introduces our notation and illustrates the setting in which these flow configurations are encountered. At any downstream location $x > x_b$, the essential features of such flows are the following:

(i) The profile is jet-like, with an overlying stagnant region whose thickness, δ_i depends on the downstream position x.

(ii) Moving downstream, the velocity maximum descends from its initial vertical level.

(iii) The volumetric flow rate Q is conserved and equal to the value associated with the upstream jet.

(iv) As the flowing layer thins, the density difference remains the same. This implies a pro-

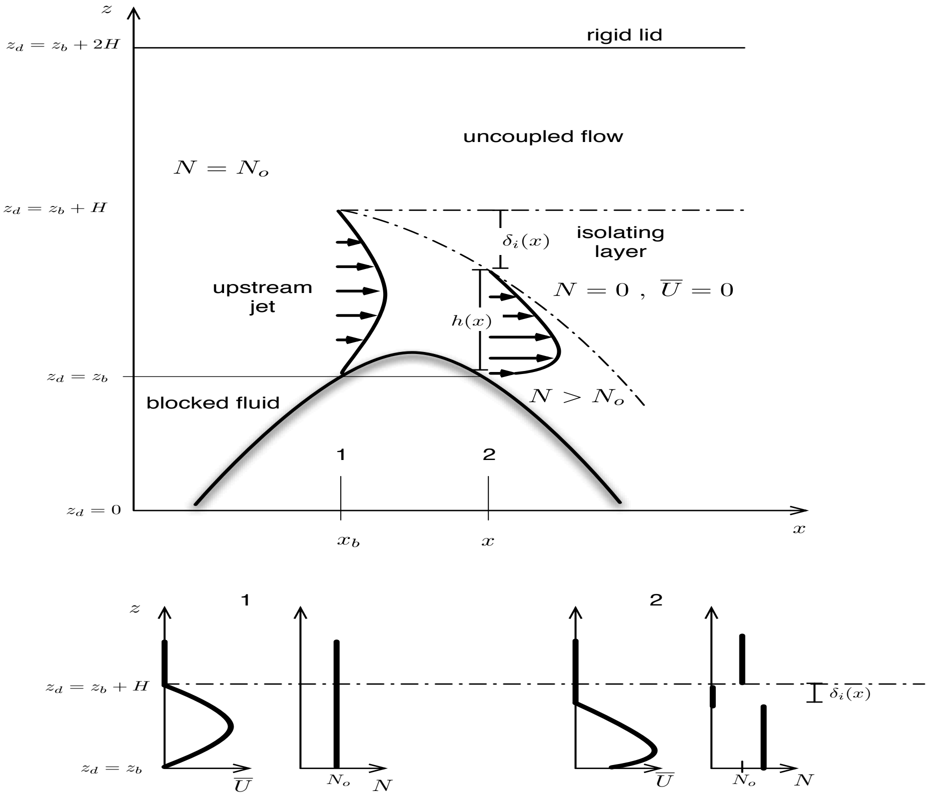

Figure 3.1: The downslope jet setting where flow configurations described above occur. The bottom panel displays the typical velocity and stratification profiles at the blocking point and an arbitrary point downstream of the crest, labelled 1 and 2 respectively.

portionately stronger stratification, which we take to be uniform for simplicity. This is a good approximation to the exact solution shown in figure 10 of Winters and Armi (2014)

The upstream profile is a parabolic jet with an overlying dynamically uncoupled layer, each of height H for simplicity. The upstream buoyancy frequency is constant and equal to N_0. As the flow develops, at each downstream location, it remains quasi-jet-like, but with a reduced thickness $h = H - \delta_i$, a stronger stratification and an isolating layer of height δ_i. The volumetric flow rate, $Q = (2/3)U_0H$ upstream remains conserved. To include the possibility of an accelerating bottom streamline, we represent the flow mathematically as a superposition of a parabolic jet with maximum U_{δ_i} and a linear component that vanishes at $z_b + h$. We define,

$$u_b = \beta U_{\delta_i} \tag{3.2}$$

where u_b is the velocity of the bottom streamline. The velocity and density profiles are then given by,

$$\bar{U}_d(z_d) = \begin{cases} 0, & z_b + h \leq z_d \leq z_b + 2H, \\ 4U_{\delta_i}\left[\frac{z_d}{h} - (\frac{z_d}{h})^2\right] + \frac{\beta U_{\delta_i}}{h}(h - z_d), & z_b \leq z_d \leq z_b + h. \end{cases} \qquad [m/s] \tag{3.3}$$

$$\bar{\rho}_d(z) = \begin{cases} \rho_0 + \Delta\rho - \frac{\Delta\rho}{2h} z_d, & z_b \leq z_d \leq z_b + h, \\ \rho_0 + \frac{\Delta\rho}{2}, & z_b + h \leq z_d \leq z_b + H, \\ \rho_0 + \frac{\Delta\rho}{2} - \frac{\Delta\rho}{2H}(z_d - H), & z_b + H \leq z_d \leq z_b + 2H, \end{cases} \qquad [kg/m^3] \tag{3.4}$$

where the overbar is used to denote the background flow field and the subscript '*d*' indicates dimensional quantities. Note that Q conservation and the bottom velocity parameter β jointly determine the parabolic maximum U_{δ_i} at any given downstream position as,

$$\frac{2}{3} U_0 H = U_{\delta_i} h \left(\frac{2}{3} + \frac{\beta}{2} \right). \tag{3.5}$$

Incorporating a perfectly homogeneous isolating layer introduces a discontinuity in the derivatives of the velocity and density at $h(x)$. To smooth this, we take these profiles as initial conditions for a 1D heat equation and allow diffusion for just enough time that the edge discontinuity is "sufficiently" ironed out for numerical discretization purposes. We have checked that our results are only weakly sensitive to small changes in the amount of smoothing. For example, the growth rate differed by only $\approx 1\%$ when the discontinuities were smoothed over a distance $h/50$ versus $h/200$. Similarly, the difference in growth rate was less than 2% when the ratio of the density and velocity diffusivity parameters was varied between 1 and 10.

For this problem, it is convenient to introduce another parameter,

$$\alpha = \frac{h}{H} = \frac{H - \delta_i}{H}, \tag{3.6}$$

that gives the height of the flowing layer as a fraction of the upstream thickness. The generalized stability analysis is then carried out in a two-parameter space of α and the bottom boundary parameter β, defined in Eq. (3.2). For the optimal flow solutions of Winters and Armi (2014), this reduces to a one-parameter space since there is a unique β that produces the best fit to the actual velocity profile for each α. We will examine this particular problem in more detail in section 3.6.2.

3.3 Mathematical formulation of the streamwise-local stability problems

The stability problem is developed using the primitive variable formulation and the normal mode decomposition. We begin with the inviscid Boussinesq equations of motion in non-dimensional form.

$$\frac{D\vec{u}}{Dt} + J\rho\hat{\mathbf{k}} = -\nabla p, \tag{3.7a}$$

$$\frac{D\rho}{Dt} = 0, \tag{3.7b}$$

$$\nabla \cdot \vec{u} = 0, \tag{3.7c}$$

where

$$J = g\frac{\Delta\rho}{\rho_0}\frac{h}{U_{max}^2}, \tag{3.8}$$

and in anticipation of jet-like profiles that terminate at the sill, z goes from 0 to $2H/h$, the reference values for the non-dimensionalization being h, $\Delta\rho$ and U_{max} - the height, density difference across the active flowing layer and its maximum velocity, given by

$$U_{max} = max(\bar{U}_d(z_d)). \tag{3.9}$$

Note that $h = H$ and $U_{max} = U_0$ at the blocking point. Moving downstream, the flowing layer thins, h decreases and U_{max} increases. Henceforth, all variables are non-dimensional unless otherwise stated.

We investigate the stability of a steady parallel, stratified shear flow of the form, $\vec{u} = \bar{U}(z)\hat{\mathbf{i}}$; $\rho = \bar{\rho}(z)$, with the pressure given by,

$$\frac{\partial \bar{p}}{\partial z} = -J\bar{\rho}(z), \tag{3.10}$$

to 2D normal mode perturbations of the form,

$$(u', w', \rho', p') = (\hat{u}(z), \hat{w}(z), \hat{\rho}(z), \hat{p}(z))e^{ik(x-ct)}. \tag{3.11}$$

Substituting Eqs. (3.10) and (3.11) in Eq. (3.7), linearizing and rearranging terms, we arrive at the following set of equations.

$$ik\bar{U}\hat{u}(z)+\hat{w}(z)\frac{\partial \bar{U}}{\partial z}+ik\hat{p}(z)=ikc\hat{u}(z), \tag{3.12a}$$

$$ik\bar{U}\hat{w}(z)+J\hat{\rho}(z)+\frac{\partial \hat{p}}{\partial z}=ikc\hat{w}(z), \tag{3.12b}$$

$$ik\bar{U}\hat{\rho}(z)+\hat{w}(z)\frac{\partial \bar{\rho}}{\partial z}=ikc\hat{\rho}(z), \tag{3.12c}$$

$$ik\hat{u}(z)+w_z=0. \tag{3.12d}$$

On a N_z grid, Eq. (3.12) can readily be recast as a generalized eigenvalue problem,

$$Av=cBv, \tag{3.13}$$

where A is a block diagonal matrix comprising 16 $N_z \times N_z$ blocks, B is a diagonal matrix and v is a column vector of the eigenfunctions. These are defined as follows,

$$A=\begin{pmatrix}
\begin{bmatrix} ik\bar{U}_1 & & 0 \\ & \ddots & \\ 0 & & ik\bar{U}_{N_z} \end{bmatrix} & \begin{bmatrix} ik\left(\frac{d\bar{U}}{dz}\right)_1 & & 0 \\ & \ddots & \\ 0 & & ik\left(\frac{d\bar{U}}{dz}\right)_{N_z} \end{bmatrix} & [0] & \begin{bmatrix} ik & & 0 \\ & \ddots & \\ 0 & & ik \end{bmatrix} \\
[0] & \begin{bmatrix} ik\bar{U}_1 & & 0 \\ & \ddots & \\ 0 & & ik\bar{U}_{N_z} \end{bmatrix} & \begin{bmatrix} J & & 0 \\ & \ddots & \\ 0 & & J \end{bmatrix} & [\mathrm{Dz}] \\
[0] & \begin{bmatrix} ik\left(\frac{d\bar{\rho}}{dz}\right)_1 & & 0 \\ & \ddots & \\ 0 & & ik\left(\frac{d\bar{\rho}}{dz}\right)_{N_z} \end{bmatrix} & \begin{bmatrix} ik\bar{U}_1 & & 0 \\ & \ddots & \\ 0 & & ik\bar{U}_{N_z} \end{bmatrix} & [0] \\
\begin{bmatrix} ik & & 0 \\ & \ddots & \\ 0 & & ik \end{bmatrix} & [\mathrm{Dz}] & [0] & [0]
\end{pmatrix}_{4N_z\times 4N_z}, \tag{3.14}$$

$$B = \begin{pmatrix} \begin{bmatrix} ik & & 0 \\ & \ddots & \\ 0 & & ik \end{bmatrix} & [0] & [0] & [0] \\ [0] & \begin{bmatrix} ik & & 0 \\ & \ddots & \\ 0 & & ik \end{bmatrix} & [0] & [0] \\ [0] & [0] & \begin{bmatrix} ik & & 0 \\ & \ddots & \\ 0 & & ik \end{bmatrix} & [0] \\ [0] & [0] & [0] & [0] \end{pmatrix}_{4N_z \times 4N_z}, \tag{3.15}$$

$$v = \begin{pmatrix} \hat{u}(z) \\ \hat{w}(z) \\ \hat{\rho}(z) \\ \hat{p}(z) \end{pmatrix}_{4N_z \times 1}, \tag{3.16}$$

where Dz is the differentiation matrix and the large zeros denote zero matrices. Given $\bar{U}(z)$, $\bar{\rho}(z)$ and a specified wave number, k, we then solve a $4N_z \times 4N_z$ problem for the eigenvalue c and eigenfunctions $\hat{u}(z), \hat{w}(z), \hat{\rho}(z)$ and $\hat{p}(z)$. From these, we may deduce the temporal growth rate

$$\omega_g^T = kc_i, \tag{3.17}$$

where the subscript i denotes imaginary part.

3.4 Numerical implementation

A Chebyshev pseudo-spectral collocation method (Appendix C) is used to compute derivatives and construct the coefficient matrices. Boundary conditions of no normal flow $\hat{w}(z) = 0$ are imposed on the upper and lower boundaries. Note that the upper boundary is well above the location where the flowing layer meets the isolating layer and so the inflection point in $\bar{U}(z)$ at that location can affect the solutions.

Due to the singularity of the coefficient matrices, the generalized eigenvalue solver delivers a number of spurious eigenvalues that manifest as infinite or very large values. This is not surprising if one notes that the eigenvalue problem, Eq. (3.13) can alternatively be formulated as a quadratic eigenvalue problem of size $N_z \times N_z$ (Winters and Riley (1992)) which in turn can be shown to possess precisely $2N_z$ eigenvalues (see e.g. Tisseur and Meerbergen (2001)). Thus only $2N_z$ of the $4N_z$ eigenvalues obtained from solving Eq. (3.13) are physically relevant. Empirically we found that the number of spurious eigenvalues is in fact $2N_z + 2$. The two additional modes presumably appear as a consequence of the homogeneous boundary conditions on $\hat{w}(z)$. This indeed seems to be the case because, when the redundant boundary condition, $\hat{\rho}(z) = 0$ was also imposed in addition to $\hat{w}(z) = 0$ at the boundaries, the solution remained unchanged except that we now counted the number of spurious eigenvalues to be $2N_z + 4$ rather than $2N_z + 2$.

Further, because of the intrinsic singularity of the Taylor-Goldstein equation, a number of eigenvalues also belong to the continuous spectrum of singular neutral modes and are not important in a the normal mode analysis of the stability problem. Some of these may also be contaminated with small non zero imaginary parts, but are filtered using the kinetic energy criterion described in Moum et al. (2003). $N_z = 256$ is found to deliver convergent values for the growth rate and phase speed of the unstable mode.

3.5 Results for generalized ambient flow profiles characteristic of downslope flow

In this section, we display the results of the stability analysis for flows whose upstream configuration is given by the optimal solution of Winters and Armi (2014), but whose downstream evolution is determined by flow rate conservation and the two-parameter space (α, β). Studying these profiles may be helpful, for example, in understanding the stability of flows that arise in downslope flow settings where the idealized Winters and Armi (2014) assumptions on the flow regime and hydrostaticity are relaxed and α and β have a different functional relation.

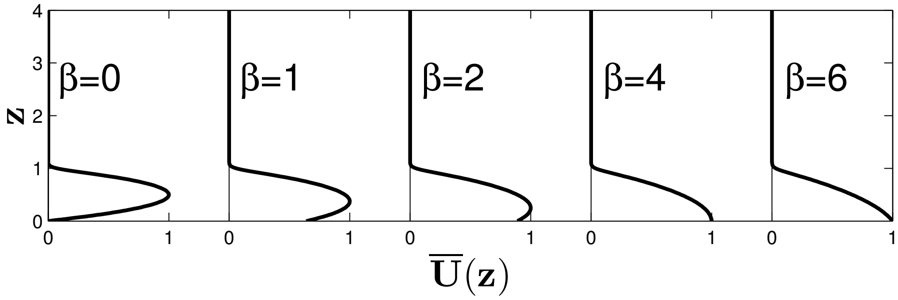

Figure 3.2: The background velocity for the illustrative case of $\alpha = 0.5$. As β increases, the flow changes character from a pure parabolic jet towards a linearly sheared profile.

To begin, we consider a family of stratified flows with $\alpha = 0.5$. This corresponds to a flowing layer downstream of the crest with height $h = H/2$, i.e. after the lower branch of the bifurcating streamline has descended from its initial position by a distance $H/2$. Figure 3.2 shows several such profiles in non-dimensional form. These differ in their β values, which corresponds to differences in speed at the lower free-slip boundary. Figure 3.3a and 3.3b display the corresponding vorticity gradient and inverse Richardson number curves for these flows. We shall return to the significance of these particular vorticity and Richardson number profiles in section 3.6.1.

Note again that the values α, β and Q conservation completely determine the profiles and define the stability problem. The dimensional expressions for velocity maximum, stratification and $Ri(z_d)$ are derived below. Eq. (3.5) gives,

$$U_{\delta_i} = \frac{\frac{2}{3}U_0}{\alpha\left(\frac{2}{3}+\frac{\beta}{2}\right)}. \tag{3.18}$$

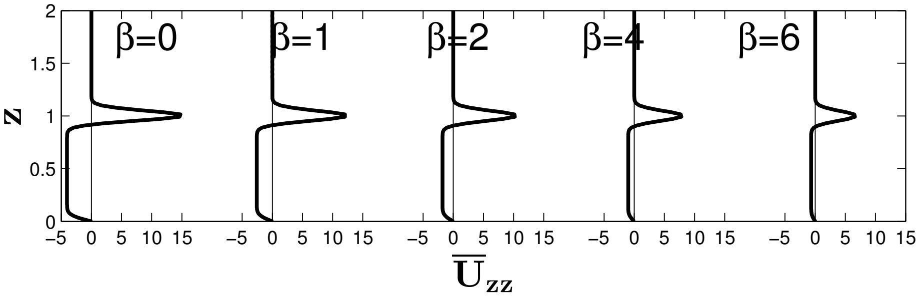

(a)

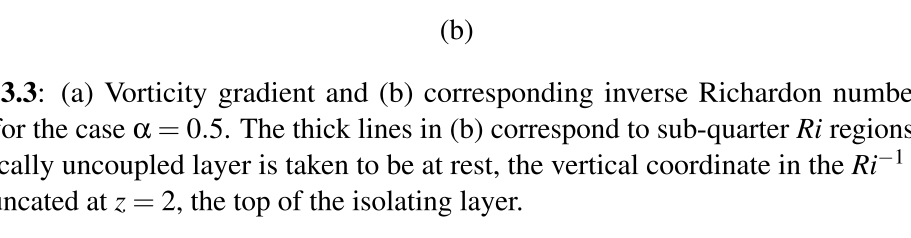

(b)

Figure 3.3: (a) Vorticity gradient and (b) corresponding inverse Richardon number (Ri^{-1}) profile for the case $\alpha = 0.5$. The thick lines in (b) correspond to sub-quarter Ri regions. As the dynamically uncoupled layer is taken to be at rest, the vertical coordinate in the Ri^{-1} plot has been truncated at $z = 2$, the top of the isolating layer.

Similarly, from Eq. (3.4), the stratification for a given value of α is directly given by

$$N_{\delta_i} = N_0/\sqrt{\alpha}. \tag{3.19}$$

Now, the optimal solution of Winters and Armi (2014) is characterized by an upstream parabolic jet with,

$$U_0 = (3/2)N_0 H/\pi. \tag{3.20}$$

Using Eqs. (3.3),(3.18), (3.19) and (3.20), the Richardson number in the flowing layer can be written as,

$$Ri = \frac{N_{\delta_i}^2}{\left(d\bar{U}_d/dz_d\right)^2} = \frac{\pi^2\alpha\left(\frac{2}{3}+\frac{\beta}{2}\right)^2}{\left(\frac{4}{\alpha}-\frac{8z_d}{\alpha^2 H}-\frac{\beta}{\alpha}\right)^2}. \tag{3.21}$$

The minimum value of Eq. (3.21) always occurs at $z_d = \alpha H$, or $z = 1$ i.e. at the upper edge of the flowing layer and is given by,

$$Ri_{min} = \pi^2\alpha^3\frac{\left(\frac{2}{3}+\frac{\beta}{2}\right)^2}{(4+\beta)^2}. \tag{3.22}$$

For each profile, we specify the wave number k and solve the eigenvalue problem Eq. (3.13). We then sweep over a specified range of $0 \leq k \leq 10$ to capture an order 1 aspect ratio K-H mode and extract the mode with the largest growth rate and the associated wave number k_{max} and phase speed c_r. Table 3.1 summarizes the results for particular values of α and β . We interpret the results in the context of hydraulically controlled stratified flow over topography, as in figure 3.1.

As the active layer crests the topography, the isolating layer increases in thickness, eventually triggering instability at a certain critical α_c. We did not obtain any unstable modes for $\alpha \geq 0.8$ suggesting that $0.7 \leq \alpha_c \leq 0.8$. The e-folding time t_e which is the time it takes for the perturbation to increase by a factor of e is a useful characterization for comparison purposes. The $O(1)$ e-folding times for the unstable modes (table 3.1) are consistent with the non-linear simulations of Scinocca and Peltier (1989).

The dimensional values of the phase speed and wavelength of the most unstable mode are also presented in the last two columns of table 3.1 for the value of H corresponding to the numerical study of Smith (1991). He reported the first significant unstable mode encountered downstream to have period and wavelength 273 sec and 2855 m respectively which is also consistent with the ranges predicted by Scinocca and Peltier (1989). While our values for these parameters are of the same order, the major difference is in the onset and growth rates of the unstable modes which we found to be over an order of magnitude larger.

For the upstream flow, $\alpha = 1$ and $\beta = 0$, which yields $Ri_{min} = \pi^2/36 > 1/4$, which is stable by the Miles-Howard theorem. Note that $Ri_{min} \sim \alpha^3$, so moving downstream, the large shear at the interface of the jet and the stagnant layer dominates the stabilizing effect of the stratification and increasing β. This explains the persistence of unstable modes at low α and relatively large β seen in table 3.1.

Figs. 3.4-3.6 display the normalized eigenfunctions for $|\hat{u}(z)|$ and $|\hat{w}(z)|$. Their wavelengths (table 3.1) and shape identify them as unit-aspect-ratio overturning shear instabilities that nucleate at the upper edge of the flowing layer, where there is an abrupt jump in shear, as shown in figure 3.3a.

3.6 Discussion

Recall that Rayleigh's theorem gives the presence of an inflection point as a necessary condition for instability in a homogeneous shear flow. The flows examined above are essentially sheared flows endowed with an inflection point, but in a stably stratified environment. Investigating the stability of the corresponding homogeneous shear profile can help clarify the nature of the

Table 3.1: Characteristics of the unstable mode in the two-parameter space of β and α. The last two columns are the dimensional values of the period (T_p) and wavelength (λ) of the unstable mode for the case $H \approx 1865$ as in the numerical experiments of Smith (1991).

	β	k_{max}	ω_g^T	$t_e(=1/\omega_g^T)$	$T_p(s)$	$\lambda(m)$
$\alpha = 1$	Stable for all $\beta \geq 0$					
$\alpha = 0.9$						
$\alpha = 0.8$						
$\alpha = 0.7$						
	0	3.6	0.2059	4.86	488	2279
	1	-	-	-		
	2	-	-	-		
	4	-	-	-		
	6	-	-	-		
$\alpha = 0.6$						
	0	3.6	0.3389	2.95	346	1953
	1	2.8	0.1434	6.97	522	2511
	2	-	-	-		
	4	-	-	-		
	6	-	-	-		
$\alpha = 0.5$						
	0	3.2	0.4271	2.34	259	1831
	1	2.4	0.2801	3.57	389	2441
	2	2.0	0.1581	6.32	459	2930
	4	-	-	-		
	6	-	-	-		
$\alpha = 0.4$						
	0	3.2	0.4878	2.05	163	1465
	1	2.4	0.3676	2.72	239	1953
	2	2.0	0.2604	3.84	280	2344
	4	1.6	0.1287	7.77	322	2930
	6	1.6	0.0659	15.17	322	2930

1. k_{max} is the wave number of maximum temporal growth rate $\omega_g^T = k_{max} c_i$, where $c_i = \mathrm{Im}(c)$.
2. t_e is the e-folding time for the fastest growing mode, scaled by h/U_0
3. '-' indicates no unstable modes found.

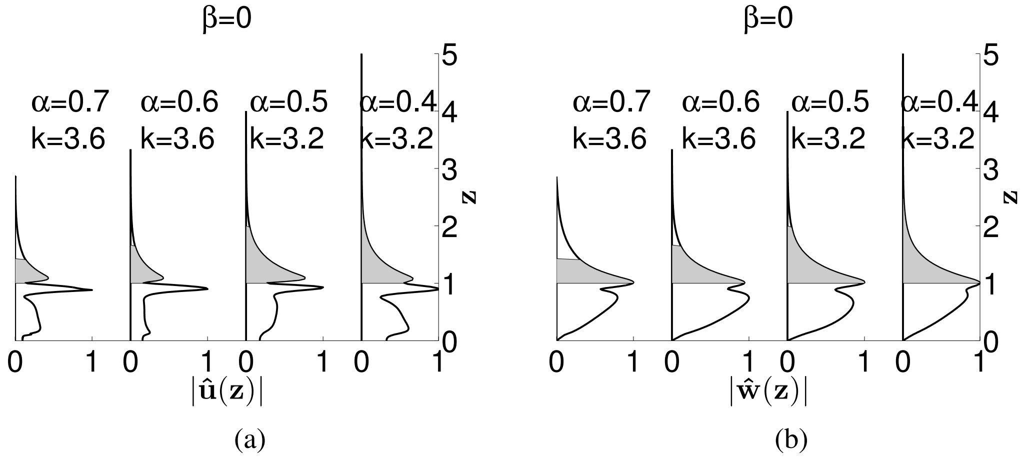

Figure 3.4: Normalized eigenfunctions (a)$|\hat{u}(z)|$ and (b)$|\hat{w}(z)|$ for $\beta = 0$. This represents the case where the bottom streamline is stationary, ie downslope flow evolves as a pure parabolic jet. $\alpha = 0.7, 0.6, 0.5$ and 0.4 were all found to possess a growing mode. Note that the lengths are non-dimensionalized using the height of the flowing layer at each location, so the isolating layer (shaded grey) lies between 1 and $1/\alpha$. Between $1/\alpha$ and $2/\alpha$, the background flow is dynamically uncoupled and the eigenfunctions decay exponentially. The sharp behavior of $|\hat{u}(z)|$ at $z = 1$ is typical of a K-H mode at a shear interface.

instability in the stratified scenario. If shear were the driving mechanism of the instability, then we would expect stratification to have a stabilizing effect, modifying the unstable shear mode and reducing its growth rate.

Indeed we found that, for every flow configuration for which an unstable mode was present, the growth rate for the same shear profile, but without a stable stratification was larger. This identifies the unstable modes of table 3.1 as stratified analogues of inflectional Rayleigh modes, which, following the convention of Carpenter et al. (2010), we refer to as Kelvin-Helmholtz modes. We further note that in the absence of stratification, the piecewise linear limit, corresponding to $\beta \to \infty$ is stable for all values of α. Our numerical results suggest this also holds for piecewise continuous, linear stratifications such as the ones under consideration here.

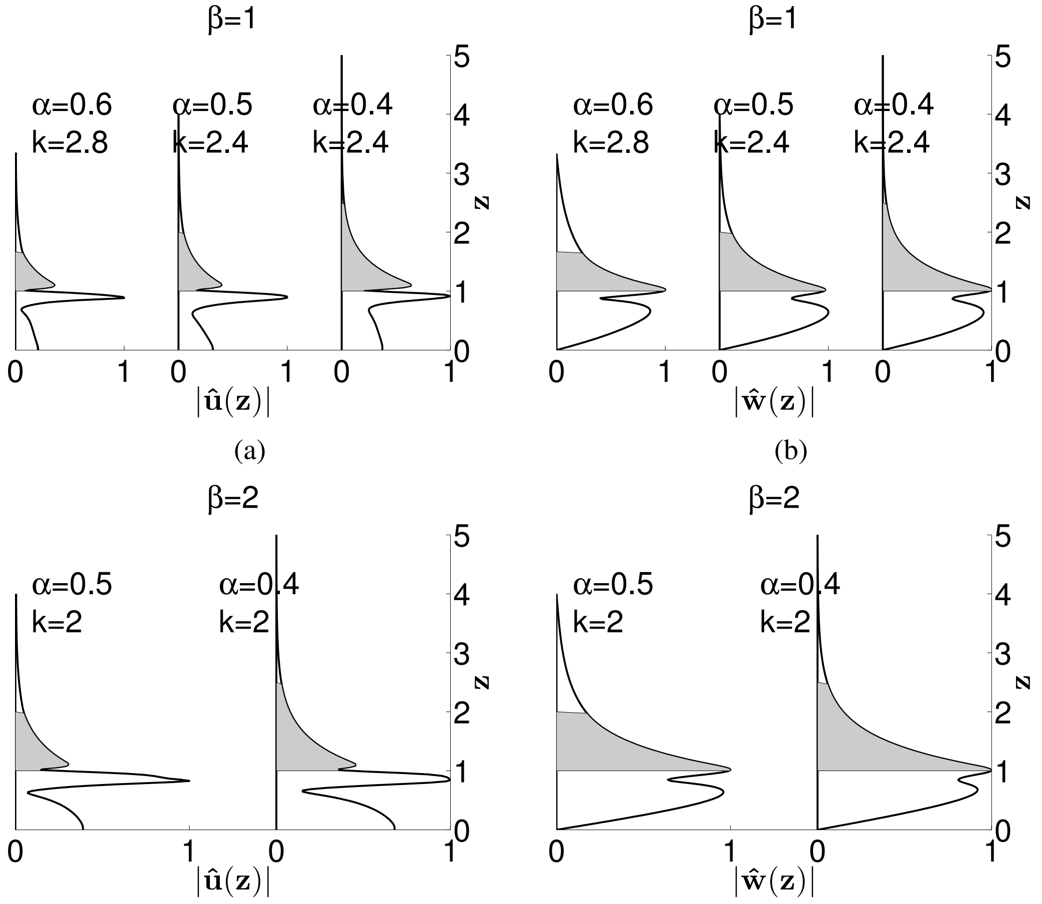

(a) (b)

(c) (d)

Figure 3.5: Normalized eigenfunctions (a),(c) $|\hat{u}(z)|$ and (b),(d) $|\hat{w}(z)|$ for $\beta = 1, 2$. When the bottom streamline is not stationary, as for example in the case of a free-slip boundary. In this configuration, the velocity maximum for the base flow shifts downwards compared to the pure parabolic jet (see figure 3.2). For $\beta = 1$, $\alpha = 0.6, 0.5$ and 0.4 were found to be unstable. When $\beta = 2$, the base profile is qualitatively similar to the case $\beta = 1$, but the larger bottom velocity appears to stabilize the flow for $\alpha \geq 0.6$.

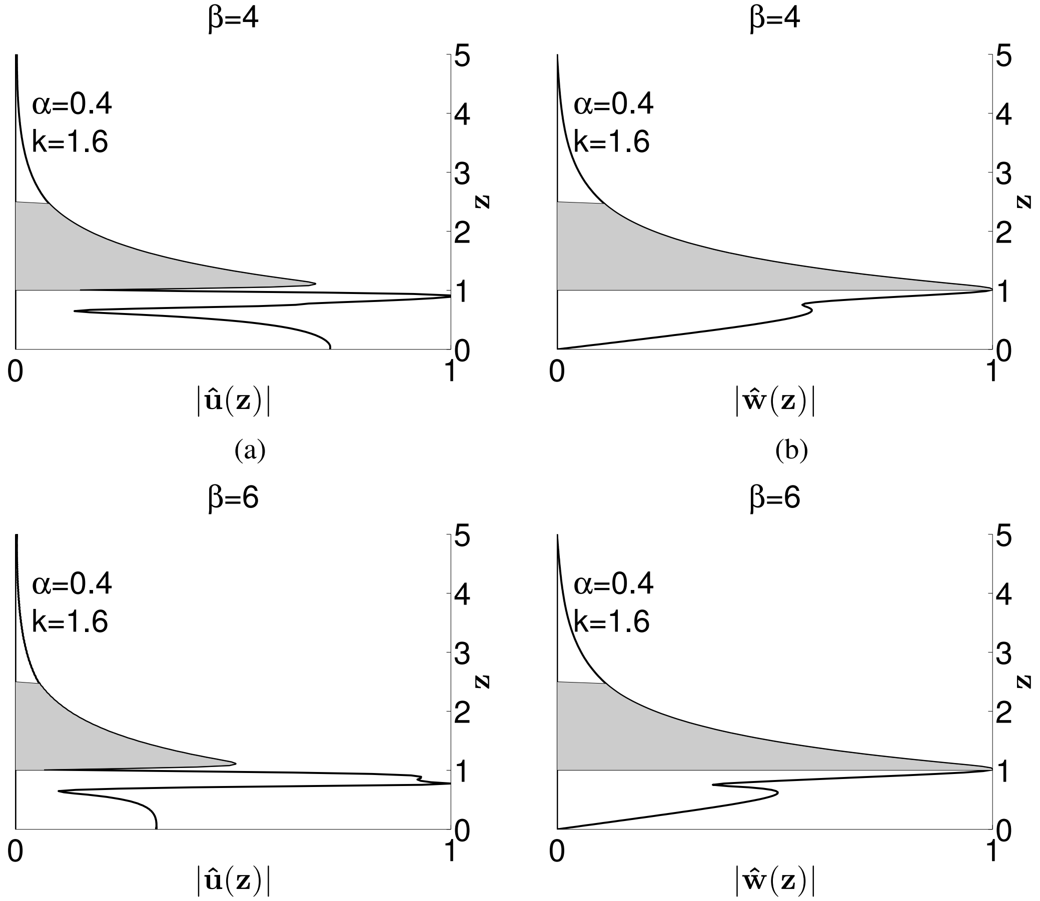

(a) (b)

(c) (d)

Figure 3.6: Normalized eigenfunctions (a),(c) $|\hat{u}(z)|$ and (b),(d) $|\hat{w}(z)|$ for $\beta = 4, 6$. This represents the case where the linear component begins to dominate the profile. $\beta = 4$ is the critical value where the velocity maximum coincides with the bottom streamline. For this configuration, only $\alpha = 0.4$ possesses sufficient shear to allow instability. At $\beta = 6$, the linear component clearly dominates the base profile (figure 3.2), but instability persists for $\alpha = 0.4$.

3.6.1 Physical interpretation of instability

The wave-interaction theory (see, e.g. Carpenter et al. (2011)) offers qualitative insight into the destabilizing mechanism at play. The key idea of the theory is that instability is possible whenever the flow configuration supports two or more waves whose direction of intrinsic propagation, relative to the local fluid velocity, are of opposite signs. Additionally, for a large class of stratified flows, Baines and Mitsudera (1994) showed that an arbitrarily small region with $Ri < 1/4$, flanked on either side by regions where $Ri > 1/4$ is a sufficient condition for instability. Such a configuration effectively splits the flow into stable upper and lower waveguides, with no vertical wave propagation being possible in the central sub-quarter Richardson number region, a result effectively proved by Bell Jr (1974). Two free modes in these separated waveguides can then interact to cause mutual changes in phase speed, inducing them to become stationary relative to one other, leading to mutual excitation and growth. This optimal “phase locked” state is maintained over a range of wave-numbers through adjustments to the phase difference. On the other hand, if $Ri > 1/4$ everywhere, internal wave modes are able to propagate vertically, eventually getting absorbed back into the mean flow at a critical layer in the central region; and the flow remains stable.

The $\bar{U}_{zz}$ profiles in figure 3.3a are seen to exhibit a large peak at $z = 1$ corresponding to the nearly discontinuous vorticity interface at the lower branch of the bifurcating streamline of figure 3.1. Below this, their values are constant, but reduced in strength and opposite in sign relative to the interface above. Thus the intrinsic direction of propagation of vorticity waves in each of these regions is opposite, satisfying one of the necessary conditions of the wave-interaction theory.

To see in more detail how these particular vorticity profiles can lead to instability, consider again the corresponding unstratified flow. Note that, unlike the prototypical examples of piecewise linear and continuous vorticity distributions for which the wave-interaction mechanism has been invoked to understand shear instability ((e.g. Carpenter et al. (2011)), in these flows, the vorticity profiles exhibit only one (and not two) distinct extrema. Thus the view of the instability as an interaction between two interfacial (or smeared) vorticity waves breaks down; and it is necessary to include the continuous spectrum in the analysis. When the flow is quasi-jet-like, with $\beta \sim O(1)$, the unstable inflectional mode may be regarded as arising due to the interaction between the interfacial, rightward propagating vorticity wave riding on the shear interface at $z = 1$ and a wave belonging to the continuous spectrum supported in the region of constant vorticity between $z = 0$ and $z = 1$. The abrupt change in the $\hat{u}(z)$ eigenfunction near $z = 1$ in figures 3.4-3.6 is typical of a vorticity wave propagating at a shear jump and further bolsters this view of the instability mechanism. When a stable stratification is added, the vorticity modes are modified by the buoyancy, leading to weakened interaction and consequently, reduced growth rates.

Inspection of figure 3.3b shows that the Baines and Mitsudera (1994) condition on the Richardson number profiles is also met for these flows. The thin lines denote separate stable wave-guides where $Ri > 1/4$. These are separated by a region (thick line) where $Ri < 1/4$ and internal wave propagation cannot occur. Approximating $z = 1$ as a discontinuous shear interface, the speed of the rightward propagating vorticity wave here is given by, to first order

$$c_1 \approx \frac{\bar{U}_z|_{z=1^-}}{2k} \tag{3.23}$$

The flow configurations in the stable lower waveguide yield a discrete spectrum of internal wave modes modified by the shear in addition to a continuous spectrum whose eigenvalues lie in the range of $\bar{U}$. In the absence of stratification, the same shear profiles support only a continuous spectrum whose properties however, differ from those of the continuous spectrum for the corresponding stratified flow. Further, Howard's (1961) semicircle theorem constrains the real phase speed of an unstable mode for this flow to lie within the range of fluid velocity. So, given the lack of a clear shear or density interface in the lower wave-guide, it seems likely that for both the stratified and unstratified flow, it is the interaction between the interfacial vorticity wave and a wave in the continuous spectrum that gives rise to instability.

To test this hypothesis, we added a small amount of viscosity and diffusivity and solved the 6th order Taylor-Goldstein equation for the flow configurations in the lower wave guide. Free slip and an exponential decay condition for $\hat{w}(z)$ at the upper boundary filter the unstable Tollmien Schlichting waves from the computation. The wave modes thus obtained are essentially similar to what we would find for the inviscid flow- vorticity waves modified by buoyancy and vice-versa- with the difference being that the singularity of the second order Taylor-Goldstein equation is avoided and consequently, the continuous spectrum collapses onto a discrete set of decaying modes. For the case $\alpha = 0.5, \beta = 2$, we found that at $k = 5$, there are two modes with speeds ≈ 0.26 which is roughly the same value that was found on applying Eq. 3.23 and which also matched the real part of the eigenvalue of the unstable mode that was found by solving the Taylor Goldstein equation for the complete profile in figure 3.2. Thus we have all the necessary elements for the wave-interaction theory to be invoked; instability persists over a range of wave numbers by mutual interaction leading to phase and amplitude locking.

For larger values of β, the shear gradient below $z = 1$ is too weak to induce a mutual growth with the vorticity wave riding aloft at $z = 1$. In the piecewise linear limit $\beta \to \infty$, there is exactly one vorticity interface at $z = 1$; no fundamental unstable shear mode is present, and thus the addition of a linear stratification apparently has no effect on the stability of the flow. As a corollary, we surmise that no unstable wave interactions are possible in a piecewise linear, stably stratified environment where there are no density jumps and where the shear is uniform on either side of a single vorticity interface.

In light of this explanation, we speculate that the reason for late onset of instability and small growth rates of Smith (1991) result from truncating the base flow at the upper edge of the active layer. This excludes a vorticity wave at the upper boundary and consequently, no destabilizing wave interactions are possible in the flow. We note however that, despite the lack of an inflection point in the profiles, the exponential decay implied by their upper boundary condition does not completely exclude the possibility of instability and indeed, the weak growth

Table 3.2: Characteristics of the unstable mode for the flow profiles representative of the exact solutions of Winters and Armi (2014). Refer to table 3.1 for more details on notation.

α	β	k_{max}	ω_g^T	t_e	$L_e(=c_g/\omega_g^T)$	$T_p(secs)$	$\lambda(ms)$
0.66	0.89	4.0	0.0743	13.46	4.05	490	1933
0.64	1.00	3.6	0.0807	12.39	3.79	496	2083
0.62	1.09	2.8	0.0928	10.78	3.33	571	2595
0.6	1.19	2.8	0.1093	9.15	2.74	532	2520
0.5	1.94	2.0	0.1643	6.10	1.68	459	2930
0.4	4.00	1.6	0.1287	7.77	1.60	322	2930

1. L_e is the e-folding length for the fastest growing spatial mode, scaled by h. See section 3.6.2 for more details.
2. c_g is the group velocity of the mode given by $c_g = \partial\omega_r/\partial k$ where $\omega_r = \mathrm{Re}(kc)$.

rates predicted might well be a consequence of this. In contrast, we have included both the isolating layer and the dynamically uncoupled flow in our analysis. This, besides imposing precise no-normal flow conditions at both boundaries, also furnishes an inflection point to the velocity profile - a necessary condition for stability of unstratified shear flow-, as well as a region of weak stratification close to the inflection point (giving $Ri < 1/4$), which may trigger an unstable shear mode via the wave interaction mechanism described above.

3.6.2 Spatial instability and the Winters and Armi (2014) downslope flow

We mentioned in section 3.2 that the Winters and Armi (2014) solution for optimally controlled stratified flow over topography is a special case where α and β are not independent, but uniquely related. We once again refer to figure 10 of Winters and Armi (2014) and note that the accelerating bottom streamline characteristic of this solution corresponds, in our present formulation, to increasing β downstream. For different values of α, values of β and the fit they produced to the actual solutions of Winters and Armi (2014) are shown in figure 3.7. Clearly, the parameter pairs (α, β) are quite close to the cases studied in section 3.5 and we may expect a stability analysis to yield similar results. Inspection of the eigenfunctions of the fastest growing modes (figure 3.8) and their growth characteristics (table 3.2) confirms this to be the case.

Our discussion so far has been restricted to the temporally growing modes for which the

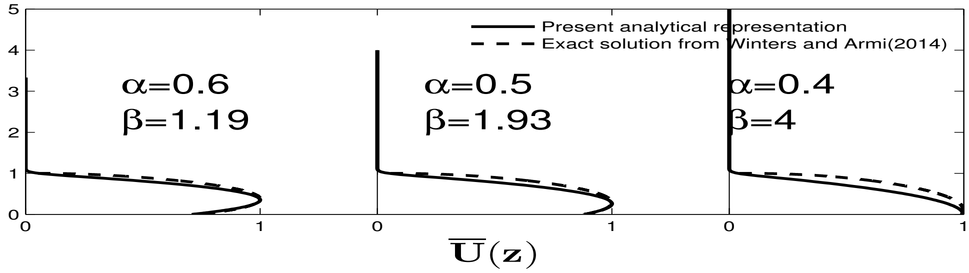

Figure 3.7: The Winters and Armi (2014) background velocity profiles at different downstream locations for the optimally controlled stratified downslope flow. The dashed lines are the exact solutions and the solid lines are the representations of these solutions using β and Q conservation.

.

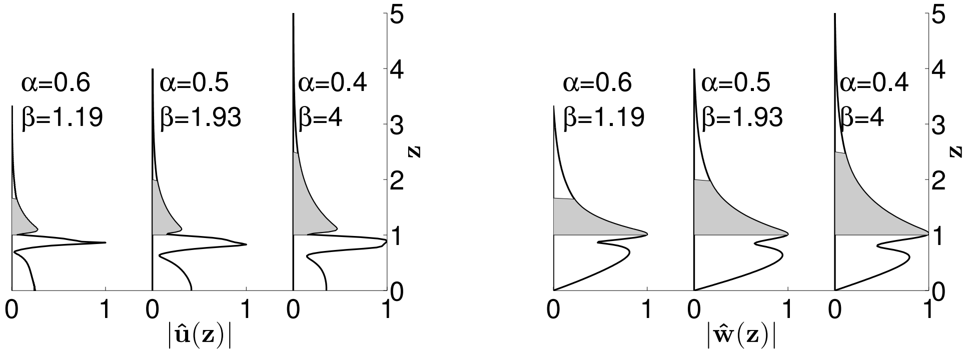

(a)

(b)

Figure 3.8: Normalized eigenfunctions (a)$|\hat{u}(z)|$ and (b)$|\hat{w}(z)|$ for the profiles representative of the solutions of Winters and Armi (2014).

underlying assumption is that the perturbations to the base flow may be distinguished by their horizontal wave numbers. However disturbances could, in principle, also assume the form of a pulse or a localized source vibrating at a fixed frequency, in which case spatially growing modes may be triggered. In the case of the former, growing disturbances are either convected away from the source (convective instability) or grow in situ (absolute instability)destroying the base flow itself for large time. The case of a local periodic forcing constitutes the so-called signaling problem and again may lead to either spatially amplified sinusoids (convective mode) or absolute instabilityHuerre et al. (2000) provides a general discussion of these and other aspects of the spatial instability problem, including an elegant technique for determining if a given flow is absolutely unstable or not.

Downslope flows in nature are subject to a wide range of perturbations and are thus potentially susceptible to both temporal and spatial modes of instability. It can thus be difficult in practice to precisely establish whether an observed instability mode is a purely spatial one or some combination of temporal and spatial modes. However, guided by consideration of the observed growing modes in Winters (2016) and Farmer and Armi (1999), we rule out the possibility of absolute growth at any downstream location. Further, for the sake of simplicity, we stay within the framework of the spatial signalling problem for the reminder of this discussion.

Recall that the optimal, horizontally uniform upstream flow configuration of Winters and Armi (2014) is stable at the blocking location x_b , with Ri_{min} being slightly greater than 1/4. Thereafter, as the upper streamline bifurcates and the flowing layer accelerates, Ri_{min} eventually drops down below $1/4$, allowing for the possibility of unstable modes.

As shown in table 3.2, for the optimally controlled solutions of Winters and Armi (2014), we found that the flow first exhibits temporal instablility where $\alpha \approx 0.67$. Upstream of this location, the growth rates found were too small to pass the spurious mode detection criterion of section 3.4, and downstream of this point, the growth rate appears to increase rapidly, growing to order $O(10^{-1})$ at $\alpha_c \approx 0.6$. The increasing shear at $z = 1$ downstream appears to be offset by the weakening shear at the bottom streamline of the flowing layer along which the flow accelerates as it ascends and plunges down the obstacle, and so the growth rate and *e*-folding scales continue to be $\sim O(10^{-1})$ and $\sim O(1)$ at further downstream locations as well.

The spatial signaling problem in the framework of Gaster (1962)

It is perhaps instructive to picture a curve of marginal stability (CMS),

$$\omega = f(k, \alpha, \beta) \tag{3.24}$$

for this problem, with ω being real valued on one side of the curve and complex on the other. For the upstream flow, $\alpha = 1, \beta = 0$, ω is real valued for all k. The first location where an unambiguously distinguishable unstable mode is encountered is for $\alpha \approx 0.66$. It may thus be reasonably surmised that the point $(k, \alpha, \beta) = (4, 0.66, 0.89)$ in parameter space is close to the CMS for the flow. This in turn allows us to appeal to the framework of Gaster (1962) in which, near the CMS and for a given wavenumber, the growth rate of an unstable spatial mode can be estimated to first order from the corresponding temporal mode through the formula,

$$k_g^s = -\omega_g^T / c_g, \tag{3.25}$$

where

$$c_g = \frac{\partial \omega_r}{\partial k} = \frac{\partial \, \mathrm{Re}(k c_r)}{\partial k} \tag{3.26}$$

is the group velocity of the temporal instability mode, which we compute numerically. Though strictly speaking, we have only argued that the first upstream unstable mode is close to the CMS, we use Eq. (3.25) to approximate the spatial growth rate at locations further downstream as well. In reality, for parameter values that are well away from the CMS, it is probably necessary to consider the dispersion relation in the complex (ω, k) plane to obtain more accurate results for the spatial problem. We shall demonstrate below that ultimately, it is the most upstream unstable mode, close to the CMS, that dominates the spatial growth of instability in streamwise slowly varying controlled downslope flows.

In table 3.2 we found the group velocity to be non-zero and positive in all cases, establishing them as convective rather than absolute modes of instability. Thus we can define an *e*-folding length, analogous to the time scale defined in section 3.5, $L_e = c_g/\omega_g^T$. This is the distance by which a growing mode propagates downstream as it undergoes amplification by a factor of *e*. In field measurements and numerical simulations we detect only the finite amplitude manifestation of an instability, which typically occurs at a downstream position that is of the order of a few *e*-folding lengths.

Evolution to finite amplitude

We reiterate that the flow configurations examined here are approximations to analytical solutions in the purely hydrostatic limit, i.e. when the horizontal length scale is infinite. In this limit, the parallel flow assumption holds everywhere, and so the very first unstable mode will have sufficient downstream distance to grow and undergo amplification to finite amplitude; in the process, it irreversibly changes the flow configuration further downstream through non-linear interactions with the base flow. However, we have not discounted the possibility that when the topography is steep enough, with horizontal length scale L_x, the initial weakly unstable spatial modes will have insufficient distance to grow before the background flow profile changes significantly. Then, these weakly growing modes effectively act as perturbations to the flow further downstream, potentially exciting a stronger unstable mode at some location. In such a case, we would have to examine the growth rates and *e*-folding length scales of the growing modes at various downstream locations, and the first mode that satisfies $L_e \ll L_x$ would be the one that would eventually dominate the other modes and lead the transition to non-linearity.

To investigate this in more detail, suppose that the horizontal length scale for the flow is

L_x. One plausible definition of $L_x \gg H$ is the downstream distance over which the thickness of the flowing layer changes by 10%. Now, for the hydrostatic approximation to hold, we require $L_x/H \sim O(10)$. Since we are interested in the lower limit, suppose that $L_x/H \approx 10$. Now, recalling that in our computations, the lengths are non-dimensionalized by h, the local flowing layer thickness, from table 3.2, the growing mode at $\alpha = 0.66$ has $L_e = 4.05h = 4.05\alpha H = 2.68H$. So an initial disturbance at this location will have sufficient downstream distance to grow to $\exp 10/2.48 \approx 42$ times its initial magnitude before the background profile changes significantly. This is more than an order of magnitude amplification and hence will manifest physically in observations and numerical simulations at $h/H \approx 0.56$ before non-linearities eventually modify the character of the background flow itself further downstream. Thus even at the boundary of the hydrostatic regime when $L_x/H \approx 10$, it appears that the very first spatial mode excited that has $O(1)$ e-folding length scale is the one that dominates the instability process in these flows.

This result is also in agreement with figure 12 of Farmer and Armi (1999) where, for a flow with $L_x/H \sim O(10)$, the centre of the first finite amplitude vortex core in the lee, corresponding to the first physically observed overturning shear instability, is seen to occur at roughly $X = 50m$ giving $\alpha \approx 0.55$. Further, recent work by Winters (2016) also seems to corroborate this. Figure 3.9 shows the isopycnals from a statistically steady, 3D simulation (movie attached) of stratified flow over topography matching the optimal upstream solution of Winters and Armi (2014), again for a flow with $L_x/H \sim O(10)$. The simulation uses the same downstream condition as in figure 4 of Winters (2016). It is noted in his paper that the downstream condition has no effect on the flow over the sill in the region where this particular instability is observed. It primarily affects the point of downstream flow separation and the strength of the internal hydraulic jump. For our purposes, a quasi-steady state was attained on time and spatial averaging over 6.25 buoyancy periods. Winters (2016) has further details on the modeling and on how the flow solutions are affected by the downstream condition.

As anticipated by the analytical solutions of Winters and Armi (2014), upstream blocking, streamline bifurcation and formation of an isolating layer are clearly observed in this simulation. Further the flow exhibits instability along the upper edge of the flowing layer, with finite amplitude features manifesting within the shaded region $0.5 \leq h/H \leq 0.6$. The location of the repeated overturns is also consistent with our prediction above that finite amplitude billows seen at $h/H \approx 0.56$ are in fact the physical manifestation of the spatially growing mode triggered further upstream at $h/H \approx 0.66$

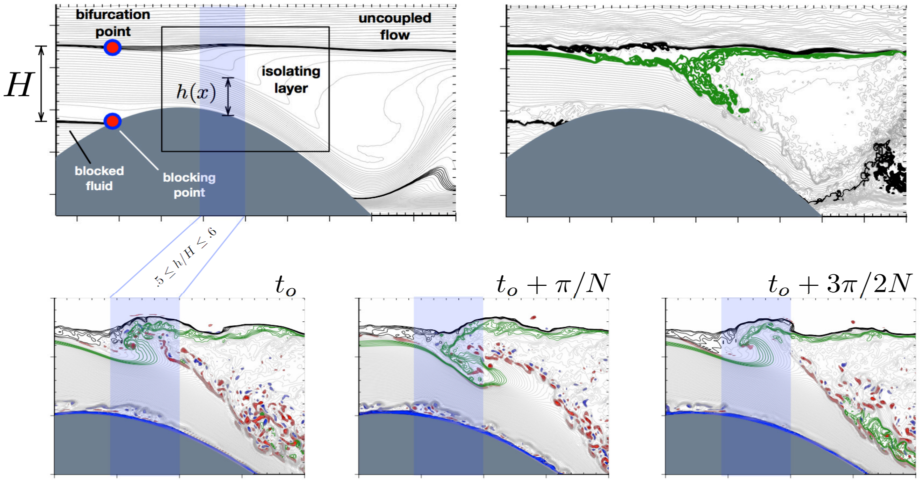

Figure 3.9: (Winters (2016)) Isopycnals and vorticity from a statistically steady non-linear simulation of stratified flow over a smooth topography matching the optimal upstream solution of Winters and Armi (2014). L_x/H for this flow is $\sim O(10)$, i.e. it is at the boundary of the hydrostatic regime. The top frame displays the time and cross-stream averaged flow (left) that exhibits the essential features of the flow and also an instantaneous snapshot (right). The bottom panel shows three snapshots of the flow spaced about half a buoyancy period apart. Shear instability is observed at the upper edge of the flowing layer, and finite amplitude billow structures are first perceived within the shaded region $0.5 \leq h/H \leq 0.6$, where repeated overturning and plunging of the lower isopycnals (coloured green for visualization purposes) is also visible. The red and blue colours indicate positive and negative vorticity extrema respectively.

3.6.3 Applicability to other flow regimes

A final note is that, while the stability analysis described here is formally valid only for the asymptotic regime of a tall mountain barrier with slow flow and/or strong stratification, even in situations where there is no blocking and upstream influence, the dynamics of the downstream flow evolution - viz. an accelerating thinning jet with a stagnant mixed layer aloft - are largely identical, as can be seen, for example in the work of Lilly (1978) and Scinocca and Peltier (1989). We therefore speculate that this overall view of the stability problem carries over to other regimes, including those with an initial uniform upstream flow profile.

3.7 Conclusion

We have analyzed the linear stability of stratified flow profiles that are typically encountered in the downslope region of topographical features in the ocean and atmosphere. By considering idealized representations of jet-like profiles that emerge from a theoretical hydraulic view of the problem as in Winters and Armi (2014), we obtain growth rates that are between 1 and 2 orders of magnitude larger than those seen in the linear stability analysis of Peltier and Scinocca (1990) and Smith (1991), and are consistent with the results of the non-linear numerical simulations of Scinocca and Peltier (1989).

We believe that it is the formal inclusion of a stagnant, homogeneous isolating layer into the stability analysis that is responsible for such a dramatic improvement in the prediction of linear stability theory. The presence of a deep isolating layer above a strongly sheared, jet-like flowing layer creates conditions that are favourable for the nucleation of shear instabilities. The sharp gradients in the horizontal velocity eigenfunction at $z = 1$ and the fact that larger growth rates were obtained on solving the Rayleigh equation for the corresponding unstratified velocity profiles, unambiguously identify them as K-H shear modes. The wave-interaction interpretation of shear flow instability appears to offer a satisfactory explanation for the observed instabilities.

Further, an analysis of the spatial stability problem in the framework of small deviations from the marginal curve of stability is shown to yield $O(1)$ e-folding length scales. These signal transition to non-linearity at downstream distances that are consistent with those reported in observations and numerical simulations of downslope flows.

This chapter is a reprint, in full, of the material as it appears in Jagannathan, A., Winters, K.B., Armi, L., "Stability of stratified downslope flows with an overlying stagnant isolating layer", *Journal of Fluid Mechanics*, 810, 392411, doi:10.1017/jfm.2016.683. The dissertation author was the primary investigator and author of this paper.

Chapter 4

The dynamical link between hydraulic control and wave excitation aloft in blocked stratified flow over topography

4.1 Introduction

Stratified flow over dynamically tall topography is characterized by the formation of a hydraulically controlled plunging flow above a layer of blocked stagnant fluid upstream. The top of this asymmetric overflow is marked by a bifurcating isopycnal which partially isolates it from the flow further aloft. When the stratification is uniform, the thickness of the overflow and hence the height of the bifurcating isopycnal can be analytically predicted by combining an optimal hydraulic control condition with a kinematic constraint for the volume transport (Winters and Armi, 2014). While these predictions for the controlled flow component have been confirmed in the numerical experiments of Jagannathan et al. (2018), one feature that cannot be satisfactorily explained by hydraulic theory alone is the presence of wave-like oscillations further aloft.

The observations of controlled stratified flows in the Sierras by Armi and Mayr (2015) suggest that the flow aloft develops as a response to the ‘virtual topography ’ formed by the top of the crest-controlled overflowing layer. The goal of this study is to obtain a deeper understanding of the dynamical connection between the controlled flow component and wave-excitation further aloft. Our experimental approach is to again consider flow across dynamically tall obstacles, but now for stratification profiles that include a sharp density step embedded within an otherwise uniformly stratified fluid. Such abrupt density variations can be encountered in, for example, atmospheric inversion layers and at the ocean pycnocline. We will analyze how the flow characteristics change as the vertical location of the density step is varied across the depth range of the corresponding uniformly stratified overflow. In particular, we seek to understand how the presence of a density step affects the height of the bifurcating isopycnal and in turn, the wave response aloft.

In his simulations of atmospheric flows with a homogeneous lower layer capped by a sharp temperature inversion, Vosper (2004) found that the flow response depends sensitively on the height and strength of the inversion. As the inversion increases in magnitude and moves closer to the crest, the flow transitions from a regime where only vertically propagating disturbances exist to one that is characterized by lee-waves propagating at the level of the inversion. At some critical inversion strength, an asymmetric hydraulic response is triggerred and the inversion itself plunges down the lee. The flow eventually returns back to a subcritical state downstream via an internal hydraulic jump..

Jiang (2014) showed that when the lower layer is unstratified, reduced gravity shallow water theory can be used to describe the overflow provided the inversion is sufficiently strong and, or the ambient flow speed is small. In that case, the flow in the upper stratified layer can be regarded as ‘passive’ in the sense that any pressure perturbations there do not affect the flow in the layer beneath.

Jagannathan et al. (2018) investigated flow splitting effects on the controlled overflowing layer in stratified flows encountering dynamically tall, long mountain ridges. In these flows, the fluid below a depth δ from the crest remains stagnant or flows around the sides of the ridge. Above this blocked fluid is a plunging, asymmetric overflow that is hydraulically controlled at the crest. A schematic of this flow in a purely 2D setting is shown in Fig. 4.1a. For a given obstacle height h_m, upstream flow speed V_∞ and stratification N_0, the topographic Froude number is defined as $Fr = V_\infty / N_0 h_m$. Winters and Armi (2014) showed that when blocking effects are significant, or equivalently, when $Fr \ll 1$, the optimally controlled overflow has a parabolic velocity profile upstream of the blocking location, with the layer thickness H and volume transport Q coupled through the control relationship $Q = NH^2/\pi$. The height of the bifurcating isopycnal is then given by $z = z_{op} = h_m - \delta + H$.

For a given upstream flow configuration, H is then found by solving a kinematic equation for the overflow transport (e.g. Winters and Armi, 2014; Jagannathan et al., 2018). These predictions were further corroborated in Jagannathan et al. (2018), where it was also noted that, contrary to the Winters and Armi (2014) assumption, the flow above the bifurcating isopycnal is not completely dynamically uncoupled from the controlled flow beneath. Rather, the asymmetric plunging overflow acts like a virtual topography for the flow aloft in a manner similar to that described by Armi and Mayr (2015), launching vertically propagating internal waves of wavelength about $2\pi V_\infty / N_0$.

We now further explore the connection between the topographically controlled flow in the lowest overflowing layer and the wave response aloft, in blocked flows that also feature a sharp stratification gradient above crest level. This flow configuration is shown schematically in Fig. 4.1b. A density jump of magnitude $\Delta\rho_i$ is located at $z = z_0 < z_{op}$, or below the bifurcation level in the corresponding uniformly stratified case. The thickness of the interface is assumed to be finite but small, that is $\delta_i / H \ll 1$, so that the stratification changes abruptly, $N_{\delta_i} / N_0 \gg 1$, where N_{δ_i} and N_0 are the statification within and away from the interface respectively.

We will show that the spatial placement of the density step strongly influences the height of the bifurcating isopycnal, which in turn determines the strength of the wave perturbations excited above the controlled overflow. Further we will also demonstrate that the amplitude of the wave is directly connected to the nature of the hydraulically controlled overflow and in particular depends sensitively on whether or not the density interface is drawn down asymmetrically across the crest as part of the plunging overflow.

4.2 Theoretical framework for blocked controlled flows in the presence of a sharp density step

Setting $Fr = O(0.1)$ leads to upstream blocking and thus guarantees an asymmetric flow response with hydraulic control at the crest. For the uniformly stratified case depicted in Fig. 4.1a, the volume conservation equation (see Jagannathan et al., 2018) is,

$$N_0 H^2/\pi = V_\infty(h_m + 7H/8) \tag{4.1}$$

and the overflow layer depth H is the positive root of this quadratic,

$$H = \frac{\frac{7\pi V_\infty}{8N_0} + \sqrt{\left(\frac{7\pi V_\infty}{8N_0}\right)^2 + \frac{4\pi V_\infty h_m}{N_0}}}{2}, \tag{4.2}$$

which can be written in terms of h_m and Fr as

$$H = \frac{\frac{7\pi}{8} h_m Fr + h_m \sqrt{\left(\frac{7\pi}{8}\right)^2 Fr^2 + 4\pi Fr}}{2}. \tag{4.3}$$

Thus for a chosen Fr, H is directly proportional to h_m.

Keeping the other parameters same, we now consider the effect of including a strong density step within the stratification profile. When the step is placed at $z_0 > z_{op}$, we expect to recover the Winters and Armi (2014) solution of a parabolically sheared upstream overflow of

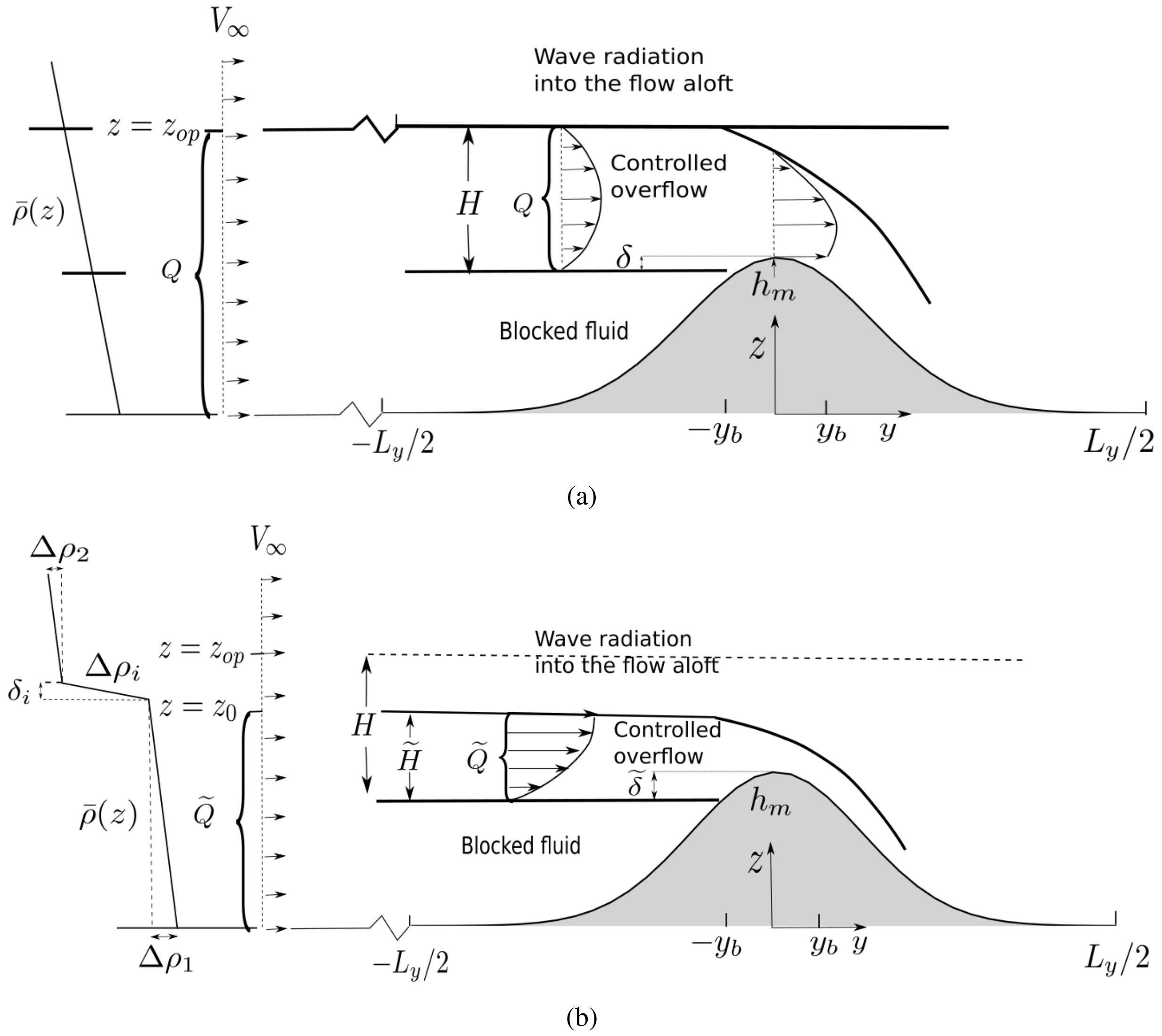

Figure 4.1: (a) Schematic of low Fr controlled asymmetric overflow over an infinite ridge for the case of uniform upstream stratification and flow speed. The upstream fluid below a depth δ from the crest is blocked. $y = -y_b$ is the streamwise coordinate of the blocking location and Q denotes the volume transport within the overflow, which matches the far upstream transport as shown. $y = -L_y/2$ and $y = L_y/2$ are the streamwise computational boundaries. The optimally controlled overflow has a parabolic velocity profile, with the height of the bifurcating isopycnal being $z = z_{op}$. (b) As in Fig. 4.1a but for the case when a density step is present in an otherwise uniformly stratified fluid with $Fr = V_\infty/N_0 h_m \ll 1$. The density step $\Delta\rho_i$ is large and the interface is thin relative to H ($\delta_i/H \ll 1$), so that $N_{\delta_i}/N_0 \gg 1$, where N_{δ_i} and N_0 denote the stratification within and away from the interface respectively. For $z = z_0 < z_{op}$, the upstream thickness of the overflow is $\widetilde{H} < H$ and the velocity profile deviates from the optimal parabolic shape as indicated.

thickness H (Fig. 4.1a). However, in the depth range $h_m < z_0 < z_{op}$, we anticipate that the density step will affect the height of the bifurcating isopycnal and hence also the thickness $\widetilde{H}$ of the overflow. This is fundamentally different from uniformly stratified low Fr flows considered in Jagannathan et al. (2018), where the overflow layer depth is part of the solution and is determined by solving equations of the form Eq. (4.1) that relate a dynamical condition for optimal crest control with kinematic flux constraints.

Preliminary simulations indicate that when $z_0 < z_{op}$ the upstream flow speed, rather than being shaped as a parabolic jet, is characterized by a peak at $z = z_0$ and is thus better represented as a half-parabola (Fig. 4.1b). Recall that in the Winters and Armi (2014) solution, the blocking scale is dynamically related to the thickness of the parabolic overflow as $\delta = H/8$. Here, we postulate that the dynamical blocking scale is $\widetilde{\delta} = \widetilde{H}/4$ where $\widetilde{H}$ is now the thickness of the half-parabola. Assuming that the overflowing layer terminates just below the density jump, its volume transport $\widetilde{Q}$ must match $V_\infty z_0$ (see Fig. 4.1b). The prediction for its peak speed v_m is then obtained by solving the conservation equation for volume transport,

$$\widetilde{Q} = V_\infty z_0 = (2/3)\widetilde{H} v_m, \tag{4.4}$$

with $\widetilde{H} = z_0 - h_m + \delta = z_0 - h_m + \widetilde{H}/4$, yielding

$$\widetilde{H} = \frac{4}{3}(z_0 - h_m). \tag{4.5}$$

Substituting Eq. (4.5) in Eq. (4.4), we obtain

$$v_m = \frac{9}{8}\frac{V_\infty z_0}{(z_0 - h_m)}, \tag{4.6}$$

which furnishes a complete description of the overflow profile in terms of the known problem parameters V_∞, h_m and z_0.

The underlying basis of the framework being developed is hydraulic control and across-crest asymmetry. Therefore, for the overflow profile constructed above to be a physically realizable one, a necessary condition is that it must be subcritical upstream. To check that it is so, we take the bottom and top of the overflowing layer as rigid boundaries of a waveguide, and solve the Taylor-Goldstein equation (using the solver described in appendix C) to determine whether the predicted overflow supports at least one upstream propagating internal wave mode. Assuming a background velocity profile $\bar{V}(z)$, uniform stratification N_0 and a wave-like disturbance with streamfunction $\psi = \phi(z)\exp(il(y-ct))$, the Taylor Goldstein equation for a vertical wave mode $\phi(z)$ with speed c is

$$\phi'' - l^2\phi + \frac{N_0^2}{(\bar{V}(z)-c)^2}\phi - \frac{1}{(\bar{V}(z)-c)}\frac{\mathrm{d}^2\bar{V}(z)}{\mathrm{d}z^2}\phi = 0 \tag{4.7}$$

where prime denotes differentiation with respect to z, $u = \mathrm{d}\psi/\mathrm{d}z$ and $w = -\mathrm{d}\psi/\mathrm{d}x$.

For a semi-parabolic velocity distribution of the form

$$\bar{V}(z) = 4v_m\left(\frac{z}{2\widetilde{H}} - \frac{z^2}{4\widetilde{H}^2}\right), \tag{4.8}$$

Eq. (4.7) can be written as

$$\phi'' - l^2\phi + \frac{N_0^2}{v_m^2\left[4\left(\frac{z}{2\widetilde{H}} - \frac{z^2}{4\widetilde{H}^2}\right) - \frac{c}{v_m}\right]^2}\phi + \frac{2}{\widetilde{H}^2\left[4\left(\frac{z}{2\widetilde{H}} - \frac{z^2}{4\widetilde{H}^2}\right) - \frac{c}{v_m}\right]}\phi = 0. \tag{4.9}$$

with boundary conditions $\phi = 0$ at $z = 0, \widetilde{H}$. We now non-dimensionalize z as

$$\widehat{z} = z/\widetilde{H}, \tag{4.10}$$

and confine attention to the fastest, long internal wave modes with $l \to 0$ that determine the criticality of the flow. Eq. (4.9) then becomes

$$\frac{1}{\widetilde{H}^2}\phi'' + \frac{N_0^2}{v_m^2\left[4\left(\frac{\widehat{z}}{2}-\frac{\widehat{z}^2}{4}\right)-\frac{c}{v_m}\right]^2}\phi + \frac{2}{\widetilde{H}^2\left[4\left(\frac{\widehat{z}}{2}-\frac{\widehat{z}^2}{4}\right)-\frac{c}{v_m}\right]}\phi = 0. \tag{4.11}$$

with the boundary conditions $\phi = 0$ at $\widehat{z} = 0, 1$.

It is easy to show that for any $\gamma > 0$, Eq. (4.11) is invariant to the transformation $h_m \to \gamma h_m$, $z_0 \to \gamma z_0$ and $N_0 \to N_0/\gamma$. First we note that this transformation leaves Fr unchanged. Next, from Eqs. (4.5) and (4.6), we obtain $\widetilde{H} \to \gamma\widetilde{H}$, while v_m stays the same. Substituting these values in Eq. (4.11) transforms the equation into itself. Note that this would not be the case without the long wave approximation $l \to 0$ that gets rid of the second term in Eq. (4.9).

If instead, we make the transformation $h_m \to \gamma h_m$, $z_0 \to \gamma z_0$ and $V_\infty \to \gamma V_\infty$, Fr is once again unchanged, but Eq. (4.11) now becomes

$$\frac{1}{\widetilde{H}^2}\phi'' + \frac{N_0^2}{v_m^2\left[4\left(\frac{\widehat{z}}{2}-\frac{\widehat{z}^2}{4}\right)-\frac{\widehat{c}}{v_m}\right]^2}\phi + \frac{2}{\widetilde{H}^2\left[4\left(\frac{\widehat{z}}{2}-\frac{\widehat{z}^2}{4}\right)-\frac{\widehat{c}}{v_m}\right]}\phi = 0, \tag{4.12}$$

where $\widehat{c} = c/\gamma$. In other words, the eigenvalues of the rescaled problem differ from those of the original one by a factor of γ. However, the crucial point is that Eq. (4.12) has a negative eigenvalue if and only if Eq. (4.11) has one. Thus in particular, for a given Fr, there exists a unique $\alpha > 1$ and a corresponding $z_{critical} = \alpha h_m$ such that for $z_{critical} < z_0 < z_{op}$, the waveguide supports at least one upstream propagating internal wave mode with $c < 0$ and is thus subcritical.

As the upstream overflow is assumed to terminate just below the density interface, the interface itself experiences only small linear perturbations. Therefore the flow aloft responds to a virtual topography of height V_∞/N_{δ_i}, which is the energetic estimate for maximum vertical excursion of isopycnals within the interfacial layer. This gives a perturbation flow speed $N\frac{V_\infty}{N_{\delta_i}}$, which is small relative to V_∞ whenever $N/N_{\delta_i} \ll 1$.

If $z_{critical} > h_m$, then in the depth range $h_m < z_0 < z_{critical}$, the predicted upstream profile will be supercritical, which is in violation of the assumption of hydraulic crest control. To resolve this inconsistency, we first note that shifting the upper boundary of the waveguide to include the density interface will increase the mean stratification of the waveguide and thus allow faster upstream propagating waves. Therefore a plausible way to maintain subcriticality is to require that the density interface be part of the controlled overflow. Proceeding on this basis and assuming that the velocity decreases linearly within the interfacial layer to the ambient flow speed V_∞, the volume transport equation for the overflow will then be modified to

$$\widetilde{Q} = V_\infty(z_0 + \delta_i) = (2/3)\widetilde{H}v_m + \frac{(v_m + V_\infty)}{2}\delta_i. \tag{4.13}$$

Next we note that the energetic estimate for maximum isopycnal displacement in the upper stratified layer is V_∞/N_0. As the overflow develops across the crest, the top of the density interface forms a plunging virtual topography for the flow above leading to the excitation of a vertically propagating internal wave of wavelength $2\pi V_\infty/N_0$, amplitude V_∞/N_0 and a corresponding flow speed perturbation of approximately $N_0\frac{V_\infty}{N_0} = V_\infty$. The complete solution then is a controlled overflowing layer shaped as a half-parabola upstream and acting as a virtual topography for a large mountain wave of perturbation speed V_∞. When the density interface is located below $z = z_{critical}$, the upstream flow fails to be subcritical even after including the density interface, which implies that in addition to the interfacial layer, some portion of the relatively weakly stratified fluid above must also participate in the controlled overflow.

The emerging picture is of an intrinsic connection between hydraulic control of the lowest overflowing layer in direct contact with the topography and wave excitation aloft. The latter is essentially a response to the shape of the virtual topography formed by the top of the density interface and depends sensitively on the dynamics of the hydraulic flow component. We will present numerical flow solutions for two cases, showing a plunging and non-plunging density interface respectively, which will demonstrate the applicability of the theoretical framework developed here.

4.3 Model description

The governing equations are the two dimensional, inviscid Navier-Stokes equations in the non-rotating, Boussinesq limit. The numerical model used for the computations is the spectral large eddy solver *flow_solve* described in Winters and de la Fuente (2012). We consider a background state characterized by a far upstream flow speed V_∞ and stratification $N(z)$ incident on a hydrostatic Gasussian topography

$$h = h_m exp(-y^2/\sigma_y^2); \qquad h_m/\sigma_y = 1/6. \tag{4.14}$$

The topography is centered on a domain of width $L_y = 33\sigma_y$ and is incorporated via the immmersed boundary setup discussed in Winters and de la Fuente (2012). Note that while the obstacle is gently sloping, the numerical model itself is non-hydrostatic. The height of the computational domain is $L_z = 6h_m$ and the density profiles considered are as shown in Fig. 4.1b. In the computations, the density jump $\Delta\rho_i$ over a height δ_i is represented using a hyperbolic tangent function as

$$\begin{aligned}\rho = \rho_0 + 0.5\Delta\rho_2\left(\frac{L_z - z}{L_z - z_0}\right)\left[1 + tanh\left(\frac{2(z - z_0 - \delta_i/2)}{\delta_i}\right)\right] \\ + 0.5\left(\Delta\rho_2 + \Delta\rho_i + \left(\frac{z_0 - z}{z_0}\right)\Delta\rho_1\right)\left[1 - tanh\left(\frac{2(z - z_0 - \delta_i/2)}{\delta_i}\right)\right]\end{aligned} \tag{4.15}$$

so that the bottom of the jump is located at $z = z_0$. The corresponding stratification profiles are then approximately given by

$$N(z) \approx \begin{cases} N_{\delta_i}; & |z - z_0 - \delta_i/2| \leq \delta_i/2 \\ N_0; & |z - z_0 - \delta_i/2| > \delta_i/2 \end{cases} \tag{4.16}$$

We fix the topographic Froude number Fr at 0.16 and consider strong density steps characterized by the dimensional values $N_0 = 10^{-2}s^{-1}$ and $N_{\delta_i} = 8.6N_0 = 8.6 \times 10^{-2}s^{-1}$. In Jagannathan et al. (2018), we showed that for a blocking scale $\widetilde{\delta}$, the appropriate inner horizontal length scale for the overflow is the half-width of the obstacle at the blocking level $\sigma_{y_{\widetilde{\delta}}}$. The smallest vertical length scale is the thickness of the density interface δ_i which, in our experiments, is much smaller than the blocking scale $\widetilde{\delta}$. To resolve these inner length scales, we choose a grid spacing $\Delta z \approx \delta_i/6$ and $\Delta y \approx \sigma_{y_{\widetilde{\delta}}}/10$.

A sponge layer of thickness $L_z/4$ near the upper boundary radiates vertically propagating waves and the upstream boundary condition evolves slowly through an iterative scheme (Jagannathan et al., 2018) that accounts for upstream influence of the topography. As in Jagannathan et al. (2018), downstream turbulence is modelled using a sixth order hyperdiffusion operator. The background flow speed is quickly ramped up from rest over ten time steps and the criterion for quasi-steadiness is that at the blocking location, the peak speed of the overflow deviates by less than 1% over subsequent iterations.

4.4 Numerical results

Setting the topographic Froude number Fr equal to 0.16 in Eq. (4.2) yields $H = 0.96h_m$. That is, the bifurcating isopycnal in the uniformly stratified case is at $z_{op} = h_m + (7/8)0.96h_m = 1.84h_m$. Any change in stratification above $z = z_{op}$ will not impact the overflow which will continue to be optimally controlled. For example, Fig. 4.2, which shows the quasi-steady flow for a strong density interface at $z_0 = 2.23h_m$, characterized by $N_{\delta_i}/N_0 = 8.6$, reveals that the overflow bifurcates at around $z = z_{op}$ as opposed to $z = z_0$. The vertical profile of the overflow at the upstream blocking location (Fig. 4.3) also agrees closely with the parabolic prediction of Winters and Armi (2014).

On the other hand, when a strong density step is located below $z = z_{op}$, our theoretical

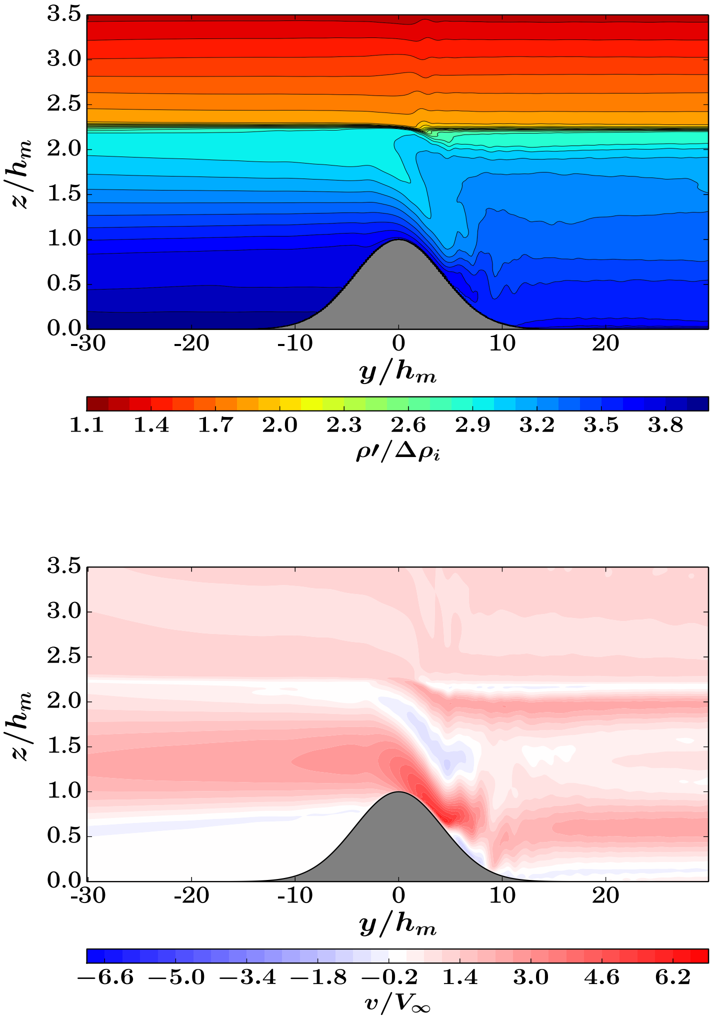

(a)

Figure 4.2: Quasi-steady flow field for 2D $Fr = 0.16$ flow over an infinite ridge with a density step characterized by $N_{\delta_i}/N_0 = 8.6$ located at $z_0 = 2.23h_m$. (Top) Isopycnal lines and contours and (bottom) streamwise velocity contours. Flow is from left to right.

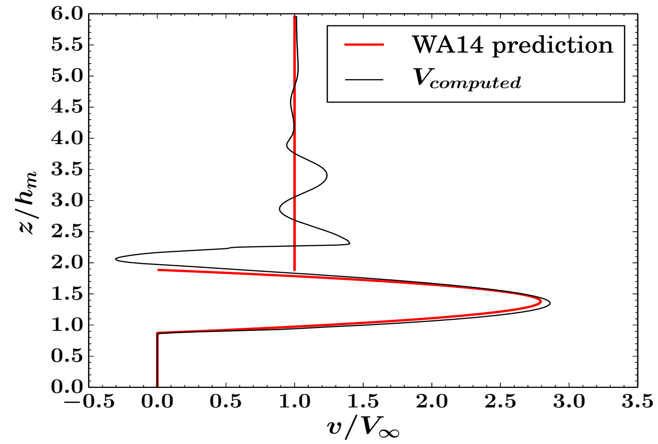

Figure 4.3: Vertical profile of the steady streamwise velocity at the blocking point $y = -y_b$ for $Fr = 0.16$ flow over an infinite ridge with a sharp density step located at $z_0 = 2.23h_m$. The Winters and Armi (2014) parabolic overflow prediction is shown in red.

framework proposes that the bifurcation will occur at $z = z_0$ when $z_{critical} < z_0 < z_{op}$ and between $z = z_0 + \delta_i$ and $z = z_{op}$ when $h_m < z_0 < z_{critical}$. Table 4.1 lists the speed of the fastest upstream propagating internal wave mode within the waveguide formed by the predicted semi-parabolic overflow for different values of z_0 at $Fr = 0.16$. When the bottom $z = z_0$ of the interface is above a height $z_{critical} = 1.45h_m$ from the ground but below $z = z_{op} = 1.84h_m$, we note that the overflow is subcritical without including the density interface. For an interface that is below $1.35h_m < z_0 < z_{critical}$, the overflow must include the interface in order for it to be subcritical. Sample flow profiles used in performing the wave speed computations for the case $z_0 = 1.35h_m$ are shown in Fig. 4.4.

We found that when $z_0 <\approx 1.33h_m$, the semi-parabolic prediction fails to be subcritical even after including the interface. Our simulations indicate that the overflow nonetheless continues to be asymmetric and hydraulically controlled, but its shape and thickness progressively deviate from the predictions of 4.2 as z_0 moves closer to crest level.

We now present results from two numerical experiments in which a sharp density interface of strength $N_{\delta_i} = 8.6 \times 10^{-2}\ s^{-1}$ is located at $z_0 = 1.73h_m$ and $z_0 = 1.35h_m$ for which the

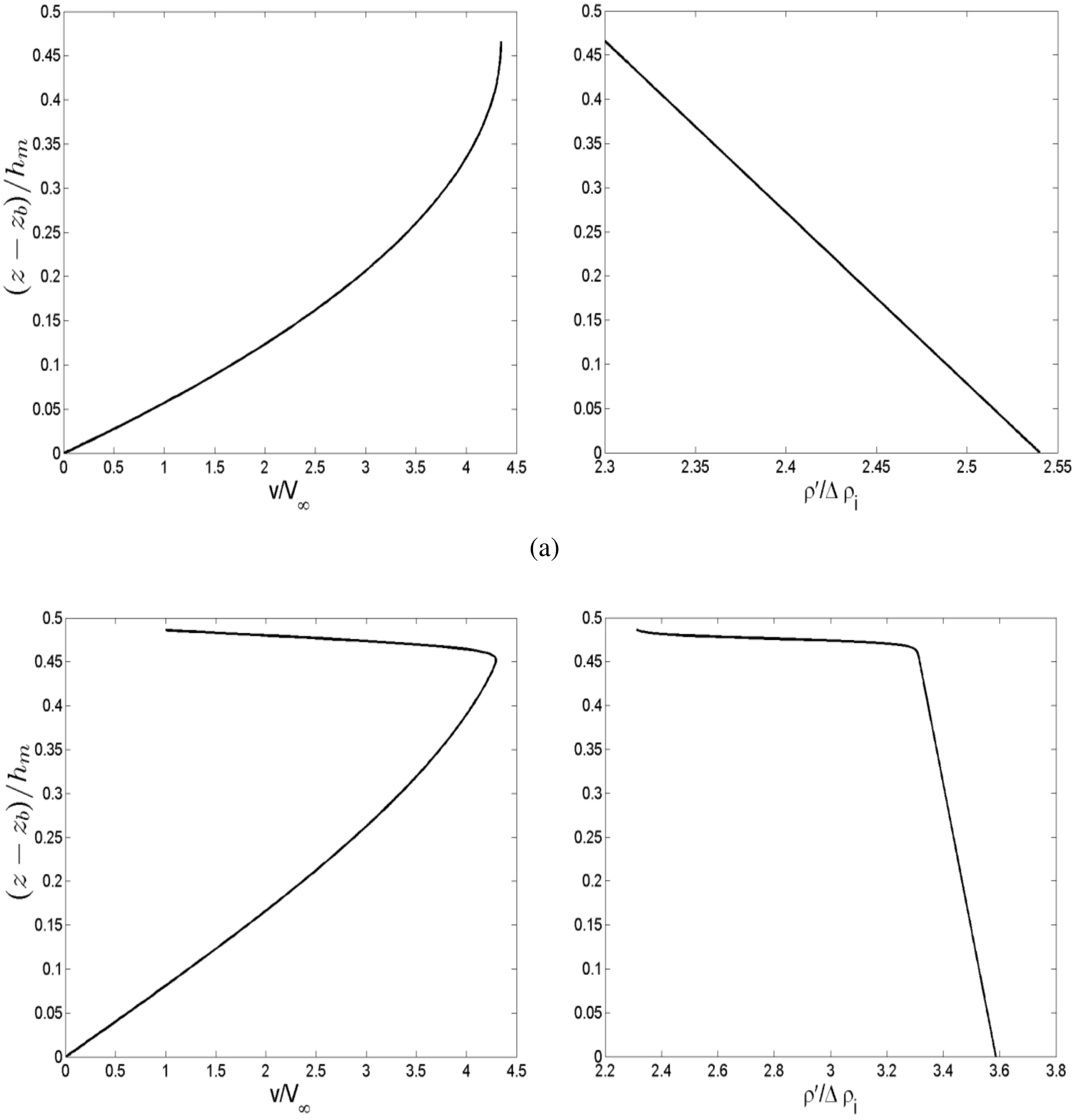

Figure 4.4: Prediction of vertical profiles of the velocity and density within the overflowing layer for the case $z_0 = 1.35h_m$, with $N_{\delta_i}/N_0 = 8.6$. (a) Excluding the density interface, (b) Including the density interface.

Table 4.1: Speed of fastest upstream propagating internal wave mode within the waveguide formed by the semi-parabolic overflow for different locations of the density step at $Fr = 0.16$

z_0/h_m	$c_{up_{max}}/V_\infty$	
	Excluding density interface	Including density interface
1.75	-0.64	-0.83
1.65	-0.35	-0.54
1.55	-0.11	-0.27
1.45	10^{-5}	-0.07
1.35	5.4×10^{-5}	-10^{-3}
1.25	7.5×10^{-4}	4×10^{-4}

waveguide analysis predicts a non-plunging and plunging interface respectively.

4.4.1 Non-plunging interface: weak perturbations aloft

We first consider the case $z_0 = 1.73h_m$. From table 4.1, the fastest upstream propagating wave mode within the predicted semi-parabolic overflow has a speed $c_{up_{max}} = -0.64V_\infty$ and is therefore subcritical as required. Fig. 4.5 shows isopycnals and velocity contours of the quasi steady flow. Like in the uniformly stratified flows considered by Jagannathan et al. (2018), upstream blocking and across-crest asymmetry are fundamental features of the flow. Also seen is an accelerating downslope flow beneath a wedge of nearly stagnant mixed fluid, identifiable as the isolating layer. However, the key distinguishing aspect of the flow compared to the uniformly stratified case is that the location of the bifurcating isopycnal is at the bottom of the density interface $z_0 = 1.73h_m$ and not at $z_{op} = 1.84h_m$.

Directly above the crest, the top of the interface is displaced slightly upward. This is a consequence of imperfect isopycnal bifurcation in a real flow and also shear instability (e.g. Jagannathan et al., 2017) at the top of the plunging downslope flow. Significantly, the interface does not plunge across the crest as part of the overflow. Thus the flow aloft can be regarded as a high Froude number response to the virtual topography formed by the nearly flat density interface and comprises only weak linear perturbations. The maximum flow speed perturbation is around $0.15V_\infty$ which agrees well with the analytical estimate of section 4.2, $V_\infty N_0/N_{\delta_i} \approx 0.12V_\infty$ for the

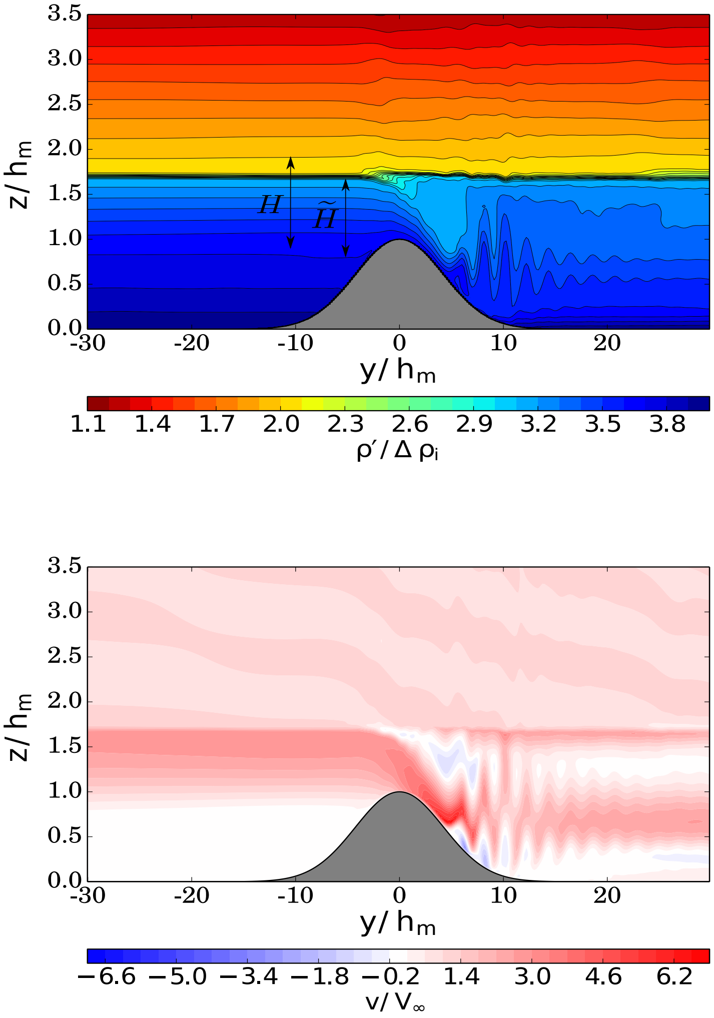

(a)

Figure 4.5: Same as Fig. 4.2 but for $z_0 = 1.73h_m$

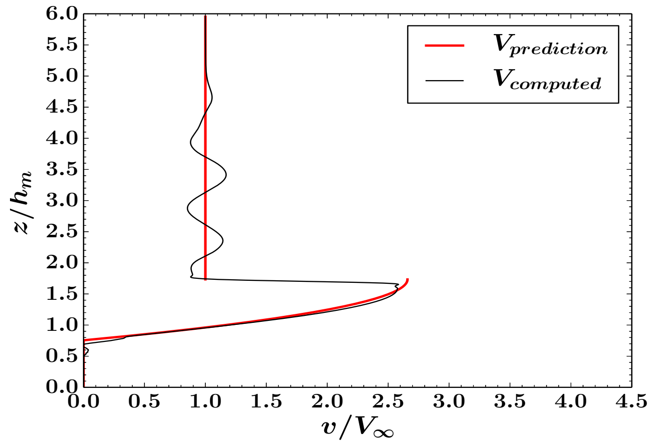

Figure 4.6: Vertical profile of the steady streamwise velocity at the blocking point $y = -y_b$ for $Fr = 0.16$ flow over an infinite ridge with a sharp density step located at $z_0 = 1.73h_m$. The prediction in red is based on the analytical framework of section 4.2 .

values of N_0 and N_{δ_i} considered.

Fig. 4.6 shows that the overflow profile at the upstream blocking location has a semi-parabolic shape as predicted. Further, both the peak speed of the overflow and the blocking depth agree well with the values obtained by solving the transport equation Eq. (4.4). Above this overflow, small amplitude oscillations ($v_0/V_\infty \approx 0.15$) are present, consistent with a vertically propagating linear mountain wave of wavelength $2\pi V_\infty/N_0$.

4.4.2 Plunging interface: Large amplitude wave aloft

Moving the density step further down to $z_0 = 1.35h_m$, table 4.1 now shows that the semi-parabolic overflow by itself, is supercritical, but becomes slightly subcritical when capped by the strong density interface. Thus our theoretical framework predicts that the density interface must participate in the hydraulically controlled overflow. This prediction is corroborated in Fig. 4.7 which shows the interfacial layer being drawn down asymmetrically across the crest. The large isopycnal displacement associated with the descent of the interface in turn excites a strong vertically propagating mountain wave aloft.

In Fig. 4.8, we observe that peak speed within the overflowing layer is now well-predicted by the volume conservation equation Eq. (4.13) which assumes a plunging interface rather than Eq. (4.4) which does not. The amplitude of the flow speed perturbation aloft is significantly larger than in the case of the non-plunging interface being about equal to V_∞, which is again consistent with the energetic prediction of section 4.2.

4.5 Discussion and conclusions

A discontunuity in the vertical profile of density can have a profound effect on the dynamics of fluid flow over topography. In particular, the presence of a strong density step above crest level can trigger an isopycnal bifurcation and subsequent transition to a controlled downslope flow state. In the absence of upstream blocking, the location of the bifurcating isopycnal coincides with that of the step.

The flows considered here feature both upstream blocking and a strong density step above crest level . As a result, the dynamical evolution of the flow is influenced not only by the magnitude and height of the density step, but also by its location relative to z_{op}, or the bifurcation level in the corresponding uniformly stratified case. This latter factor determines whether the flow is parabolic or semi-parabolic in shape, whether the density interface plunges across the crest as part of the overflow and the response of the flow aloft to the virtual topography formed by the top of the interface.

The observations of Armi and Mayr (2015) showed that when a neutrally stratified layer is capped by a strong density inversion, the flow aloft responds to the virtual topography formed by the inversion layer. Depending on the ambient conditions, the overflow may be subcritical, supercritical or hydraulically controlled and asymmetric across the crest. The exact nature of the overflow and the corresponding shape of the inversion across the crest are well described using single-layer reduced-gravity hydraulics.

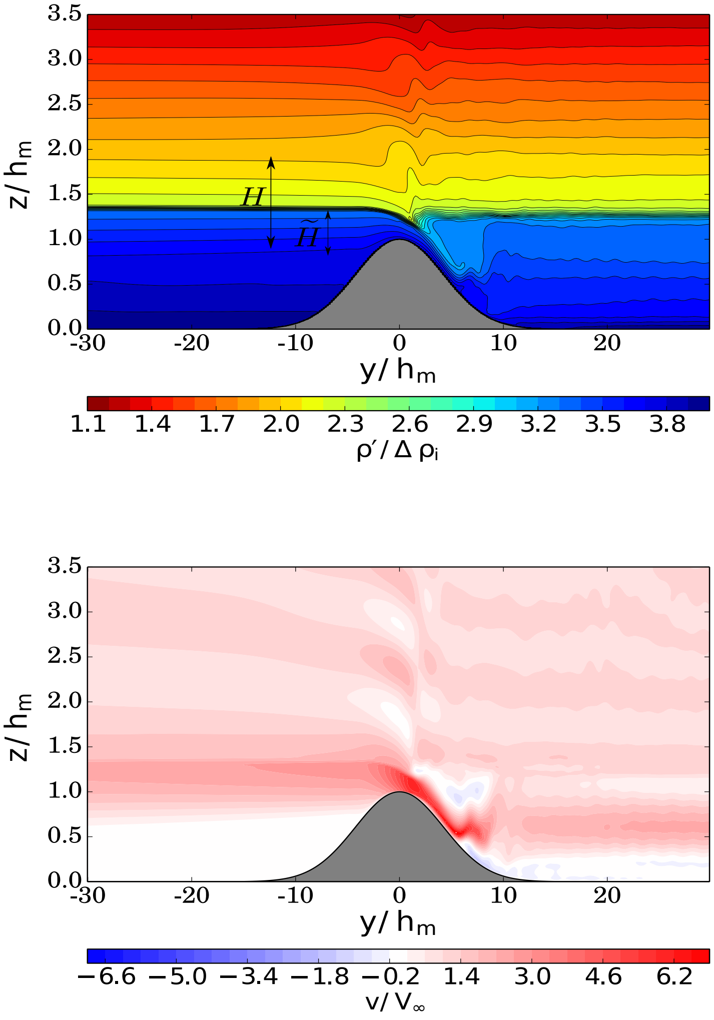

(a)

Figure 4.7: Same as Fig. 4.5 but for $z_0 = 1.35h_m$

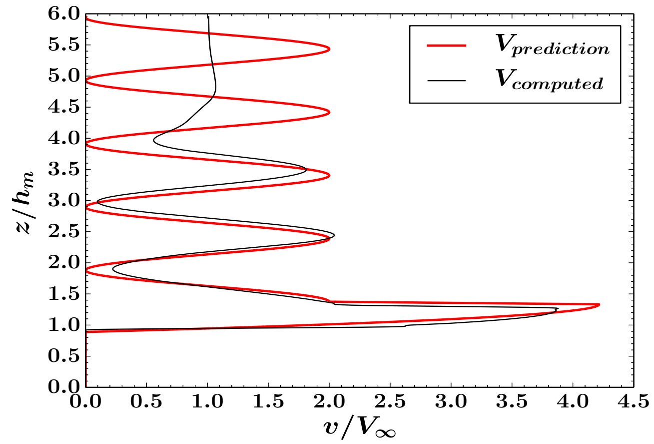

Figure 4.8: Same as Fig. 4.6 but for $z_0 = 1.35h_m$.

Unlike the Armi and Mayr (2015) study and the earlier works of Vosper (2004) and Jiang (2014), we consider a lower layer which is sufficiently stratified for blocking effects to be significant. In these flows, the natural fore-aft asymmetry induced by upstream blocking always triggers a hydraulic response, regardless of the location of the step. This differs from the study of Vosper (2004) in which the flow response ranges from vertically propagating disturbances to lee waves to a crest-controlled plunging flow depending on the inversion strength and location. The reduced gravity shallow water theory (Jiang, 2014) is also rendered inapplicable when the lower layer is stratified.

To summarize, in blocked topographically controlled flows that feature a sharp density step, a one-way decoupling exists in the sense that the flow in the upper stratified layer has no bearing on the crest-controlled flow in contact with the topography. However, the hydraulic character of this lower overflowing layer fundamentally controls the amplitude of the vertically propagating wave aloft. The theoretical framework developed in section 4.2 can predict the correct subcritical upstream overflow, including the shape of the interfacial layer across the crest. Whether or not the interfacial layer participates in the overflow is shown to be directly related to the constraint of maintaining subcriticality upstream and has a dramatic influence on the wave response further aloft. When the density interface remains flat across the crest, wave excitation is strongly suppressed. By contrast, in the case where the interface plunges asymmetrically down the lee slope, the amplitude of the wave response aloft is larger by a factor proportional to N_{δ_i}/N_0 compared to when the interface remains flat. In general, a quantification of the topographically controlled flow component is essential to determine the shape of the virtual topography and hence to predict the characteristics of the flow response further aloft.

This chapter is a draft of the manuscript under preparation for submission to the *Journal of Fluid Mechanics* as Jagannathan, A., Winters, K.B., Armi, L., “The dynamical link between hydraulic control and wave excitation aloft in blocked stratified flow over topography”. The dissertation author was the primary investigator and author of this work.

Appendix A

Mapping the Winters and Armi (2014) solution to arbitrary terrain shapes

In the numerical flow solutions we present in chapter 2, the specified pieces of information are the topography $h(y)$ and upstream flow conditions V_∞ and N. From these, we estimate the overflow transport Q and set up a quadratic equation for the upstream overflow thickness H as in Eq. (2.13). After determining H, it is specified as an input to the Winters and Armi (2014) model along with N and some small, constant slope for the bifurcating streamline. The model then produces flow solutions downstream of the blocking point, including an implied terrain shape $h^*(y)$ with peak height h^*_m. On either side of the crest, the solution additionally generates a unique one-to-one map between the drop of the bifuracting streamline $\eta^*(y)$ and the height of any point along the terrain surface relative to the blocking level $h^*(y) - (h^*_m - H/8)$. This is depicted schematically in Fig. A.1. The flow solutions at arbitrary downstream locations e.g. $y = y_1$ and y_2 along the given topography $h(y)$ in Fig. A.1a can be mapped to $y = y^*_1$ and y^*_2 respectively along the implied terrain shape produced by the Winters and Armi (2014) model, shown in Fig. A.1b. Thus the analytical flow solutions of Winters and Armi (2014) are valid for any arbitrary hydrostatic topography.

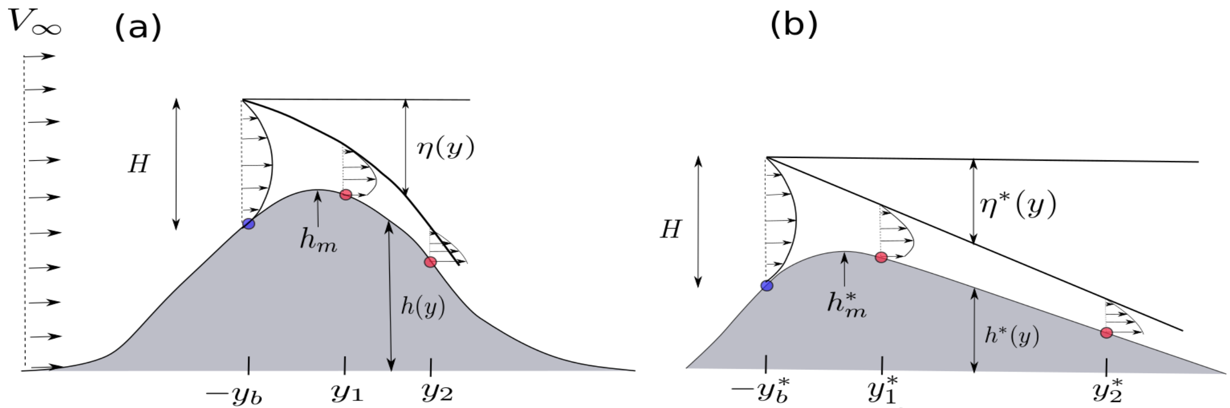

$$\left.\begin{aligned}\eta(y_1)=\eta^*(y_1^*) &\implies h_m - h(y_1) = h_m^* - h^*(y_1^*)\\ \eta(y_2)=\eta^*(y_2^*) &\implies h_m - h(y_2) = h_m^* - h^*(y_2^*)\end{aligned}\right\} \implies \begin{aligned} y_1 &\leftrightarrow y_1^*\\ y_2 &\leftrightarrow y_2^*\end{aligned}$$

Figure A.1: Schematic illustrating how blocked controlled flows over an arbitrary topography are mapped to the Winters and Armi (2014) solution. (a) Low Fr flow of specified upstream velocity V_∞ and uniform stratification N incident on an arbitrary topography $h(y)$ produces a hydraulically controlled overflow with a bifurcating streamline $\eta(y)$ of unknown slope as indicated. The blocking location is at $y = -y_b$ and the upstream overflow depth H is determined by solving the transport equation (e.g. Eq. (2.13)). The resulting streamwise velocity profiles at arbitrary downstream locations $y = y_1$ and y_2 are also shown. (b) Schematic of the Winters and Armi (2014) solution. The upstream overflow thickness H found in (a) is now specified and a bifurcating streamline of constant slope is imposed. Downstream of the blocking location $y = -y_b^*$, layerwise integration of Bernoulli's equation yields the flow solution within the controlled layer and also produces a corresponding terrain shape $h^*(y)$ with a single peak. On either side of the crest, the height by which the streamline has dropped $\eta^*(y)$ and the height of the terrain surface relative to the blocking point (shown as a blue dot) is a unique one-to-one map. Thus the solution obtained at any location, for example $y = y_1^*$ can be mapped to that at $y = y_1$ in (a), i.e. $y_1 \leftrightarrow y_1^*$ provided $h(y_1) - h(-y_b) = h^*(-y_b^*) - h^*(y_1^*)$.

Appendix B

Sensitivity of the flow structure aloft to domain height and sponge layer thickness

The question of whether the wave-like flow seen above the controlled overflow solutions of chapter 2, is caused by wave trapping as a result of imperfect radiation at the upper boundary and its possible effects on the overflow were investigated further. If the upper boundary in effect behaves as a rigid lid, then only certain quantized modes can exist and the quantization will dependent on the height of the domain.

To test whether the quantitative properties of the controlled overflowing layer and the oscillatory flow aloft (e.g. in Fig. 2.3a) depend sensitively on the choice of the domain height and sponge layer thickness, we repeated the $Fr = 0.16$ infinite ridge simulation described in section 2.5.1 of chapter 2 for three different configurations of domain and sponge layer depths. The sponge layer is designed to absorb the most energetic upward propagating waves of vertical scale about h_m. In the original case, the vertical height of the domain $L_z = 6h_m$ and the sponge layer has a thickness $1.8h_m$. In the other two cases, we set $L_z = 12h_m$ and $18h_m$, with much deeper damping layers, of thickness $4.5h_m$ and $6.7h_m$ respectively. The vertical profile of the streamwise velocity at the blocking point (Fig. B.1) shows that the quantitative properties of the controlled

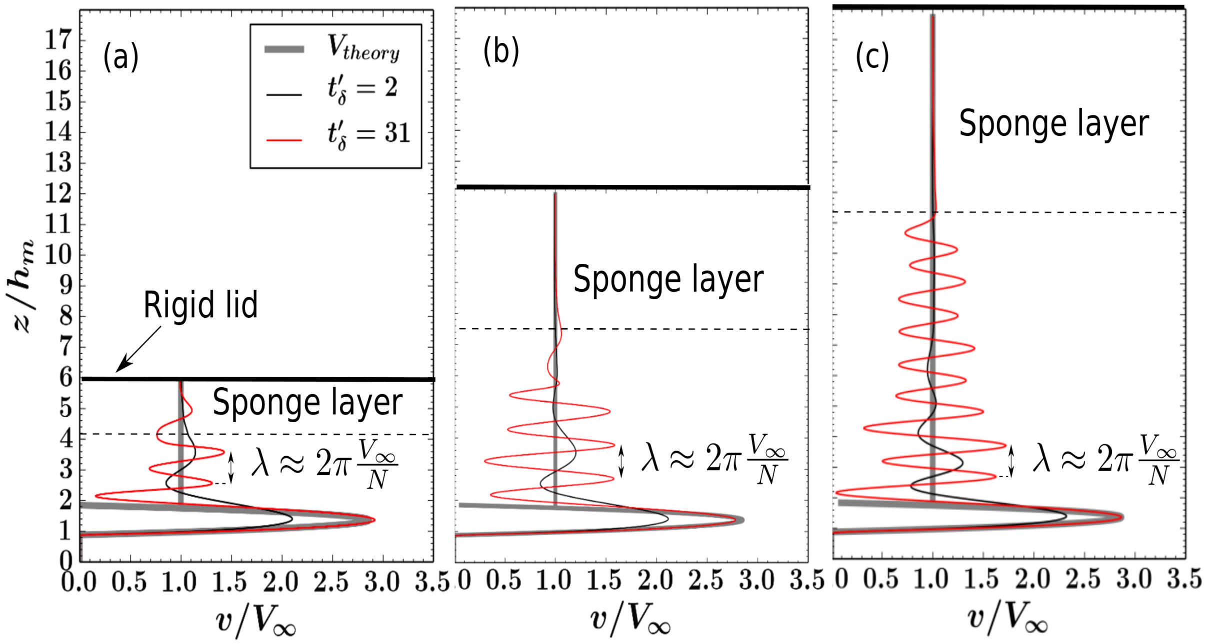

Figure B.1: Vertical profiles of the streamwise velocity at the blocking point $y \approx -y_b$ along with the analytical prediction of Winters and Armi (2014) (plotted in grey) for $Fr = 0.16$ flow over an infinite ridge with domain height and Rayleigh damping layer thickness respectively set to (a) $6h_m$ and $1.8h_m$, (b) $12h_m$ and $4.5h_m$ and (c) $18h_m$ and $6.7h_m$.

overflow are unchanged and the oscillatory flow structure aloft also persists in all cases. Further, Fig. B.1 shows that the vertical wavelength of this wave-like flow is independent of domain height and is around $\lambda \approx 2\pi V_\infty/N$ in all cases.

Appendix C

Description of the linear stability solver

We have developed a robust 2D flow stability solver that can determine the linear stability of parallel stratified shear flows, both in the inviscid case as well as when viscosity and thermal diffusion are included. The solver is versatile and can handle both homogeneous and inhomogeneous boundary conditions in any of the flow variables and for any order of the derivative so long as it is lower than the order of the differential equation. It is based on the Chebyshev collocation method which is used to discretize the governing Boussinesq equations and construct the coefficient matrices of the resulting generalized eigenvalue problem. The Gauss-Lobatto nodes are naturally clustered at the boundaries, which is useful in certain situations, e.g where boundary layer effects need to be resolved. But in some other cases, such as a *tanh* shear layer problem, higher grid resolution is required around the center of the domain. We thus include an cubic grid mapping option which redistributes the nodes so that they cluster around any specified point in the flow domain.

Solutions for Kelvin-Helmhotz instabilities in inviscid stratified shear flows have been validated by comparing against the benchmark results of Hazel (1972). We have also tested the code for the 4th order Orr-Sommerfeld equation by comparing the code predictions for the critical Reynolds number Re_{cr} for the plane Poiseuille flow with that of Orszag (1971); and the critical value of the Rayleigh number, Ra_{cr}, for the first two unstable modes of the 6th order Rayleigh-Benard stability problem with values found in Drazin and Reid (2004)

Unlike the shooting method that is commonly used to solve for the most unstable mode, the code also delivers the neutral wave modes and their speeds, both for stable as well as unstable flows. The solver can thus also be used for determining whether any given flow configuration is subcritical or supercritical by searching for the fastest upstream propagating internal wave mode it supports. The flow is subcritical if the speed $c_{up_{max}}$ of this mode is negative and supercritical if is positive. When this mode is exactly arrested, i.e. $c_{up_{max}} = 0$, the flow is critical.

Bibliography

Armi, L., and G. J. Mayr, 2007: Continuously stratified flows across an alpine crest with a pass: shallow and deep föhn. *Q. J. R. Meteorol. Soc.*, **133 (623)**, 459–477, doi:10.1002/qj.22.

Armi, L., and G. J. Mayr, 2015: Virtual and real topography for flows across mountain ranges. *J. Appl. Meteor. Climatol.*, **54 (4)**, 723–731, doi:10.1175/JAMC-D-14-0231.1.

Baines, P., 1977: Upstream influence and Long's model in stratified flows. *J. Fluid Mech.*, **82 (1)**, 147–159, doi:10.1017/S0022112077000573.

Baines, P. G., 1987: Upstream blocking and airflow over mountains. *Annu. Rev. Fluid Mech.*, **19 (1)**, 75–95, doi:10.1146/annurev.fl.19.010187.000451.

Baines, P. G., 1998: *Topographic effects in stratified flows*. Cambridge University Press.

Baines, P. G., and K. P. Hoinka, 1985: Stratified flow over two-dimensional topography in fluid of infinite depth: A laboratory simulation. *J. Atmos. Sci.*, **42 (15)**, 1614–1630, doi:10.1175/1520-0469(1985)042¡1614:SFOTDT¿2.0.CO;2.

Baines, P. G., and H. Mitsudera, 1994: On the mechanism of shear flow instabilities. *J. Fluid. Mech.*, **276**, 327–342.

Bauer, M. H., G. J. Mayr, I. Vergeiner, and H. Pichler, 2000: Strongly nonlinear flow over and around a three-dimensional mountain as a function of the horizontal aspect ratio. *J. Atmos. Sci.*, **57 (24)**, 3971–3991, doi:10.1175/1520-0469(2001)058¡3971:SNFOAA¿2.0.CO;2.

Bell Jr, T., 1974: Effects of shear on the properties of internal gravity wave modes. *Deutsche Hydrografische Zeitschrift*, **27 (2)**, 57–62.

Beluši'c, D., M. Pasarić, and M. Orlić, 2004: Quasi-periodic bora gusts related to the structure of the troposphere. *Quart. J. Roy. Meteor. Soc.*, **130 (598)**, 1103–1121, doi:10.1256/qj.03.53.

Brighton, P., 1978: Strongly stratified flow past three-dimensional obstacles. *Quart. J. Roy. Meteor. Soc.*, **104 (440)**, 289–307, doi:10.1002/qj.49710444005.

Cao, Y., and R. G. Fovell, 2016: Downslope windstorms of san diego county. part i: A case study. *Mon. Wea. Rev.*, **144 (2)**, 529–552, doi:10.1175/MWR-D-15-0147.1.

Carpenter, J. R., N. J. Balmforth, and G. A. Lawrence, 2010: Identifying unstable modes in stratified shear layers. *Phys. Fluids*, **22 (5)**, 054 104.

Carpenter, J. R., E. W. Tedford, E. Heifetz, and G. A. Lawrence, 2011: Instability in stratified shear flow: Review of a physical interpretation based on interacting waves. *Appl. Mech. Rev.*, **64 (6)**, 060 801.

Chamorro, L. P., and F. Porté-Agel, 2010: Effects of thermal stability and incoming boundary-layer flow characteristics on wind-turbine wakes: a wind-tunnel study. *Bound-layer Meteor.*, **136 (3)**, 515–533.

Chow, F. K., S. F. De Wekker, and B. J. Snyder, 2012: *Mountain weather research and forecasting: recent progress and current challenges*. Springer Science & Business Media, 750 pp., doi: 10.1007/978-94-007-4098-3.

Clark, T. L., and R. D. Farley, 1984: Severe downslope windstorm calculations in two and three spatial dimensions using anelastic interactive grid nesting: A possible mechanism for gustiness. *J. Atmos. Sci.*, **41 (3)**, 329–350.

Clark, T. L., and W. R. Peltier, 1977: On the evolution and stability of finite-amplitude mountain waves. *Journal of the Atmospheric Sciences*, **34 (11)**, 1715–1730, doi:10.1175/1520-0469(1977)034¡1715:OTEASO¿2.0.CO;2.

Clark, T. L., and W. R. Peltier, 1984: Critical level reflection and the resonant growth of nonlinear mountain waves. *Journal of the Atmospheric Sciences*, **41 (21)**, 3122–3134, doi:10.1175/1520-0469(1984)041¡3122:CLRATR¿2.0.CO;2.

Drazin, P. G., 1961: On the steady flow of a fluid of variable density past an obstacle. *Tellus*, **13 (2)**, 239–251, doi:10.1111/j.2153-3490.1961.tb00081.x.

Drazin, P. G., and W. H. Reid, 2004: *Hydrodynamic stability*. Cambridge university press.

Durran, D. R., 1990: Mountain waves and downslope winds. *Atmospheric processes over complex terrain*, W. Blumen, Ed., No. 45, Meteror. Monogr., Amer. Meteor. Soc., 59–81.

Epifanio, C. C., and D. R. Durran, 2001: Three-dimensional effects in high-drag-state flows over long ridges. *J. Atmos. Sci.*, **58 (9)**, 1051–1065, doi:10.1175/1520-0469(2001)058¡1051:TDEIHD¿2.0.CO;2.

Epifanio, C. C., and R. Rotunno, 2005: The dynamics of orographic wake formation in flows with upstream blocking. *J. Atmos. Sci.*, **62 (9)**, 3127–3150, doi:10.1175/JAS3523.1.

Farmer, D., and L. Armi, 1999: Stratified flow over topography: the role of small-scale entrainment and mixing in flow establishment. *Proc. R. Soc. London A*, The Royal Society, Vol. 455, 3221–3258.

Gaster, M., 1962: A note on the relation between temporally-increasing and spatially-increasing disturbances in hydrodynamic stability. *J. Fluid Mech.*, **14 (02)**, 222–224.

Hanazaki, H., 1988: A numerical study of three-dimensional stratified flow past a sphere. *J. Fluid Mech.*, **192**, 393–419, doi:10.1017/S0022112088001910.

Hazel, P., 1972: Numerical studies of the stability of inviscid stratified shear flows. *J. Fluid. Mech.*, **51 (01)**, 39–61.

Howard, L. N., 1961: Note on a paper of John W. Miles. *J. Fluid Mech*, **10 (4)**, 509–512.

Huang, C., Y.-L. Lin, M. L. Kaplan, and J. J. Charney, 2009: Synoptic-scale and mesoscale environments conducive to forest fires during the october 2003 extreme fire event in southern california. *J. Appl. Meteor. Climatol.*, **48 (3)**, 553–579, doi:10.1175/2008JAMC1818.1.

Huerre, P., G. K. Batchelor, H. K. Moffatt, and M. G. Worster, 2000: Open shear flow instabilities. *Perspectives in fluid dynamics*, 159–229.

Hughes, M., A. Hall, and R. G. Fovell, 2009: Blocking in areas of complex topography, and its influence on rainfall distribution. *J. Atmos. Sci.*, **66 (2)**, 508–518, doi:10.1175/2008JAS2689.1.

Hunt, J., Y. Feng, P. Linden, M. Greenslande, and S. Mobbs, 1997: Low-froude-number stable flows past mountains. *Il nuovo cimento C*, **20 (3)**, 261–272.

Hunt, J., and W. Snyder, 1980: Experiments on stably and neutrally stratified flow over a model three-dimensional hill. *J. Fluid Mech.*, **96 (4)**, 671–704, doi:10.1017/S0022112080002303.

Jackson, P. L., G. Mayr, and S. Vosper, 2013: Dynamically-driven winds. *Mountain weather research and forecasting*, F. K. Chow, S. F. De Wekker, and B. J. Snyder, Eds., Springer, 121–218, doi:10.1007/978-94-007-4098-3_3.

Jagannathan, A., K. B. Winters, and L. Armi, 2017: Stability of stratified downslope flows with an overlying stagnant isolating layer. *J. Fluid Mech.*, **810**, 392–411, doi:10.1017/jfm.2016.683.

Jagannathan, A., K. B. Winters, and L. Armi, 2018: Stratified flows over and around long dynamically tall mountain ridges. *Under review*. *J. Atmos. Sci.*

Jiang, Q., 2014: Applicability of reduced-gravity shallow-water theory to atmospheric flow over topography. *J. Atmos. Sci.*, **71 (4)**, 1460–1479, doi:10.1175/JAS-D-13-0101.1.

Kaye, N., 2008: Turbulent plumes in stratified environments: a review of recent work. *Atmosphere-ocean*, **46 (4)**, 433–441.

Lilly, D. K., 1978: A severe downslope windstorm and aircraft turbulence event induced by a mountain wave. *J. Atmos. Sci.*, **35 (1)**, 59–77.

Lin, Y.-L., 2007: *Mesoscale Dynamics*. Cambridge University Press, 630 pp., doi:10.1017/CBO9780511619649.

Linden, P. F., 1999: The fluid mechanics of natural ventilation. *Annu. Rev. Fluid Mech.*, **31 (1)**, 201–238.

Long, R. R., 1955: Some aspects of the flow of stratified fluids. iii. continuous density gradients. *Tellus*, **7**, 341.

Mayr, G. J., and L. Armi, 2010: The influence of downstream diurnal heating on the descent of flow across the sierras. *J. Appl. Meteor. Climatol.*, **49 (9)**, 1906–1912, doi:10.1175/2010JAMC2516.1.

Miglietta, M., and A. Buzzi, 2001: A numerical study of moist stratified flows over isolated topography. *Tellus A*, **53 (4)**, 481–499, doi:10.1111/j.1600-0870.2001.00481.x.

Miles, J. W., 1961: On the stability of heterogeneous shear flows. *J. Fluid Mech.*, **10 (04)**, 496–508.

Moum, J. N., D. M. Farmer, W. D. Smyth, L. Armi, and S. Vagle, 2003: Structure and generation of turbulence at interfaces strained by internal solitary waves propagating shoreward over the continental shelf. *J. Phys. Oceanogr.*, **33 (10)**, 2093–2112.

Ólafsson, H., and P. Bougeault, 1996: Nonlinear flow past an elliptic mountain ridge. *J. Atmos. Sci.*, **53 (17)**, 2465–2489, doi:10.1175/1520-0469(1996)053¡2465:NFPAEM¿2.0.CO;2.

Orszag, S. A., 1971: Accurate solution of the orr–sommerfeld stability equation. *J. Fluid Mech.*, **50 (04)**, 689–703.

Peltier, W. R., and J. F. Scinocca, 1990: The origin of severe downslope windstorm pulsations. *J. Atmos. Sci.*, **47 (24)**, 2853–2870, doi:10.1175/1520-0469(1990)047¡2853:TOOSDW¿2.0.CO;2.

Pierrehumbert, R., and B. Wyman, 1985: Upstream effects of mesoscale mountains. *J. Atmos. Sci.*, **42 (10)**, 977–1003, doi:10.1175/1520-0469(1985)042¡0977:UEOMM¿2.0.CO;2.

Porté-Agel, F., Y.-T. Wu, H. Lu, and R. J. Conzemius, 2011: Large-eddy simulation of atmospheric boundary layer flow through wind turbines and wind farms. *J. Wind Eng. Ind. Aerod.*, **99 (4)**, 154–168.

Queney, P., 1948: The problem of air flow over mountains: A summary of theoretical studies. *Bull. Amer. Meteor. Soc.*, **29**, 16–26.

Schar, C., and D. R. Durran, 1997: Vortex formation and vortex shedding in continuously stratified flows past isolated topography. *J. Atmos. Sci.*, **54 (4)**, 534–554, doi:10.1175/1520-0469(1997)054¡0534:VFAVSI¿2.0.CO;2.

Scinocca, J. F., and W. R. Peltier, 1989: Pulsating downslope windstorms. *J. Atmos. Sci.*, **46 (18)**, 2885–2914.

Sheppard, P., 1956: Airflow over mountains. *Quart. J. Roy. Meteor. Soc.*, **82 (354)**, 528–529, doi:10.1002/qj.49708235418.

Smith, R. B., 1980: Linear theory of stratified hydrostatic flow past an isolated mountain. *Tellus*, **32 (4)**, 348–364, doi:10.3402/tellusa.v32i4.10590.

Smith, R. B., 1985: On severe downslope winds. *J. Atmos. Sci.*, **42 (23)**, 2597–2603, doi: 10.1175/1520-0469(1985)042¡2597:OSDW¿2.0.CO;2.

Smith, R. B., 1989: Hydrostatic airflow over mountains. Adv. Geophys., Vol. 31, Elsevier, 1–41, doi:10.1016/S0065-2687(08)60052-7.

Smith, R. B., 1991: Kelvin-Helmholtz instability in severe downslope wind flow. *J. Atmos. Sci.*, **48 (10)**, 1319–1324.

Smolarkiewicz, P. K., and R. Rotunno, 1989: Low froude number flow past three-dimensional obstacles. part I: Baroclinically generated lee vortices. *J. Atmos. Sci.*, **46 (8)**, 1154–1164, doi:10.1175/1520-0469(1989)046¡1154:LFNFPT¿2.0.CO;2.

Tisseur, F., and K. Meerbergen, 2001: The quadratic eigenvalue problem. *SIAM review*, **43 (2)**, 235–286.

Vosper, S. B., 2004: Inversion effects on mountain lee waves. *Quarterly Journal of the Royal Meteorological Society*, **130 (600)**, 1723–1748, doi:10.1256/qj.03.63.

Wells, H., S. Webster, and A. Brown, 2005: The effect of rotation on the pressure drag force produced by flow around long mountain ridges. *Quart. J. Roy. Meteor. Soc.*, **131 (608)**, 1321–1338, doi:10.1256/qj.04.37.

Winters, K. B., 2016: The turbulent transition of a supercritical downslope flow: sensitivity to downstream conditions. *J. Fluid Mech.*, **792**, 997–1012, doi:10.1017/jfm.2016.113.

Winters, K. B., and L. Armi, 2014: Topographic control of stratified flows: upstream jets, blocking and isolating layers. *J. Fluid Mech.*, **753**, 80–103, doi:10.1017/jfm.2014.363.

Winters, K. B., and A. de la Fuente, 2012: Modelling rotating stratified flows at laboratory-scale using spectrally-based dns. *Ocean Modell.*, **49**, 47–59, doi:10.1016/j.ocemod.2012.04.001.

Winters, K. B., and J. J. Riley, 1992: Instability of internal waves near a critical level. *Dyn. Atmos. Oceans*, **16 (3-4)**, 249–278.